PHYSIK-DEPARTMENT

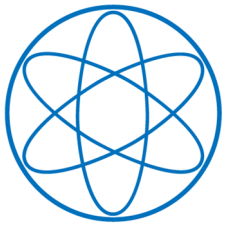

Stimuli-responsive reversible hydrogels from polyampholytes

Dissertation
von

Margarita A. Dyakonova

TECHNISCHE UNIVERSITÄT
MÜNCHEN

TECHNISCHE UNIVERSITÄT MÜNCHEN

Physik-Department

Fachgebiet Physik weicher Materie

Stimuli-responsive reversible hydrogels from polyampholytes

Margarita A. Dyakonova

Vollständiger Abdruck der von der Fakultät für Physik der Technischen Universität München zur Erlangung des akademischen Grades eines

Doktors der Naturwissenschaften (Dr. rer. nat.)

genehmigten Dissertation.

Vorsitzender:	Univ.-Prof. Dr. Ulrich Gerland
Prüfer der Dissertation:	1. Univ.-Prof. Dr. Christine M. Papadakis
	2. Univ.-Prof. Dr. Hendrik Dietz

Die Dissertation wurde am .....16.03.2016..... bei der Technischen Universität München eingereicht und durch die Fakultät für Physik am ....21.04.2016..... angenommen.

One experiment I place above the thousand beliefs, created by imagination.

M. V. Lomonosov

Preface

The present project has been developed in collaboration with Prof. Constantinos Tsitsilianis from the Laboratory of Macromolecular Engineering at the Department of Chemical Engineering, University of Patras, Patras, Greece. The polymer synthesis was performed by Dr. Nikoletta Stavrouli and Dr. George Gotzamanis (Department of Chemical Engineering, University of Patras, Greece). The samples for structural and dynamical investigations were prepared by Dr. Maria T. Popescu and Sandra Gkermpoura (Laboratory of Macromolecular Engineering, Department of Chemical Engineering, University of Patras, Greece). Rheological measurements were carried out by Dr. Maria T. Popescu, Sandra Gkermpoura and Dr. George Gotzamanis.

Small-angle neutron scattering (SANS) studies were carried out at the KWS-1 and KWS-2 instruments operated by JCNS at the Heinz Maier-Leibnitz Zentrum (MLZ, Garching, Germany) and at the D22 instrument at Institut Laue–Langevin (ILL, Grenoble, France). Experiments were carried out with the support from the instrument scientists: Dr. Sebastian Jaksch, Dr. Zhenyu Di (KWS-1/KWS-2) and Dr. Isabelle Grillo (D22).

Rotational dynamic light scattering (DLS) studies were performed at the Department of Supramolecular Polymer Systems, Institute of Macromolecular Chemistry (Prague, Czech Republic), with the help of Dr. Sergey K. Filippov and Prof. Dr. Petr Štěpánek.

Abstract

Stimuli-responsive hydrogels from polyampholytes have recently attracted great interest in various fields of applications due to their tunable rheological properties. In the current work, we study the influence of pH and ionic strength on the associative character of several types of polyampholytes and the resulting nanostructure of the hydrogels. By means of small-angle neutron scattering, we reveal the strong influence of the charge asymmetry and density on the network architecture. The dynamical processes in the gels are investigated using rotational dynamic light scattering.

Abstrakt

In jüngster Zeit haben stimuliresponsive Hydrogele aus Polyampholyten großes Interesse in den verschiedenen Anwendungsbereichen auf Grund ihrer kontrollierbaren rheologischen Eigenschaften geweckt. In dieser Arbeit untersuchen wir den Einfluss von pH-Wert und Ionenstärke auf den assoziativen Charakter verschiedener Polyampholyte sowie die Nanostruktur der Hydrogele. Mit Neutronenkleinwinkelstreuung zeigen wir den starken Einfluss der Ladungsasymmetrie und -dichte auf die Netzwerkarchitektur. Die dynamischen Prozesse in den Gelen werden mit dynamischer Lichtstreuung in Rotationsgeometrie untersucht.

Contents

1. Introduction

In recent decades, the interest to stimuli-responsive reversible hydrogels has greatly risen due to advanced macromolecular engineering, which allows obtaining polymer materials with precisely controlled morphologies. Their diversity and sensitivity to different external stimuli drives mankind to explore new areas of possible applications, which include almost all areas of everyday life.

The present work is devoted to studies of self-assembled hydrogels from stimuli-responsive polyampholytes. Previously, properties of polyampholyte hydrogels have been shown to have rich pH-dependent rheological behavior, which inevitably raises an interest to these systems as model systems for multiple applications.[1-9] Network formation in polyampholyte systems is driven by various intermolecular interactions, namely electrostatic interactions between ionized groups as well as hydrophobic and H-bonding. Electrostatic attractive interactions between oppositely charged moieties result in a formation of interpolyelectrolyte complexes (IPEC),[10,11] which act as temporary cross-links of the network. In polyampholytes, the extent of electrostatic interactions, and, hence, an extent of interpolyelectrolyte complexation is defined by charge conditions, namely charge asymmetry and charge density. The latter ones can be greatly affected by various parameters. In present work we aim to investigate the influence of pH and ionic strength on the associative character of several types of polyampholytes and the conformational properties of formed hydrogels, responsible for their mechanical behavior.

At first, we will focus on the effect of charge asymmetry on the self-organized structure of the quaternized polyampholyte PAA-*b*-QP2VP-*b*-PAA (PAA and P2VP are poly(acrylic acid) (weak polyacid) and quaternized poly(2-vinylpyridine) (strong polybase)). This polymer exhibits pH-responsive self-organization behavior due to protonation - deprotonation equilibrium of the PAA blocks, while the QP2VP block is strongly charged, independently of pH. By varying pH, it is possible to change the ratio $[AA^-]/[2VPR^+]$, and, hence, to influence the charge asymmetry in the system. By means of small-angle neutron scattering (SANS) we will focus on the structural changes, laying at the origin of detected earlier sol-to-gel transition decreasing pH from 7.0 to 3.0. Increase in charge imbalance is expected to influence the extent of both: attractive and repulsive electrostatic interactions, and affect the resulting gelation ability.

With the aim to better understand the behavior and structure of this kind of systems, we will investigate the gel and network properties in two other systems, with the same triblock architecture and block lengths but with different degree of ionization of the P2VP block - the nonquaternized polyampholyte PAA-*b*-P2VP-*b*-PAA, and with different end-block nature - the telechelic polyelectrolyte P*t*BA-*b*-P2VP-*b*-P*t*BA (P*t*BA is poly(*tert*-butyl acrylate), hydrophobic). Systems will be studied at pH 3.0, where the maximum viscosity for them was previously detected. Lower degree of ionization of the P2VP blocks in PAA-*b*-P2VP-*b*-PAA and P*t*BA-*b*-P2VP-*b*-P*t*BA in comparison to the one in PAA-*b*-QP2VP-*b*-PAA is expected to lead to a lower extent of electrostatic interactions and higher hydrophobicity from the non-ionized units, which would inevitably lead to the differences in structural and rheological behavior of these systems.

Further, we will investigate the influence of the screening effect of the monovalent salt NaCl on the behavior and the network properties in hydrogels from similar kind of triblock polyampholytes PAA-*b*-P2VP-*b*-PAA at pH 3.0. To investigate the influence of charge density, we perform comparative SANS studies on a reference system: quaternized counterpart PAA-*b*-QP2VP-*b*-PAA at pH 5.0, where the degrees of ionization of both blocks (PAA, QP2VP) are significantly higher than in the first system, making electrostatic interactions predominant and responsible for the behavior in solution. Increase in ionic strength is expected to decrease the charge density of both ionizable blocks PAA and P2VP, which would result in variations in structure of formed hydrogels.

Finally, we will investigate the influence of charge density on the structure of hydrogels from the telechelic polyampholyte PMMA-*b*-P(DEA-*co*-MAA)-*b*-PMMA (PMMA, PDEA and PMAA are poly(methyl methacrylate), poly(2-(diethylamino)ethyl methacrylate) and poly(methacrylic acid)), in dilute and semi-dilute regime. The interest to the present system is caused by its different self-assembly mechanism due to the presence of the hydrophobic end-blocks along with the random polyampholytic middle block. The pH variation is expected to change the net charge of the middle block P(DEA-*co*-MAA), affecting the conformation behavior of the entire polymer in solution. Dynamical processes in the gel networks will be investigated by means of rotational dynamic light scattering (DLS).

2. Background

In order to understand the behavior of charged polymers in solution, we will start with the simple case of a single polyelectrolyte chain (chapter 2.1). There we will focus on several aspects, influencing the polyelectrolyte chain behavior in solution, namely characteristic length scales, counterion condensation, behavior in a poor solvent, etc. Chapter 2.1.2 describes polyelectrolyte chains in the semi-dilute regime. Finally, in chapter 2.2, we will consider the case of polyampholyte chains in semi-dilute solutions.

2.1. Polyelectrolytes

Recently a lot of polymeric materials appeared which can respond in some desired way to external stimuli. Among them are polyelectrolytes. Due to the presence of ionizable groups polyelectrolytes exhibit shrinkage or swelling in response to various external stimuli, like pH, ionic strength, solvent quality and electric field.[12-19] Highly responsive behavior raises a strong attention to these systems in various areas of applications, including development of sensors and actuators,[20-23] optical components,[24] and smart membranes for separation.[25] Plenty of applications relate to biocompatibility of polyelectrolytes, which makes it possible to use these systems for medical purposes: in drug delivery systems and implants for tissue engineering.[26-29]

Polyelectrolytes are polymers, which bear either cationic or anionic ionizable groups on the chain. In polar solvents, these groups can dissociate, and, depending on the degree of dissociation, they can be classified as strong or weak polyelectrolytes.[30-34] In figure 2.1, the structures of two synthetic polyelectrolytes are presented. Both are negatively charged polyacids when dissociated. Poly(sodium styrene sulfonate) (PSS) is a strong polyelectrolyte, which means it is completely dissociated in the whole pH range, while polyacrylic acid (PAA) represents a weak polyacid, which dissociates only in a certain pH range, and its degree of ionization varies with pH.

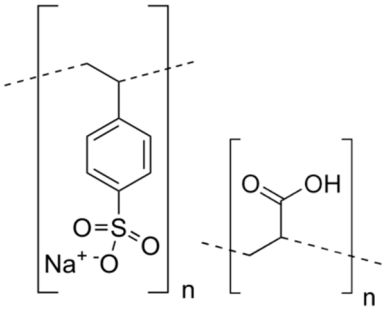

Fig. 2.1: Structure of poly(sodium styrene sulfonate), PSS (strong polyelectrolyte) and polyacrylic acid, PAA (weak polyelectrolyte). Taken from Ref. 35.

Another interesting class of charged polymers is represented by polyampholytes. These carry both cationic and anionic charged groups on the backbone.[36,37] We will consider their properties in detail later.

Despite of the numerous studies, the ionizable polymers still remain weakly understood. In neutral polymers, the interactions between the molecules are short ranged and, hence, act on length scales smaller than the polymer chain size or the correlation length. In contrast, in polyelectrolytes the scales determining the physical properties, include both short range and long range or Coulombic. The latter ones introduce additional intermediate length scales, which influence the conformation of the chain, responsible for its behavior in solution. Moreover, presence of counterions and their condensation on the polymer chains have an impact on long range interactions in solution. Therefore, there is a complex correlation between various effects in the systems of ionized polymers. Multiple theories were developed for different cases of charged polymers: in dilute or semi-dilute solutions, in good or poor solvent, without or with counterions or salt ions, etc. Nevertheless, simultaneous presence of multiple factors affecting the behavior of ionized chains makes it sometimes complicated to compare the experiment to theory.

The fact that polyelectrolytes are charged molecules gives rise to a rich behavior in dilute and semi-dilute solutions, which is very different from those of neutral polymers. Some of the differences are summarized here:[38-41]

1. Shift to the semi-dilute regime happens at a significantly lower concentration than in case of neutral polymers. Long range electrostatic repulsion between charged monomers causes the polymer to expand, and, therefore small overlap concentrations and high viscosities.

2. The osmotic pressure of salt-free polyelectrolyte solutions is higher than the one of neutral polymers due to the presence of a high number of counterions.

3. The osmotic pressure of polyelectrolyte solutions increases with polymer concentration, and is strongly dependent on salt concentration.

This supports the idea of prevailing counterion contribution to the pressure. Counterions are electrostatically bound to charged chains, which leads to the formation of clouds of counterions around the polymer chains.[42] The local distribution of counterions around the chain impact the conformational properties of polyelectrolytes in solution. Particularly, counterion translational entropy is at the origin of enhanced solubility in charged systems.

4. Viscosity is proportional to the square root of polymer concentration $\eta \sim c^{1/2}$,[43] while in the solution of neutral polymers, there is a linear dependence.

5. In contrast to solutions of neutral polymers, the polyelectrolyte chains remain in unentangled regime in a much wider range of concentrations.

2.1.1. Single polyelectrolyte chain

Poisson-Boltzmann equation

The present chapter is based on refs. [44-46].

In order to understand the properties of electrolyte solutions, it is important to account for the influence of long range interactions between ions. In comparison with other interactions which act on a distance of a few Angstroms, the Coulombic interactions act on much larger scales.

Let us consider the atoms as particles with point charges at specific atomic positions. Then, the local electrostatic potential, $\psi(r)$, induced by charge density, $\rho(r)$, obeys the Poisson equation:

$$\Delta\psi(r) = -\frac{\rho(r)}{\varepsilon_0 \varepsilon(r)} \tag{2.1}$$

where ε_0 is the permittivity in vacuum. We assume that medium is isotropic, so that $\varepsilon(r) = \varepsilon$. For a system with many point-like particles indexed by i with charge q the charge density distribution is given by:

$$\rho(r) = q\sum_i \delta(r - r_i)\,. \tag{2.2}$$

Thus, the electrostatic potential from Eq. 2.1 can be rewritten as:

$$\psi(r) = -\frac{q}{4\pi\varepsilon_0\varepsilon}\sum_i \frac{1}{|r - r_i|}. \tag{2.3}$$

The local concentration of *i* species with a valence z_i at a distance *r* from the chain is related to the electrostatic potential by Boltzmann's law:

$$c_i(r) = c_i^0 \exp\left(-\frac{z_i e\langle\psi(r)\rangle}{k_B T}\right) \tag{2.4}$$

where the constant c_i^0 is the bulk ion concentration. The local charge density distribution $\rho(r)$ is given by the Boltzmann equation:

$$\rho(r) = e\sum_i z_i c_i(r). \tag{2.5}$$

Thus, Eq. 2.1 can be rewritten as:

$$\Delta\langle\psi(r)\rangle = -\frac{e}{\varepsilon_0\varepsilon}\sum_i z_i c_i^0 \exp\left(-\frac{z_i e\langle\psi(r)\rangle}{k_B T}\right). \tag{2.6}$$

Eq. 2.6 is a non-linear differential equation of the second order. In order to solve it some approximations have to be taken. Therefore two boundary conditions are introduced:[47] the system is considered under the condition of a weak electrostatic potential:

$$\langle\psi(r)\rangle << \frac{k_B T}{z_i e} \tag{2.7}$$

and in conditions of electroneutrality:

$$\sum_i z_i c_i^0 = 0. \tag{2.8}$$

Then, the linearized Poisson-Boltzmann equation is given by:

$$\Delta\langle\psi(r)\rangle = \frac{1}{\lambda_D{}^2}\langle\psi(r)\rangle \tag{2.9}$$

where λ_D is the Debye screening length:

$$\lambda_D = \sqrt{\frac{\varepsilon_0\varepsilon k_B T}{e^2\sum_i z_i{}^2 c_i^0}}. \tag{2.10}$$

It is equal to the distance up to which the potential is valid. If we consider that the potential is spherically symmetric around an ion, Eq. 2.9 becomes:

$$\langle\psi(r)\rangle = \frac{z_i e}{4\pi\varepsilon_0\varepsilon}\frac{e^{-r/\lambda_D}}{r} \tag{2.11}$$

with a pair interaction energy as:

$$U_{DH}(r) = z_i^{\,2} k_B T \frac{\lambda_B}{r} e^{-r/\lambda_D} \tag{2.12}$$

where λ_B is the Bjerrum length, or the distance, at which the interaction between two charges becomes equal to the thermal energy.[48] It is given by:

$$\lambda_B = \frac{e^2}{4\pi\varepsilon_0 \varepsilon k_B T}. \tag{2.13}$$

Single polyelectrolyte chains

The present chapter is based on ref. [41].

Let us now consider a single polyelectrolyte chain with the degree of polymerization *N* in salt-free solution immersed in a "dielectric vacuum" as a Gaussian chain, consisting of charged and uncharged monomers. Here, we consider a simplified model in order to introduce some of the important parameters for future discussions. As well we neglect the contribution from counterions because of the fact that, in infinite dilution, they are spread elsewhere around.

The energy of a single isolated polyelectrolyte chain in θ solvent includes a contribution from Coulomb interaction between charged monomers and an energy contribution from the "neutral" polymer, U_0, or the free energy of a bead-spring chain:

$$U = U_0 + \frac{1}{2} k_B T \sum_{i=1}^{N} \sum_{j \neq i} \frac{\lambda_B q_i q_j}{|r_i - r_j|} \tag{2.14}$$

where λ_B is again the Bjerrum length, which describes the strength of electrostatic interactions. The energy from a neutral polymer includes the term describing the chemical bonding of the monomers together with short range excluded volume interactions. Here, the simple case of U_0 as the free energy of a Gaussian chain in salt-free solution is considered:

$$U_0 = \frac{3k_B T}{2b^2} \sum_{i=1}^{N-1} (r_{i+1} - r_i)^2 \tag{2.15}$$

where *b* is the monomer size. The chain is considered to carry only a few charges, so the average total charge is *fNe* with *f* being a fraction of charged monomers. After averaging over all possible conformations the free energy can be written as a function of *R* as:[49]

$$F_{tot}(R) \sim k_B T \left[\frac{R^2}{Nb^2} + \frac{(Nf)^2 \lambda_B}{R} \ln\left(\frac{R}{bN^{1/2}} \right) \right]. \tag{2.16}$$

The first term represents the contribution from elastic energy, while the second term considers the contribution from Coulombic interactions. After minimizing the free energy of the chain with respect to *R*:

$$R \sim bNu^{1/3} f^{2/3} [\ln(eN(uf^2)^{2/3}]^{1/3} \tag{2.17}$$

where $u = \lambda_B / b$ is the interaction parameter. It can be seen that the chain size grows faster than linear with the chain's degree of polymerization and increases with the charge fraction. It is bigger than the size of a neutral chain ($R_n^2 \sim Nb^2$), which is due to the stretching of a polyelectrolyte chain as a result of electrostatic repulsion between charged monomers.

Now let us consider the effect of the degree of ionization on the conformational properties of the chain. Above a certain critical number of charged monomers fN, the chain starts to elongate in order to minimize its free energy. The critical value can be calculated by equating the electrostatic energy to the thermal energy, k_BT:

$$\frac{\lambda_B (fN)^2}{bN^{1/2}} \approx 1 \tag{2.18}$$

from where the critical number of charged monomers is given by:

$$fN \approx u^{-1/2} N^{1/4}. \tag{2.19}$$

Upon a further increase in electrostatic energy, the chain continues to elongate monotonously with increasing charge fraction, f, until it reaches a rod-like conformation.

Scaling model of the polyelectrolyte chain

The present chapter is based on ref. [50].

In this section for dilute solutions and in the next one for semi-dilute solutions of polyelectrolytes, we will try to summarize the most important differences in the behavior of chains. The below presented scaling approach becomes possible when introducing different length scales, which separate different regimes of screening of electrostatic interactions. Among them is the electrostatic blob, which separates two different chain regimes.[38,50]

The electrostatic blob is defined as the distance below which the conformation of the chain remains unperturbed by the electrostatic interactions.[50] In θ solvent, it is given by:

$$D \approx b\left(uf^2\right)^{-1/3}. \tag{2.20}$$

Above *D*, the electrostatic interactions become relevant and lead to the elongation of the chain into an array of electrostatic blobs (fig. 2.2).

Fig. 2.2: Schematic representation of the polyelectrolyte chain as an array of electrostatic blobs of size *D*.

The size of the chain is given by:

$$R_b \approx bN\left(uf^2\right)^{1/3}. \tag{2.21}$$

From Eq. 2.20 and 2.21 it can be seen that both, blob size and chain size depend on the interaction parameter, *u*, and the charge fraction, *f*. Eq. 2.21 is different from Eq. 2.17, given earlier for the chain size, by a logarithmic term. Nevertheless, Eq. 2.21 can be transformed to Eq. 2.17 by taking into account the non-uniformity of chain stretching, in other words, considering that the blobs in the middle of the chain interact with the rest of the chain more strongly than the ones at its ends.[41,51] Nevertheless, the correction term is small, and at this stage it is more important for us to understand the general concepts of the chain behavior.

Poor solvent

The present chapter is based on ref. [41].

Most of the studied polyelectrolytes, being organic with a non-polar backbone, can dissociate in polar solvents like water only at a certain conditions, while in any other case, water can be considered a poor solvent. Poor solvent causes a competition between the hydrophobic attractive interactions along the backbone and electrostatic repulsion between equally charged units. Many theoretical studies have been carried out on charged chains in salt-free solutions in poor solvent.[52-60] The main finding reveals the transition from a more globular state to an elongated one and, finally a pearl-necklace with an increase in the charge density and electrostatic repulsion between the charges. Dobrynin's et al. studies on a single weakly charged chain have shown a continuous transformation from one to two and more globules, connected by strings with increase in electrostatic strength.[61] Micka et al. in their studies on strongly charged flexible polyelectrolytes varied the polymer density and the electrostatic interaction strength in order to follow a transition from the state with prevailing electrostatic interactions

to the state, characterized by strong screening.[62] They have found that at low polymer densities, strong Coulomb interactions dominate and result in strongly stretched, necklace-like conformation of chains. In contrast, at high densities, short range hydrophobic attractive forces cause the chain to collapse.

In order to describe the behavior of a charged polymer in a poor solvent, we have to refer to the case of a neutral polymer chain. The free energy is given by an expansion:

$$\frac{F}{k_B T} \approx \frac{R^2}{b^2 N} + NB\rho + NC\rho^2 \tag{2.22}$$

where ρ is the number density of monomers. *N* and *C* on the right side describe the two-body and three-body interactions. For the case of the Lennard-Jones potential, *B* is given by:

$$B(T) = \frac{1}{2}\int dr\left(1-\exp\left(-\frac{U_{LJ}(r)}{k_B T}\right)\right) \approx b^3\left(1-\frac{\theta}{T}\right) \approx b^3\tau \tag{2.23}$$

where $\tau = 1\text{-}\theta/\mathrm{T}$ is the effective temperature. *C* is proportional to b^6. The size of the globule after minimizing the interaction part of the free energy with respect to the size is given by:

$$R \approx b\left(\frac{N}{|\tau|}\right)^{1/3}. \tag{2.24}$$

In case of a very poor solvent, or $|\tau| \approx 1$, the chain is in the collapsed state:[63]

$$R \approx bN^{1/3}. \tag{2.25}$$

If the electric charge of the globule exceeds some critical value, the globule becomes unstable and splits into an array of smaller globules according to the Rayleigh principle.[64] For a polyelectrolyte chain in the globular state, the critical fraction of charged monomers per chain is given by:

$$f_{crit} \approx \left(\frac{|\tau|}{uN}\right)^{1/2}. \tag{2.26}$$

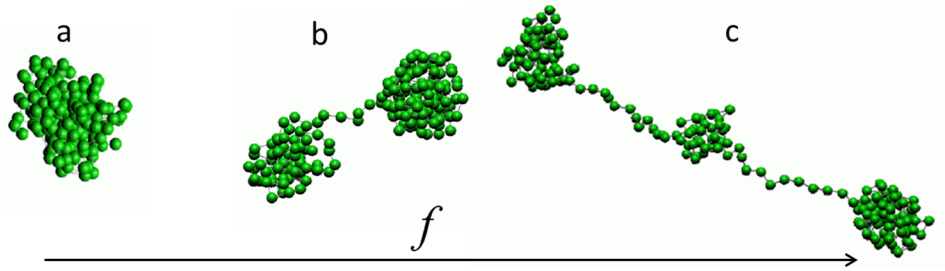

Fig. 2.3: Structure evolution of uniformly charged chain in poor solvent with increasing charge fraction. (a) A globule with $f = 0$; (b) a dumbbell with $f = 0.125$; (c) a necklace with $f = 0.15$. Taken from Ref. 65.

In case of a polyelectrolyte, the small globules are all located on one polymer chain and covalently bound. This fact does not permit them to spread around, instead it leads to a formation of a necklace of beads of size $D_b \approx b(|\tau| / uf^2)^{1/3}$, connected by strings (fig. 2.4). The string length is determined by the balance of the electrostatic repulsion between neighboring beads and the surface tension of string: $l_{str} \approx b(|\tau| / uf^2)^{1/2}$. The size of the necklace is given by:

$$L_{nec} \approx bN\left(uf^2 / |\tau|\right)^{1/2}. \qquad (2.27)$$

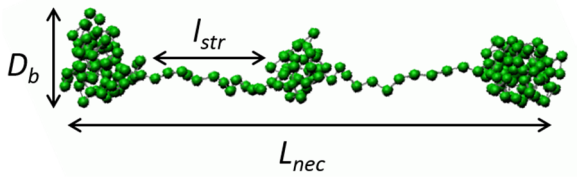

Fig. 2.4: A pearl-necklace with its characteristic dimensions. Taken from Ref. 65.

At this stage, we have shown that the chain behavior in a poor solvent is determined by the charge fraction, *f*. The size of both - bead and string - increases with the absolute value of the effective temperature, τ, whereas it decreases with increasing fraction of charged monomers, *f*. We will refer to these findings later in order to compare the behavior of a single polyelectrolyte chain to the one of the chain in a semi-dilute solution.

Counterion condensation

The present chapter is based on ref. [41].

In previous discussions, the presence of counterions was neglected. However, in real systems, especially in highly charged systems, there is always a finite concentration of counterions, which, at certain conditions, start to condensate on the polymer chains.[66] It was shown

experimentally that condensation of counterions and their local distribution influence the behavior of the chain in solution.[67,68] Roland et al. studied highly charged chains and found that counterion condensation provokes ion pair formation.[69] As a result of this, attractive dipole-dipole interactions further causes the polymer chains to collapse or shrinkage in case of networks.

The phenomenon of condensation is related to the value of the parameter $\lambda_B = b$.[41] It defines two classes of polyelectrolytes: weakly charged with $\lambda_B / b < 1$, when the distance between two closest charged groups on a polymer backbone is larger than the Bjerrum length, and strongly charged, for which $\lambda_B / b > 1$ (fig. 2.5). The counterion condensation occurs only in case of strongly charged polyelectrolyte systems.

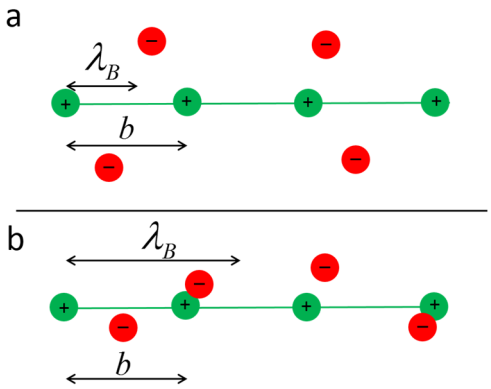

Fig. 2.5: Two classes of polyelectrolytes: weakly charged, no counterion condensation, $\lambda_B / b < 1$ (a) and strongly charged, with counterion condensation, $\lambda_B / b > 1$ (b).

The counterions screen some fraction of charges, which is the reason that the effective charge of polymer is lower than its nominal charge.

Osmotic pressure

The present chapter is based on ref. [41].

The osmotic pressure in dilute polyelectrolyte solution is given by the sum of ideal pressure of gas of non-interacting counterions and pressure of polymer chains:

$$\frac{\pi}{k_B T} = \frac{\pi_{ion}}{k_B T} + \frac{\pi_{pol}}{k_B T} = fc + \frac{c}{N^3} \qquad (2.28)$$

where c is the polymer concentration and f the charge fraction. From Eq. 2.28 it can be seen that, at infinitely low concentrations, the contribution from the chain remains very small since

it scales inversely proportional to the third power of the polymerization degree. This supports the earlier introduced hypothesis that the osmotic pressure of polyelectrolyte solutions is dominated by counterions.

Salt effect and persistence length

The present chapter is based on refs. [41,70-71].

Addition of salt partially screens the electrostatic interactions between charged monomers. As it was shown previously, the strength of interactions decreases with increasing the distance between charged monomers, however, they still interact through unscreened Coulomb potential at a distances smaller than λ_D. At low salt concentrations, when the Debye screening length is much larger than the chain size $\lambda_D >> R_b$, there is no effect on the chain conformation. At high salt concentrations, when the Debye screening length is smaller than the electrostatic blob size $\lambda_D << D$, a polyelectrolyte chain behaves as a neutral polymer in good solvent. At intermediate salt concentrations, when $D < \lambda_D < R_b$, the interactions between charges are responsible for the local stiffness of the chain at the distances above the Debye screening length, λ_D. The stiffness can be described by means of electrostatic persistence length, L_e, which is salt concentration dependent.

Originally, L_e was calculated by evaluating the change in electrostatic energy of polymer, induced by deviation of its conformation from the linear one. Here, we will only present the final equations for L_e.

For charged systems the total persistence length includes contribution from the bare, L_0, and electrostatic, L_e, persistence length:

$$L_t = L_0 + L_e . \tag{2.29}$$

Electrostatic persistence length is given by:

$$L_e = \frac{\lambda_B}{b^2}\left(\frac{\lambda_D}{2}\right)^2 . \tag{2.30}$$

Since L_e for weakly screened solutions is larger than λ_D, we can make a conclusion that the effect from electrostatic interactions extends above λ_D value. It is worth to note that polymer conformation is defined by its bare rigidity, L_0, at small length scales, while by the persistence rigidity, L_e, at larger length scales.

In poor solvent, the electrostatic persistence length increases further with decreasing solvent quality:[33]

$$L_e \sim D + \lambda_D^2 \tau^2 \lambda_B^{-1/3} \tag{2.31}$$

which results in increase in radius of gyration in poor solvent instead of its decrease as it happens in solutions of neutral polymers.

We have shown that both, charge fraction and ionic strength, have an influence on electrostatic rigidity of the polyelectrolyte chain, and, therefore, influence its conformational properties. The latter ones have a significant impact on the final rheological behavior. Further we will consider this influence in semi-dilute solutions due to their relevance to the studied here systems.

2.1.2. Semi-dilute solutions

The present chapter 2.1.2 is based on ref. [41].

In charged systems, shift to the semi-dilute regime occurs when the distance between chains becomes comparable with the chain size:[38,39]

$$c^* \propto N / R^3 \propto 1/(N^2 \ln N)\,. \tag{2.32}$$

Thus, the solution overlap concentration has much stronger dependence on the degree of polymerization in comparison to the one for solutions of neutral chains ($c_n^* \propto N^{-1/2}$), which explains the shift to the semi-dilute regime in polyelectrolytes and the gel network formation at very low concentrations.

Correlation length

Before we have shown that in dilute solutions of polyelectrolytes, there are several characteristic length scales, determining the behavior of chains: Debye screening length, λ_D; electrostatic correlation blob, *D*; electrostatic persistence length, L_t. In semi-dilute solutions above the overlap concentration, there is only one important length scale - correlation length, ξ, or the average mesh size (fig. 2.6). It was introduced initially in the cell model of Katchalsky et al.[72] The cell has a cylindrical symmetry with the polyelectrolyte chain, located along the axis of the cylinder. Each charged monomer experiences electrostatic repulsion from all other charged monomers within the correlation volume and electrostatic attraction due to the counterion background. The charge on the section of chain within the correlation length, ξ, is compensated by counterions, so the average charge of the correlation volume, ξ^3, is equal to zero.

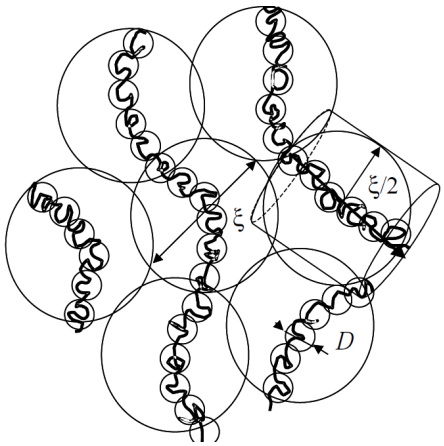

Fig. 2.6: Schematic representation of the cell model in semi-dilute regime with a radius of $\xi/2$ and length ξ and electrostatic blob size *D*. Data from Ref. 41.

The correlation length varies reciprocally with the square root of polymer concentration:

$$\xi \propto c^{-1/2}. \tag{2.33}$$

Expression for the electrostatic blob is rather lengthy, we do not present it here, it can be found in Ref. 41. At length scales smaller than ξ, chains are strongly stretched due to electrostatic repulsion between similarly charged monomers, similar to the chain behavior in dilute solutions. At length scales larger than ξ, both - electrostatic and excluded volume interactions - become screened and the polyelectrolyte chain can be represented as a random walk of size ξ,[30,38,47,73] with stronger concentration dependence than in case of uncharged polymers in semi-dilute solutions (for neutral polymer $R \approx c^{-1/8}$):

$$R \sim N^{1/2} c^{-1/4}. \tag{2.34}$$

This explains the unusually wide unentangled range in semi-dilute solutions of polyelectrolytes in comparison to solutions of neutral polymers.

Salt effect

In salt-free solutions below counterion condensation threshold, the Debye screening length is given by:[41]

$$\lambda_D = (4\pi\lambda_B f_* c)^{-1/2} \tag{2.35}$$

where f_* is the effective charge density on polymer. This value can be determined experimentally.[74] It is proportional to the number of free counterions, which, in turn, is related to the polymer degree of dissociation and solvent quality.

For calculating the scaling behavior in presence of salt, the screening length was assumed to expand in order to compensate the charge of both: counterions and salt ions:

$$\xi_s \approx \xi \left(1 + \frac{2c_s}{f_* c} \right)^{1/4} \tag{2.36}$$

where ξ (Eq. 2.33) is the correlation length in salt-free semi-dilute solution of polyelectrolytes and c_s the salt concentration. Assuming that the chain is an array of electrostatic blobs of a new size ξ_s, the chain size dependence is found to exhibit two limits.[41] In regime of high salt concentration, $\langle R^2 \rangle \propto N^{1/2} c^{-1/4} \propto I^{-1/4}$, whereas at low salt concentration limit, it is $\langle R^2 \rangle \propto N^{1/2} c^{-1/2} \propto I^{-1/2}$. Therefore, the chain size has a non-linear dependence on ionic strength, and so the rheological behavior.

Osmotic pressure

Osmotic pressure of polyelectrolyte solutions in semi-dilute regime has two contributions (as in dilute regime):[41]

$$\frac{\pi}{k_B T} = \frac{\pi_{ion}}{k_B T} + \frac{\pi_{pol}}{k_B T}. \tag{2.37}$$

The ionic term has two limits:[31]

$$\frac{\pi_{ion}}{k_B T} = 2c_s \left[\sqrt{\left(\frac{f_* c}{2c_s} \right)^2 + 1} - 1 \right] \cong \begin{cases} f_* c & c_s << f_* c \\ (f_* c)^2 / c_s & f_* c << c_s \end{cases}. \tag{2.38}$$

The polymeric contribution is $k_B T$ per correlation volume:[40,63]

$$\frac{\pi_{pol}}{k_B T} = \xi^{-3}. \tag{2.39}$$

It can be seen that at low salt concentrations, the ionic contribution dominates, whereas at high ionic strengths, both contributions are small. Polymeric contribution to osmotic pressure becomes important only at high concentrations of polymer. At high polymer concentrations, long range electrostatic interactions get screened and short range excluded volume interactions become prevailing.

Poor solvent

Like in case of dilute solutions, polyelectrolyte chain in semi-dilute solution adopts a necklace conformation,[75,76] however there are three different regimes,[57,77-79] influencing the rheological behavior (fig. 2.7a). At low polymer concentrations, chain forms a necklace. Upon further increase in concentration, counterion condensation leads to a monotonous shrinkage of the chain, while shift to a more concentrated regime is accompanied by an increase of the chain size to the size of the Gaussian chain. All these transitions have a direct relation to the degree of ionization of the chain.

The normal dependence of correlation length $\xi = c^{-1/2} f_*^{-1/2}$ ($R \sim bN^{1/2} c^{-1/4} f_*^{1/4}$), discussed earlier, is valid until the concentration of polymer reaches:[41]

$$c_{str} \sim \frac{|\tau|}{u f_*^2} \tag{2.40}$$

at which the correlation length becomes of the order of the string length (fig. 2.7a). Above this concentration, there is only one bead in the correlation volume, ξ^3. This happens due to the

complete screening of electrostatic repulsion between beads by the beads on neighboring chains. The correlation length reduces to:

$$\xi = c^{-1/3} f_*^{-2/3}. \tag{2.41}$$

The system can be imagined as a dilute solution of beads. The chain size in this regime is:

$$R \approx bN^{1/2} c^{-1/3} f_*^{1/3}. \tag{2.42}$$

Upon a further increase in concentration, $c > c_b$, the beads start to overlap, so $\xi \sim D$ (fig. 2.7a). In this regime, the polymer chain behaves as an ideal chain with the size of the order of the Gaussian chain size. This can be explained by that fact that at this high concentration, the electrostatic interactions are mostly screened and chain behaves as a neutral one.

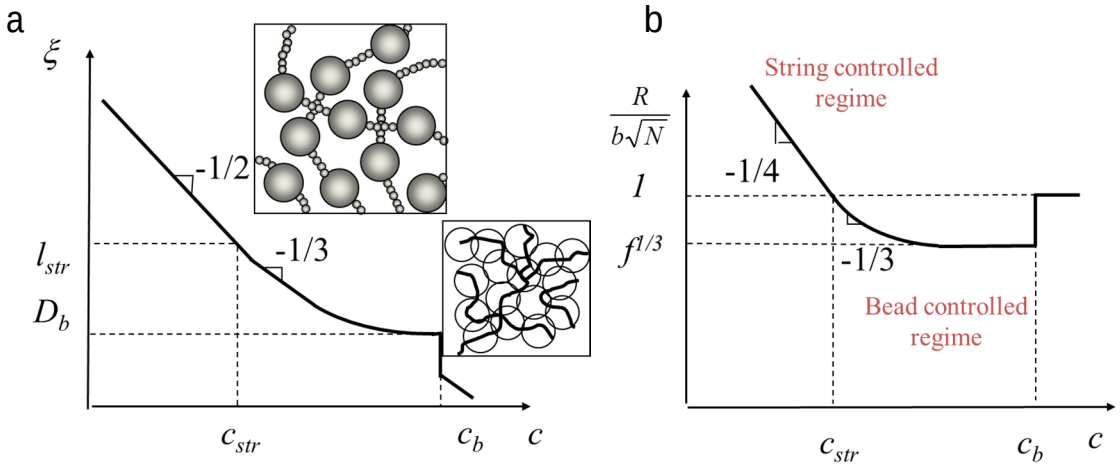

Fig. 2.7: (a) Correlation length, ξ, and (b) $R / b\sqrt{N}$ in dependence on polymer concentration. Data from Ref. 80.

From Eq. 2.40, it can be seen that the transition between two different scaling regimes occurs in dependence on solvent quality and charge fraction, which leads to a non-linear rheological response upon increase in polymer concentration. In discussions above it was shown that the charge fraction, in its turn, can be influenced by ionic strength.

2.2. Polyampholytes

Polyampholytes represent another important class of associative copolymers. In comparison to polyelectrolytes, polyampholytes contain both acidic and basic ionizable groups on the backbone.[36,37] In figure 2.8, structure of typical polyampholyte, consisting from weak base (2-vinylpyridine) and weak acid (acrylic acid), is presented.

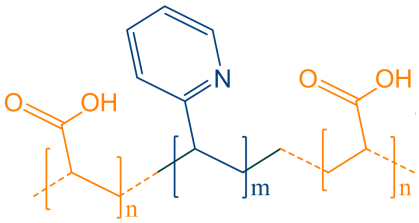

Fig. 2.8: Structure of polyampholyte, consisting from weak base (2-vinylpyridine) and weak acid (acrylic acid).

Polyampholytes deserve a special attention due to their responsive behavior in a much wider pH range in comparison with polyelectrolytes. Thus, the latter ones are dissociated in a certain pH range, depending on the nature of comprising blocks, whether it is acidic or basic. Polyampholytes possess behavior of both: the polybase at low pH values, and the polyacid at high pH values. Depending on the degree of ionization of both ionizable blocks and the net charge on the molecule, polyampholyte can follow the behavior of both: polyampholyte and polyelectrolyte. This rich behavior and possibility to control it attract a lot of attention to polyampholytic systems in terms of their possible applications. Thus, they are widely used for separation and purification processes, like protein separation,[2,81-82] recovery of metal ions,[83] for water desalination[4] and oil recovery processes.[1] Polyampholyte-metal complexes exhibit a catalytic activity.[3,84] Being water soluble and biocompatible, polyampholytes are widely used for biochemical and medical purposes,[5,7] such as artificial organs, muscles, implant coatings and controlled drug release.[6,8-9,85-86]

The oppositely charged monomers can be randomly[87-90] distributed along the polymer backbone or can be localized in separate regions of polymer, forming a block copolymer.[91-94] The local distribution of both ionizable blocks and the net charge on the chain strongly influences the chain conformation in solution and, therefore, mechanical properties of the system and its ability to respond to various external stimuli, like temperature,[95-97] pH[98-105] and ionic strength.[106-108]

2.2.1. Effect of charge asymmetry

Analogously to the case of polyelectrolytes in aqueous solutions, ionized groups on polyampholytes dissociate and the net charge on molecule can vary with pH or stay independent. At certain pH value, there is an equality in number of oppositely charged units, which leads to polymer net charge zero and its following precipitation. This pH is called isoelectric point *Iep*.

Depending on charge conditions, whether polyampholyte balanced or not, polymer exhibits two different behaviors. Thus, if the net charge is big, chain is located in a polyelectrolyte regime. Strong repulsive electrostatic forces between equally charged monomers result in extended chain conformation in dilute solutions.[30-31,33,109-111] In neutral or balanced polyampholytes, the chain collapses into a globule. This happens as a result of screening effect of charges of one sigh, surrounding the charge of the opposite sign, which leads to a gain in electrostatic energy.[112] Here, further we will not consider balanced polyampholytes since our system is highly imbalanced.

Several theoretical studies on behavior of polyampholytes have been carried out.[112-116] The conformational properties of diblock polyampholytes, depending on the charge asymmetry, or the net charge of the molecule, were studied by Shusharina and Rubinstein.[117] The authors showed that diblock polyampholytes with charge asymmetry form core-shell micelles. The core is formed by equal amount of positively and negatively charged blocks as a result of their mutual electrostatic attraction, while the remaining chains, carrying uncompensated charge of one sign, are located in the shell (fig. 2.9). The chains in the shell follow the behavior of a polyelectrolyte chain, which was described in previous sections.

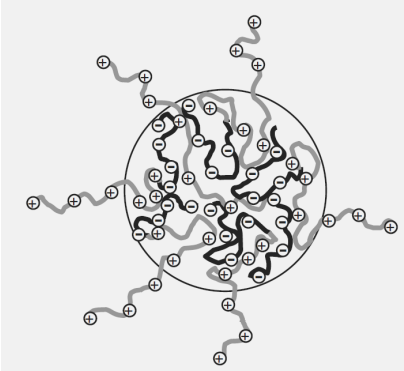

Fig. 2.9: Schematic representation of a star-like micelle from diblock polyampholytes. Taken from Ref. 118.

Similar observation were made by Jeon et al.[119] The authors have studied complexation of polyelectrolyte chain with both - random and diblock polyampholytes - in poor solvent. The authors showed that the polyelectrolyte chain changes its configuration from a common necklace conformation to a bead-like upon neutralization of charged units of one sign on polyelectrolyte by equal amount of oppositely charged units on polyampholyte. Complexation with a random polyampholyte results in the formation of a globular bead with a part of non-complexed chains, forming the loops around the aggregate (fig. 2.10a). In case of the block polyampholyte, the complexation results in the formation of a core from complexed oppositely charged chains, with a part of non-complexed charged chains of polyampholyte, sticking out of the core (fig. 2.10b).

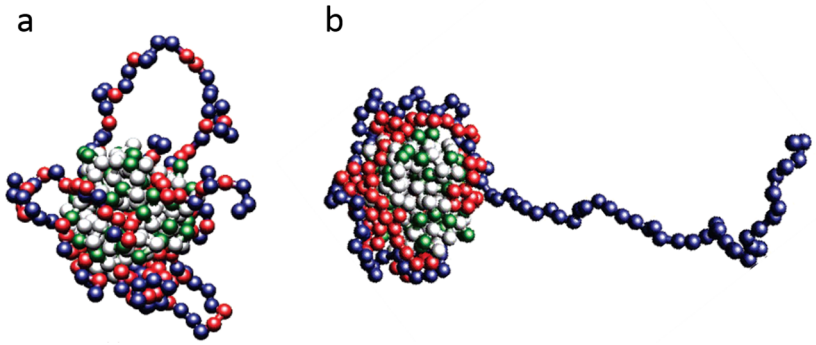

Fig. 2.10: Snapshots of structures formed by complexation of polyelectrolyte with random polyampholyte (a) and diblock polyampholyte (b). The positively and negatively charged monomers of the polyampholyte chain are shown in red and blue, respectively. The negatively charged and neutral monomers of the polyelectrolyte chain are shown in green and gray, respectively. Taken from Ref. 119.

In present work, significant part is devoted to studies of reversible hydrogels from block polyampholytes. Presence of electrostatic interactions, both attractive between oppositely charged units and repulsive between equally charged sequences, can lead to a gel formation at much lower concentrations in comparison with neutral polymers.[120,121] Polyampholytes can self-associate into a transient 3-D network as a result of multiple intermolecular interactions:[122,123] electrostatic, hydrophobic and H-bonding between certain functional groups on the chains. In polyampholyte systems, one of the most important features, which make the network formation possible are Interpolyelectrolyte complexes (IPEC) (fig. 2.11).[11,124] They act as temporary cross-links of the network and are built as a result of electrostatic attraction

between oppositely charged moieties. In case of charge neutrality, there is a precipitation of formed complexes, whereas charge asymmetry leads to the formation of a stable hydrogel.

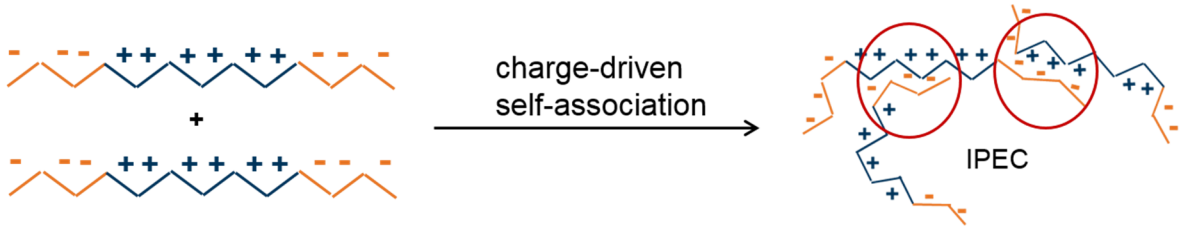

Fig. 2.11: Interpolyelectrolyte complex (IPEC) formation as a result of charge-driven association.

2.2.2. Effect of salt

Salt has a two-fold effect on the polyampholyte chains. The salt ions screen both, the attractive electrostatic forces between oppositely charged segments and repulsive forces between equally charged units.[112] Effect of ionic strength on behavior of polyampholyte chains was studied by different groups.[125-129] The behavior of the chain size upon addition of salt was shown to be a non-linear, depending on whether the chain is in polyelectrolyte or polyampholyte regime. Addition of salt to a polyampholyte chain in polyelectrolyte regime, or when the molecule carries high net charge, will lead to the collapse of strongly stretched chain due to the decrease in Debye length (Eq. 2.10). Upon further addition of salt, the Debye length decreases even further down to the size of internal polyampholyte Debye length and, therefore, screens the attractive forces on the backbone, permitting the polymer chain to swell. When the net charge on the chain is small (polyampholyte regime), the chain size grows monotonically with increase in ionic strength.[112]

Peiffer and Lundberg in their studies on charged polyampholytes have shown that addition of salt breaks numerous intramolecular electrostatic interactions, predominant in salt-free solutions, leading to a swelling of chains and, as a result, an increase in solution viscosity.[125] This phenomenon lays at the origin of enhanced solubility of polyampholytes upon increase in ionic strength.The same observation was made by Ohlemacher et al.[126] and English et al.[127] in their studies on non-neutral polyampholytes. The maximum of swelling was detected at relatively low ionic strengths. Further addition of salt was shown to cause the chains to shrink to the volume corresponding to the one of neutral chains.

Tanaka and Tanaka have shown that increase in ionic strength in solutions of randomly charged polyampholytes provokes a transition from the polyelectrolyte to the polyampholyte regime, which explains peculiar behavior of the radius of gyration of polymer.[128] The polyelectrolyte nature is predominant in salt-free solutions, whereas it gets weakened upon addition of salt, which screens the excess charges. This transition to the polyampholyte regime is accompanied by a simultaneous decrease in polymer radius of gyration. Further increase in ionic strength leads to an opposite effect of increase in radius of gyration, which is attributed to the transition from the polyampholyte regime to the non-charged state, where all electrostatic interactions get screened.

Nisato et al. revealed a similar behavior of shear modulus of hydrogels upon increase in ionic strength.[129] Thus, at low ionic strengths, the polyelectrolyte behavior is predominant, characterized by stretched conformation of chains and high shear modulus. Further increase in ionic strength causes a transition to the Gaussian chain conformation, followed by a simultaneous decrease in shear modulus.

Therefore, by varying the strength of electrostatic interactions after addition of salt, it is possible to influence the polymer chain conformation and resulting macroscopic behavior of the system.

2.3. Telechelic polyampholytes

Telechelic polymers, comprising a polyampholyte middle block, end-capped by short hydrophobic groups, represent another class of self-associating polymers. Among the multiple external stimuli, provoking the inter- and intramolecular associations, responsible for hydrogel formation, are temperature,[130-134] pH[135,136] and solvent quality.[137,138] Telechelic polyampholytes have attracted special attention because of their well-defined and controllable macromolecular architecture which results in tunable rheological properties.[138-140] Interplay between the hydrophobic associations of the outer blocks and electrostatic interactions between charged segments on the middle polyampholytic block define the behavior in solution. Presence of the ionizable blocks makes these systems multiresponsive, and, hence, attractive for applications in various fields. Particularly, by tuning the charge density on the micelles, it is possible to increase their stability, making these systems promising candidates for drug delivery applications.[8,94] The possibility to obtain materials with enhanced mechanical stability and reversible character of the sol-to-gel transitions stimulate their further application as solution stabilizers or material thickeners.[141,142]

In recent decades, several groups studied the influence of pH on the conformational properties of this kind of copolymers, comprising polyampholytic block. Gotzamanis et al. studied the behavior of two types of diblock terpolymers: the amphiphilic P(DEAEMA-*co*-MAA)-*b*-PMMA (PDEAEMA, PMAA and PMMA are poly(2-(diethylamino)ethyl methacrylate), poly(methacrylic acid) and poly(methyl methacrylate), respectively), that consists of a hydrophobic (PMMA) and a polyampholytic block, and PEGMA-*b*-P(DEAEMA-*co*-MAA) (PEGMA is poly(ethylene glycol) methyl ether methacrylate), which along with the polyampholytic block comprises a temperature-responsive (PEGMA).[93] The authors have shown that amphiphilic diblock terpolymer self-assembles through hydrophobic interactions between the PMMA blocks, which form the core, surrounded by the corona from the polyampholyte P(DEAEMA-*co*-MAA) blocks. Depending on pH, the charge of the corona changes its sign. The latter system demonstrates multiresponsiveness to various stimuli: combining different conditions, such as temperature, pH and ionic strength, the authors could obtain different types of micellar nanoparticles, varying in the charge of the corona: neutral, positive and negative.

Iatridi et al. have studied the self-organization of star block terpolymers consisting of hydrophobic polystyrene arms and polyampholyte diblock (P2VP-*b*-PAA) arms, all connected to a cross-linked poly(divinyl benzene), in dependence on pH.[143] It was shown that, upon increasing pH, the system forms various structures, ranging from unimolecular core-shell micelles via worm-like micelles to network-like large assemblies. The authors suggest that these structures result from the coexistence of three segments which are different in nature: hydrophobic PS and ionizable P2VP and PAA blocks. It was found that, below the *iep* of the polyampholytic diblock copolymer, the terpolymer is bis-hydrophilic (P2VP, PAA), whereas, above the *iep*, it is bis-hydrophobic (PS, P2VP), which dictates the mechanisms involved in structure formation. Among them are solvophobic repulsive interactions between the hydrophobic segments, intermicellar H-bonding as well as electrostatic interactions between charged segments.

Copolymerization in diblock terpolymers allows to tune the properties of the blocks and, thus, the properties of the resulting micellar structures. In contrast, self-assembly of triblock terpolymers can lead to the formation of more complex systems, like 3D networks. Further incorporation of the polyampholytic block allows obtaining systems, which are highly responsive in a wider range of pH in comparison with polyelectrolyte systems.

Tsitsilianis et al. have studied the pH-dependent behavior of a pentablock terpolymer PMMA-*b*-PAA-*b*-P2VP-*b*-PAA-*b*-PMMA (PAA and P2VP are poly(acrylic acid) and poly(2-vinyl pyridine)), where the middle PAA-*b*-P2VP-*b*-PAA represents a polyampholytic triblock copolymer, end-capped with hydrophobic PMMA blocks.[138] It was found that the nature of the networks is strongly related to the pH value, which was attributed to the protonation/deprotonation of ionizable segments inside the central polyampholytic triblock copolymer. Moreover, pronounced differences in rheological properties of obtained hydrogels were detected. The authors correlate their findings with the nature and length of the bridging chains in the network: both at low and high pH, the hydrogel represents a network, consisting of hydrophobic PMMA cores, which act as physical cross-links, bridged by elastically active chains. At low pH, these contain longer protonated P2VP and shorter non-ionic PAA blocks. Strong stretching of the P2VP blocks promotes a high connectivity in the system and leads to the formation of a strong gel. At high pH, the bridging chains are constituted of deprotonated PAA blocks together with non-ionic hydrophobic P2VP blocks, which induces a bridge-to-loop transition, resulting in a weaker gel. Therefore, the authors have shown that, by varying pH, it

is possible to transform a positively charged, free-standing gel to a negatively charged, less stiff network.

Similar findings were observed by Stavrouli et al. in their studies on hydrogels from a similar pentablock terpolymer containing a triblock polyampholyte PAA-*b*-P2VP-*b*-PAA with additional hydrophobic PMMA end-blocks.[139] The pH-responsivity was related to the varying degree of electrostatic interactions inside the polyampholytic block, while the thermothickening phenomenon was attributed to the enhanced mobility of the PAA blocks at temperatures above their upper critical solution temperature (UCST), which facilitates their electrostatic associations with the P2VP blocks and leads to a strengthening of the network.

Thus, self-assembled hydrogels from telechelic polymers with a polyampholyte block represent highly pH-responsive systems, whose properties can be further tuned in order to fit special applications, for instance, by introducing thermo-responsive monomers into the polyampholytic middle blocks.[144,145] It was shown that the presence of a temperature-sensitive comonomer can influence the properties of a pH-sensitive copolymerized monomer and vice versa, which can significantly broaden the range of T/pH sensitivity.

A very interesting example is presented in the studies of Feil et al. on hydrogels comprising the temperature-sensitive N-isopropylacrylamide (NIPAAm) and the pH sensitive (diethy1amino)ethyl methacrylate (DEAEMA) together with a hydrophobic butyl methacrylate (BMA) component: P(NIPAAm-co-BMA-co-DEAEMA).[144] Whereas the former two influence the swelling of the gel, the latter BMA component enhances the mechanical properties of the gel. The authors demonstrated the influence of temperature on the pH-sensitive swelling, which was attributed to the effect of temperature on the pK_b of DEAEMA. Further investigations have shown that copolymerization with a thermosensitive monomer leads to a decrease in the basicity of DEAEMA with increasing temperature, which was attributed to the increased hydrophobicity of PNIPAAm upon increase in temperature. Moreover, it was shown that the LCST of P(NIPAAm-*co*-BMA-*co*-DEAEMA) is pH dependent, due to the varying charge density on DEAEMA. This means that the temperature range in which swelling of the gel occurs depends on the amount of ionizable DEAEMA segments.

A similar effect of copolymerized pH sensitive acrylic acid (AA) with *N*-isopropylacrylamide (NIPAAM) on its LCST was shown by Bulmus et al.[145] An increase in the LCST of the copolymer with increasing AA content was related by the authors to the hydrophilic nature of the acrylic acid at all pH ranges.

3. Characterization techniques

In present chapter we will discuss the main principles of three different techniques, which were used for studies of present systems. The mechanical behavior of hydrogels was addressed by rheological studies. With the aim to establish the internal structure, or the origin of observed mechanical properties, small-angle neutron measurements were performed. Moreover, the dynamic behavior of hydrogel networks was examined by dynamic light scattering also in rotational mode.

3.1. Rheology

The present chapter 3.1 is based on refs. [146-148].

Rheology studies the deformation and flow of materials under applied force.[149] The goal of rheology is to quantify the dynamic behavior over a wide range of parameters and to relate it to the internal material structure. Depending on the mechanical response to aplied stress or strain, materials can be classified as elastic, viscous and viscoelastic. According to the Hookes description, an ideal elastic material behaves as a solid, and its extension is proportional to applied stress, and it returns to its initial state after the termination of load. In contrary to an elastic material ideal liquid exhibits permanent flow while exposed to the load and its flow rate is proportional to the load. In real life most of the materials do not exhibit ideal solid or ideal liquid behavior, but viscoelastic. As a result, both stress and strain are functions of time and extent of deformation.[150]

The most frequently used experiments for studying the viscoelastic behavior of materials include creep, stress relaxation and dynamic techniques. In creep experiment a constant stress is applied to the material and the strain is recorded as a function of time. In the stress relaxation test, the material is subjected to a constant deformation, and the stress decay is recorded as a function of time. Dynamic technique implies the use of periodically varying stress or deformation, whereas the phase-dependent oscillatory response is measured.

3.1.1. Steady-state shear flow

In figure 3.1a, the steady shear deformation is presented. At time t = 0, the bottom plate is fixed, and the upper plate is made to gain a constant velocity, v. This results in a generation of the shear stress, τ, inside the fluid between the plates. The fluid starts to flow. The shear rate, $\dot{\gamma}$, will be constant throughout the fluid and is estimated as v/h, where h is the distance between the plates (fig. 3.1a).

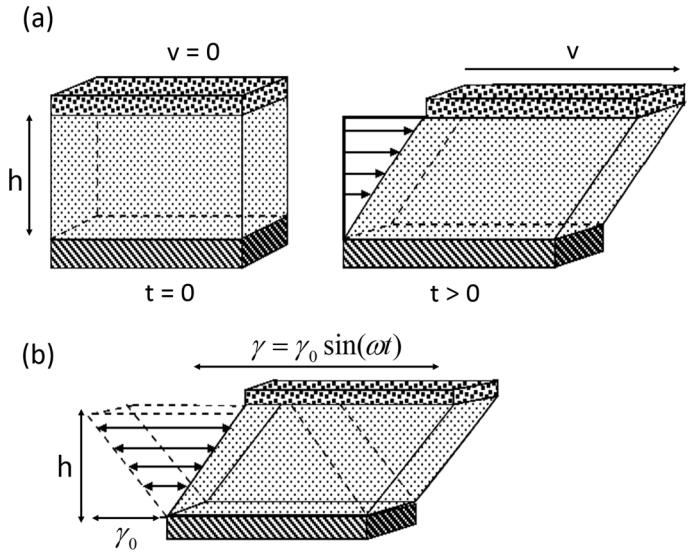

Fig. 3.1: Two types of shear deformation: steady shear (a) and dynamic (oscillatory) shear (b). See description in text. Modified from Ref. 147.

In a steady shear experiment, a steady shear stress is applied to the material, and the resulting shear rate is monitored. The data is collected, when the material has reached steady state flow (equilibrium conditions). The most important parameter, deduced from the steady-shear flow experiment, is the viscosity. It is given by the by the ratio of applied shear stress to the shear rate and reported as a function of the shear rate (or shear stress):

$$\eta(\dot{\gamma}) = \frac{\tau}{\dot{\gamma}}. \tag{3.1}$$

A plot of viscosity versus shear rate or shear stress is called a flow curve (fig. 3.2). For the ideal viscous flow, the viscosity is independent of the shear rate (fig. 3.2a). This behavior is characteristic for Newtonian liquids, or homogenous fluids with low molecular weights.[149] Nevertheless, a lot of real systems are non-Newtonian liquids, and the viscosity is not a constant, but depends on the rate and the time of the action of applied shear stress. The materials, which

do not exhibit a yield stress, but instead flow instantaneously under applied stress, are called pseudoplastic. The flow is accompanied by decrease in viscosity increasing shear rate. This is called a shear-thinning. Among these materials are polymer solutions. In the simplest case, the sample shows the Netwonian behavior at low shear rates, followed by a shear thinning at higher shear rates (fig 3.2b). At low shear rates viscosity has a constant value η_0, called the zero-shear viscosity. After the critical shear rate ($\dot{\gamma}_c$) is reached, the viscosity of the sample decreases.

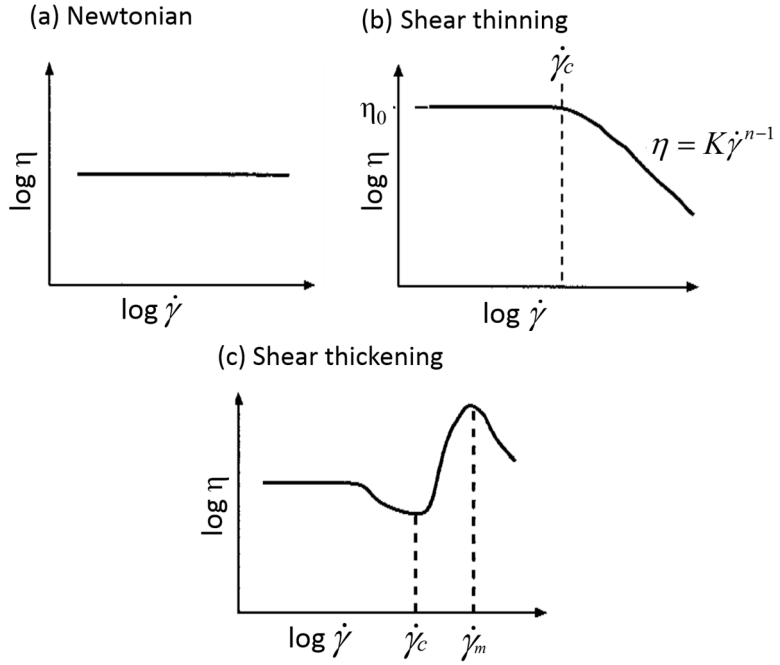

Fig. 3.2: Material behavior under steady shear: Newtonian (a), shear thinning (b) and shear thickening (c). Taken from Ref. 147.

For modeling the steady-shear response, often the Power law model is used:

$$\eta = K\dot{\gamma}^{n-1} \tag{3.2}$$

where K is a consistency, n is the power law index and characterizes the particular behavior of the material. Thus, $n = 1$ manifests the Newtonian behavior; $n < 1$ is characteristic for shear-thinning process in case of pseudoplastic fluids, $n > 1$ defines shear-thickening process. Shear thickening is observed less frequently and is characterized by the increase in the material viscosity increasing the shear rate. The materials are classified as dilatant (fig. 3.2c). At a critical shear rate $\dot{\gamma}_c$ the viscosity starts to increase, until it reaches a maximum at a shear rate, $\dot{\gamma}_m$, above which viscosity starts to drop. Shear thickening often occurs as a result of phase separation or structure rearrangements in material.

3.1.2. Dynamic shear flow

As we mentioned before, for most of real materials the mechanical behavior is a function of time and rate of deformation. At low rate of deformation, behavior of most of the soft materials is viscous, whereas at higher rates material exhibits elastic behavior. This phenomenon of viscoelasticity can be addressed by dynamic testing, like oscillatory stress or strain measurements.

In dynamic shear flow test (fig. 3.1b), the deformation of oscillating frequency ω is applied to the material, and the strain response can be written as:[151]

$$\gamma = \gamma_0 \sin(\omega t) \tag{3.3}$$

where γ_0 is the maximum amplitude of the strain and ω is in rad/s or $\omega / 2\pi$ in Hz. In a dynamic experiment the strain amplitude, imposed on the sample is minimal and within its linear viscoelastic regime (LVR). It means that stress is linearly proportional to the imposed strain. Then shear stress, generated by oscillatory strain, is also sinusoidal and is given by:

$$\tau = \tau_0 \sin(\omega t + \delta) \tag{3.4}$$

where τ_0 is the maximum amplitude of shear stress and δ is the phase angle shift of stress in respect to strain. In figure 3.3, the curves for oscillating stress and strain are presented as a function of time.

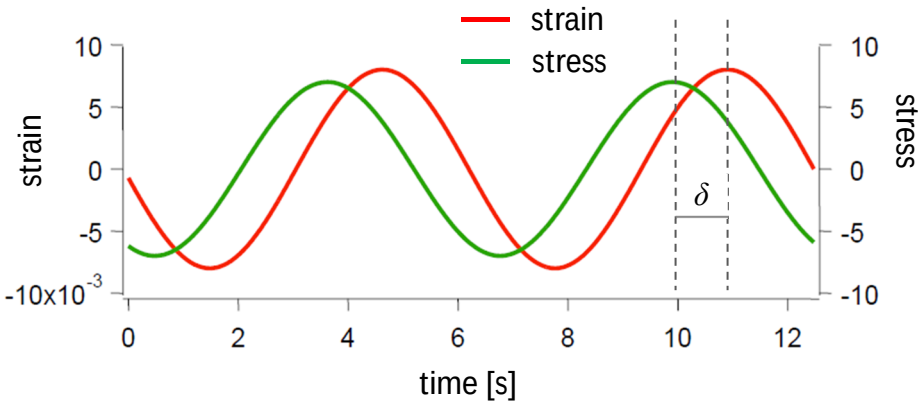

Fig. 3.3: Oscillatory applied strain (γ) wave and the resulting stress wave (τ) with the phase angle shift δ. Modified from Ref. 152.

For an ideally elastic material the maxima of stress and strain coincide and are in phase, $\delta = 0°$. If the material is purely viscous, the phase shift between stress and strain is of $\delta = 90°$. Viscoelastic materials have an intermediate behavior between these two extremes,

$0° < \delta < 90°$. From Eq. 3.4 the resulting stress wave can be written as a sum of in-phase and out-of-phase with the strain components:

$$\tau = \tau_0 \sin(\omega t)\cos(\delta) + \tau_0 \sin(\delta)\cos(\omega t) \tag{3.5}$$

or:

$$\tau = \gamma_0 \left[\left(\frac{\tau_0}{\gamma_0} \cos(\delta) \right) \sin(\omega t) + \left(\frac{\tau_0}{\gamma_0} \sin(\delta) \right) \cos(\omega t) \right]. \tag{3.6}$$

From Eq. 3.6, the dynamic storage modulus can be written as:

$$G' = \frac{\tau_0}{\gamma_0} \cos(\delta). \tag{3.7}$$

It is related to the stress in-phase with the displacement and carries all information about elastic nature of material. The loss modulus is related to the stress component being out-of-phase with the strain, and contains the information about the dissipation of energy by the material:

$$G'' = \frac{\tau_0}{\gamma_0} \sin(\delta). \tag{3.8}$$

Eq. 3.6 can be rewritten as:

$$\tau = \gamma_0 G' \sin(\omega t) + \gamma_0 G'' \cos(\omega t). \tag{3.9}$$

For purely elastic material $G'' = 0 \quad (\delta = 0^\circ)$, for purely viscous $G' = 0 \quad (\delta = 90^\circ)$. For viscoelastic material both elastic and loss moduli have non-zero values. The ratio of these two moduli is equal to the tangent of the phase angle and characterizes the viscoelastic behavior of the particular material, or the strength of material:

$$\tan(\delta) = \frac{G''}{G'}. \tag{3.10}$$

Thus, when it is less than 1, the particles are strongly associated, which can lead to a sedimentation. The value of $\tan(\delta)$ higher than 1 suggests the particles are uncorrelated. Stable solution is characterized by $\tan(\delta)$ of intermediate value.

The complex viscosity is defined as:

$$\eta^* = \left[\left(\frac{G'}{\omega} \right)^2 + \left(\frac{G''}{\omega} \right)^2 \right]^{1/2}. \tag{3.11}$$

The complex viscosity varies with frequency analogously to the steady viscosity versus shear rate.

Amplitude and frequency sweep

There are different types of oscillation tests, which are used to determine the strength and stability of a material. In order to investigate truly material functions, the tests have to be performed within the linear viscoelastic region (LVR). In this manner, the strain does not exceed the critical value, above which the elastic structure is destroyed. In order to determine the LVR, the amplitude sweep over a strain (or stress) range is performed (fig. 3.4a). During an amplitude sweep the amplitude of the deformation (or the amplitude of the shear stress) is varied, while the frequency is kept constant. In figure 3.4a, the storage modulus G' and the loss modulus G'' are plotted as a function of the deformation.

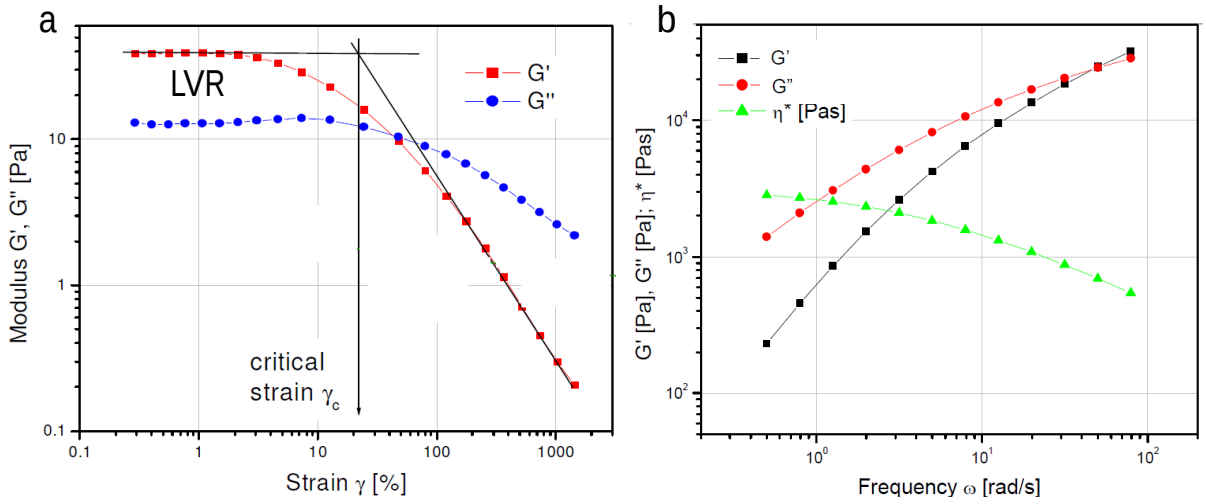

Fig. 3.4: Examples of the oscillatory tests (on cosmetic cremes): amplitude (a) and frequency (b) sweeps. Taken from Ref. 153.

At low deformation, the sample structure is maintained, and the G' and G'' moduli are constant (LVR). When the applied deformation becomes too high, structure is disturbed and both moduli start to decrease. The plateau value of G' in the LVR-region can give information about rigidity of the sample at rest, while the one of G'' gives the information about the viscosity of the unsheared sample. Additional information can be obtained from the ratio of the two moduli. Thus, if $G' > G''$ (in LVR), the sample has the properties of a viscoelastic solid. $G'' > G'$ indicates that sample behaves like a viscoelastic fluid. The point of the intersection of the curves for G' and G'' defines the yield point. After the LVR is determined, a frequency sweep at a given stress/strain is performed with the aim to determine the nature of the material (fig. 3.4b).

In the frequency sweep experiment, the frequency is varied while the amplitude of the deformation (or the amplitude of the shear stress) is kept at a desired value (determined in a strain sweep). Frequency sweep measurements of polymer hydrogels at various temperatures can give an information about their melting point, glass transition, viscoelastic characteristics, inter-particle forces and entanglement density.[154] For colloidal dispersions information about their sedimentation stability can be achieved.

Figure 3.5 shows the difference in moduli behavior for three types of materials.[147] Figure 3.5a represents a stabilized dispersion with no interparticle interactions. It can be seen that $G'' > G'$ for all the values in studied frequency range. From the slope it is possible to estimate which modulus will prevail in a certain frequency range. Figure 3.5b represents the case of weakly flocculated dispersion. The particle interaction forces are not negligible now, and the behavior of moduli is not so trivial. Thus, at low frequencies, $G'' > G'$, while the situation changes above a certain frequency value, where $G'' < G'$, manifesting the viscoelastic nature of material. The frequency at which there is a crossover of G' and G'' defines the longest relaxation time of the material, or the time, required for the stress to relax. Figure 3.5c represents the case of strongly interacting particles, like polymer hydrogels. Now both moduli are almost frequency independent, while $G' > G''$ in all studied frequency range.

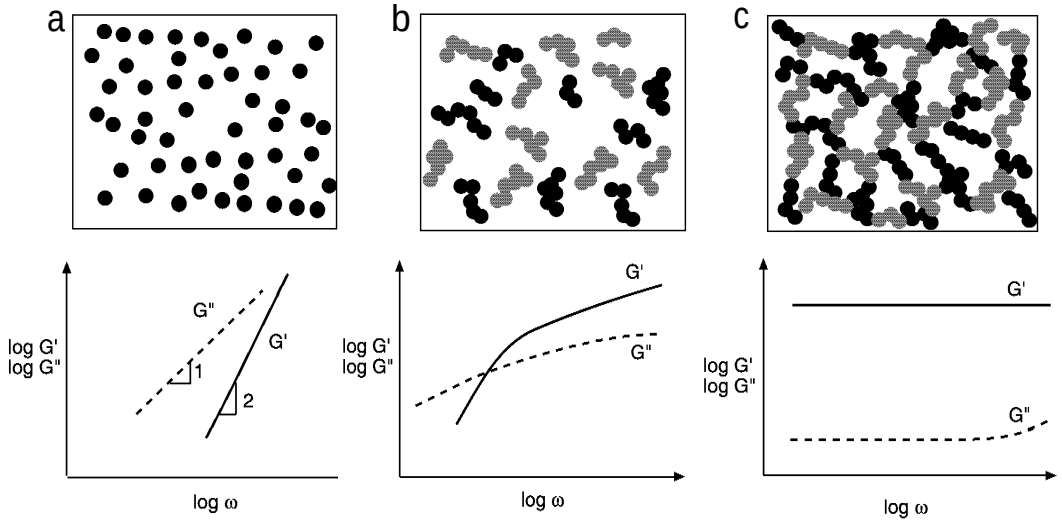

Fig. 3.5: Colloidal dispersions and corresponding elastic G' and loss G'' moduli as a function of angular frequency for (a) stabilized dispersion, (b) weakly flocculated dispersion and (c) gel. Modified from Ref. 147.

Thus, dynamic rheology is directly related to the material microstructures at rest or at small deformations in comparison to steady rheology, where the material properties are studied under the flow.

3.1.3. Creep

Another category of unsteady shear testing includes a transient shear testing, like creep. In a creep experiment, the instantaneous stress is increased from 0 to τ_0 (usually small loads), and the change in a strain (creep) is observed over time (fig. 3.6). The polymeric materials deform continuously, reaching a steady rate of straining, $\dot{\gamma}_\infty$ (fig. 3.6b). The data is usually expressed in terms of compliance, $J(t)$ (fig. 3.6c):

$$J(t)=\gamma(t)/\tau_0 \quad . \tag{3.12}$$

In a linear viscoelastic regime, strain is linear to stress, and resulting strain versus time at different τ_0 collapses into $J(t)$ plot.

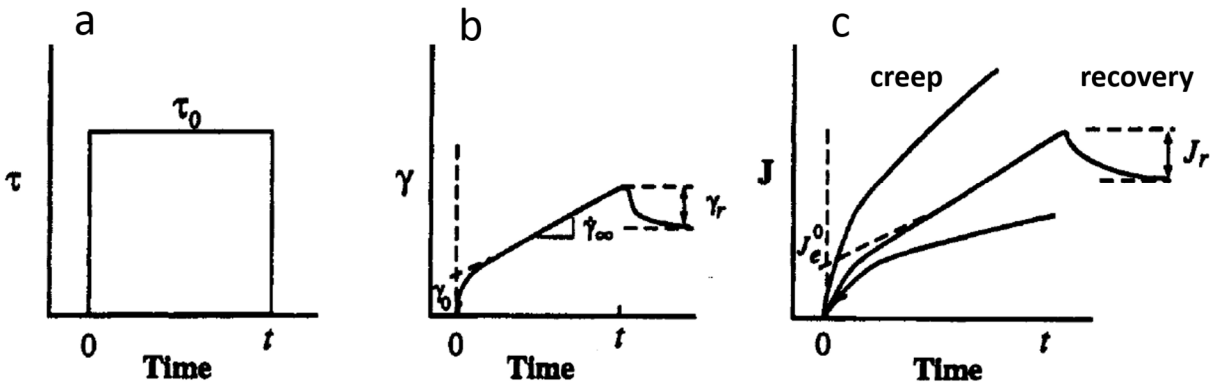

Fig. 3.6: Creep experiment. (a) Stress profile; (b) Strain as a function of time; (c) Data is plotted in terms of creep compliance. Modified from Ref. 148.

A steady state creep compliance J_e^0 is defined by extrapolation of the limiting slope to t = 0. The slope is inverse of the viscosity at low shear rate, η_0 . In a steady creeping regime:

$$J(t)=\frac{\gamma_0}{\tau_0}+\frac{\tau\dot{\gamma}_\infty}{\tau_0} = J_e^0+\frac{t}{\eta_0}. \tag{3.13}$$

or:

$$J(t)=\frac{1}{G_0}+\frac{t}{\eta_0} \tag{3.14}$$

where G_0 is the plateau modulus, reflecting structural information such as entanglements molecular weight in the network. As well, G_0 is related to another characteristic parameter of a viscoelastic system, *i.e.* its relaxation time, $\tau_R = \eta_0/G_0$, or the time, required for stresses to relax. In a viscous fluid under the deformation, the stresses relax instantaneously, whereas they never relax for an elastic solid.

3.1.4. Instrument

Rheological measurements of studied systems were performed on a stress controlled Rheometric Scientific SR 200 rheometer. The stress controlled rheometer applies a controlled stress (torque) on the sample, which leads to its deformation. As a result, probe rotates with a certain speed, which depends on the viscosity of material. The resulting angular displacement is measured by an optical encoder.

In figure 3.7a, the schematic representation of the instrument setup is depicted. During the measurement the test material is placed between two surfaces. The bottom surface is a plate, which is fixed. The upper surface has a variable geometry: parallel plates, cone and plate, concentric cylinders. The geometry shape selection is driven by the nature and the density of the material under the study. Thus, parallel plates geometry is often used for study of gels, soft materials; cylinders are used for fluids and other low-viscosity materials; cone and plate geometry is used for studies of liquids, dispersions and polymer hydrogels. In present study the cone and plate geometry was used (fig. 3.7b), which allows a homogeneous deformation of the sample, so the shear rate and the shear stress are position independent. The geometry is located on the end of the arm and rotates with a certain speed by a motor, so the load can be controlled. As we mentioned before the shear rate is constant over the entire sample and related to the frequency as:

$$\dot{\gamma} = \frac{\omega}{\alpha} \tag{3.15}$$

where α is the cone angle (fig. 3.7b). Varying the value of the angle it is possible to adjust the maximum shear rate.

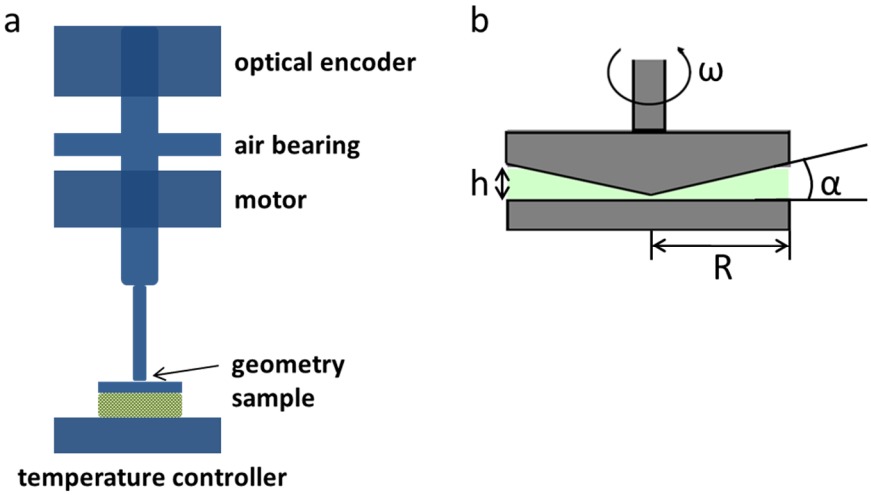

Fig. 3.7: (a) Schematic presentation of stress controlled rheometer; (b) cone and plate geometry. Adapted from Ref. 155.

The temperature control is performed by a Peltier control system.

Details of all experimental settings and scans will be given further in Chapters 4, 5 and 6.

3.2. Small-angle neutron scattering

The present chapter is based on refs. [156-158].

One of the most powerful methods of investigation the structure of materials at the mesoscopic scale (1 nm - 1 μm) is small-angle neutron scattering. This is induced by numerous advantages of this technique: non-invasiveness; possibility to extract structural information, averaged over the whole sample; and one of the most important, possibility to obtain some of the physical quantities (volume, surface and etc.) using model-free approach.[157] The fact that neutrons are unaffected by the charge of electrons, but interact with a nucleus on very short distances, gives an advantage of deep penetration, and, as a result, probing of the bulk properties of the material. Scattering with neutrons allows high scattering contrast between the particles and the matrix due to the big difference in scattering lengths of hydrogen and deuterium.[156]

The neutrons feature dual wave-particle nature. Neutrons have a mass equivalent to 1839 electrons (1.674928×10^{-27} kg), magnetic dipole moment of $-1.9130427\mu_n$ and a spin of ½.[158] The scattering of neutrons happens through the interaction with a nucleus or through the interaction with a magnetic moment of unpaired electrons with a magnetic moment of the neutron. Here we will focus on the elastic scattering from a nucleus.

3.2.1. Elastic scattering

The present chapter is based on refs. [158,159].

In order to understand how the atomic structure of the sample relates to the measured signal let us consider the scattering of the neutron beam from the single nucleus. We assume that nucleus is rigidly fixed at the origin of coordinates, which means that it cannot move and exchange the energy. The final scattering is related to the interaction potential between the neutron and nucleus, separated by r. The potential is a short ranged, and vanishes over a distance of $\sim10^{-15}$ m. Due to the fact that it is several orders of magnitude lower than the neutron wavelength (~1Å = 10^{-10} m), nucleus behaves as a point scatterer (fig. 3.8).

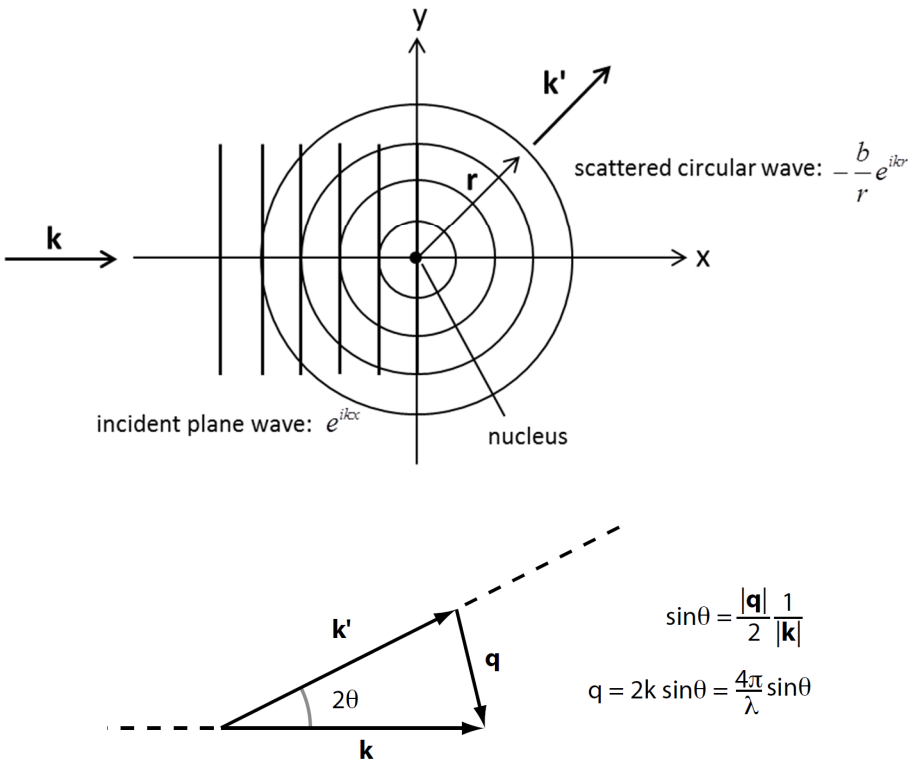

Fig. 3.8: Elastic neutron scattering from a fixed nucleus. Modified from Ref. 160.

The beam of neutrons can be represented by a plane wave with a wave-function:

$$\psi_i = e^{-ikx} \tag{3.16}$$

where x is the distance from the nucleus. $k = 2\pi/\lambda$ is the wave-number. Scattering from a nucleus as a point scatterer results in a spherically symmetrical wave-function:

$$\psi_s = -\frac{b}{r}e^{-ikr} \tag{3.17}$$

where b is the nuclear scattering length. This is so called efficiency of neutron scattering by a nucleus. The value of scattering length does not depend on the wavelength of the incident beam of neutrons. The strength of the nucleus-neutron interaction is mainly determined by the nuclear structure, but not the atomic number. As a result there is no direct correlation between the magnitude of the scattering length and atomic number or mass of the element. The value of one element can significantly differ from the one of neighboring element, including isotopes of the same element. For instance, hydrogen ^{1}H has a coherent scattering length of -3.74×10^{-5} Å, but its isotope, deuterium ^{2}H (D) 6.67×10^{-5} Å. The technique of contrast variation is based on the idea of moderating the scattering length of the material by replacing hydrogen with deuterium.

Above presented case was considered for a single nucleus; for a three-dimensional assembly of nuclei the scattered wave is given by:

$$\psi_s = -\sum_i \left(\frac{b_i}{r}\right) e^{ikr} e^{i\vec{q}\cdot\vec{r}} \tag{3.18}$$

with a scattering vector $\vec{q} = \vec{k}_i - \vec{k}_s$, where $\vec{k}_i$ and $\vec{k}_s$ are the wave-vectors of the incident and scattered neutrons. In case of elastic scattering (fig. 3.8), there is no exchange of energy and $\left|\vec{k}_i\right| = \left|\vec{k}_s\right|$. From the triangle representation in fig. 3.8, the momentum transfer q can be calculated as:

$$q = \frac{4\pi \sin\theta}{\lambda} \tag{3.19}$$

where 2θ is the angle between $\vec{k}_i$ and $\vec{k}_s$, through which the scattering particle is deflected.

3.2.2. Scattering cross section

The present chapter is based on refs. [158-159,161].

In case radiation is scattered by a point source, considered earlier, the scattered wave is spherical. In this case, the flux is practical to consider as the amount of energy transmitted per second through a solid angle, but not per area as in case of a plane wave. In other words, the flux becomes independent of the distance from the source and is given by the total number of neutrons scattered per solid angle and in one second. In figure 3.9, it is shown the incident plane wave of flux, and the resulting spherical wave, scattered in all directions.

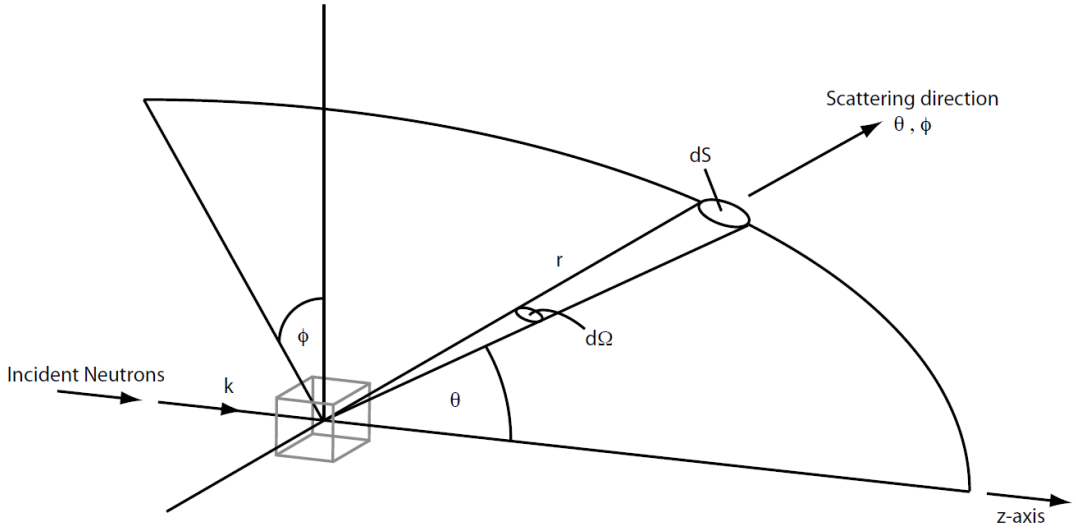

Fig. 3.9: The geometry of the scattering experiment. From Ref. 162.

The probability that a neutron will be scattered by a nucleus into a solid angle $d\Omega$ in the given direction θ,ϕ is defined by a differential cross-section:

$$\frac{d\sigma}{d\Omega} = \frac{\text{number of neutrons scattered per second into } d\Omega \text{ in direction } \theta,\phi}{\Phi d\Omega} \tag{3.20}$$

where Φ is the number of neutrons in incident flux per unit area per second. The dimensions of flux are in [area^{-1} time^{-1}] and of numerator are in [time^{-1}], which gives the dimensions of area for cross section: [area^{-1}]. After integration the differential scattering cross section over the solid angle we obtain the total scattering cross section, or the quantity, measured in a scattering experiment:

$$\sigma_S = \frac{\text{total number of neutrons scattered per second}}{\Phi}. \tag{3.21}$$

In order to derive the cross section for a molecule as a system of nuclei, let us first derive the cross section for scattering from a single nucleus. The number of neutrons scattered into an area dS per second is given by:

$$\upsilon dS \left|\psi_S\right|^2 = \upsilon dS \frac{b^2}{r^2} = \upsilon b^2 d\Omega \tag{3.22}$$

where υ is the velocity of neutrons. The incident neutron flux is given by:

$$\Phi = \upsilon \left|\psi_i\right|^2 = \upsilon. \tag{3.23}$$

From Eq. 3.20 the differential cross section is related to the scattering length density:

$$\frac{d\sigma}{d\Omega} = \frac{\upsilon b^2 d\Omega}{\Phi d\Omega} = b^2. \tag{3.24}$$

The differential cross-section for the assembly of nuclei with a wavefunction, given in Eq. 3.18 is a function of q and is given by:

$$\frac{d\sigma}{d\Omega}(\vec{q}) = \frac{1}{N}\left|\sum_i^N b_i e^{i\vec{q}\cdot\vec{r}}\right|^2. \tag{3.25}$$

Due to the fact that the wavelength in SANS is bigger than the atomic distance, the polymer can be represented as a worm with a constant scattering length density over the whole molecule:

$$\rho = \frac{1}{V}\sum_{i\in\{mol\}} b_i \tag{3.26}$$

where b_i is the scattering length density of the atom and V is the volume of the molecule. Considering all atoms inside the molecule and normalizing by the molecule volume we obtain a macroscopic cross section:

$$\frac{d\Sigma}{d\Omega}(\vec{q}) = \frac{N}{V}\frac{d\sigma}{d\Omega}(\vec{q}) = \frac{1}{V}\left|\int_V \rho(\vec{r})e^{i\vec{q}\cdot\vec{r}}d\vec{r}\right|^2 . \quad (3.27)$$

In case of the system with two phases of different scattering length densities, ρ_1 of a polymer and ρ_2 of a medium, we obtain:

$$\frac{d\Sigma}{d\Omega}(\vec{q}) = \frac{1}{V}(\rho_1 - \rho_2)^2\left|\int_V e^{i\vec{q}\cdot\vec{r}}d\vec{r}\right|^2 . \quad (3.28)$$

The first contrast factor describes the interference of neutrons scattered from different parts of the object, and describes the shape and size of scattering objects, whereas the integral term describes the positions of different scattering objects.

3.2.3. Coherent and incoherent cross section

The present chapter is based on refs. [156,158-159].

Above presented section considers only scattering from one isotope of one element. Real systems represent a mixture of isotopes with *b* varying from nucleus to nucleus. In case when the element consists of a single isotope, but the nuclear spin of an isotope is non zero, the nucleus has either b^+ or b^- scattering length. If the neutron with a spin of 1/2 interacts with a nucleus with a spin *i*, the system will have a resulting spin of *i*+1/2 or *i*-1/2. Each spin state, and therefore, each scattering length b^+, has a certain probability. As a consequence of such irregularity in scattering lengths there are coherent and incoherent contributions to a scattering signal:

$$\frac{d\sigma}{d\Omega}(\vec{q}) = \langle b\rangle^2 \sum_{j,k} e^{iq(\vec{r}_j - \vec{r}_k)} + N(\langle b^2\rangle - \langle b\rangle^2) . \quad (3.29)$$

The coherent first term is the total intensity which would have been detected at condition that all nuclei have the same scattering length of $\langle b\rangle$. It is dependent on position of atoms, *r*, therefore, it contains the structural information. The second term does not have *r* dependence, and proportional to $\langle b^2\rangle - \langle b\rangle^2$, in other words, it is related to the divergence in scattering length.

The cross section is connected to *b* as:

$$\sigma_{tot} = 4\pi \left\langle b^2 \right\rangle . \tag{3.30}$$

Therefore we can write the new expressions for coherent and incoherent cross sections as:

$$\sigma_{coh} = 4\pi \left\langle b \right\rangle^2 , \tag{3.31}$$

$$\sigma_{incoh} = 4\pi (\left\langle b^2 \right\rangle - \left\langle b \right\rangle^2) . \tag{3.32}$$

Both values are known for some common elements, like ^{1}H, ^{2}D, P. The huge difference in cross section of deuterium and hydrogen is unique and advantageous for studies of polymers. SANS of polymers in deuterated water as a medium allows a high contrast between the material and medium, possible without chemical modification of material.

3.2.4. Resolution function

The present chapter is based on refs. [157,163].

An intention to have a fast data acquisition or in other words, high flux of radiation, leads to the utilization of broad wavelength monochromators or relaxed collimation of the incident beam. This results in a wide distribution of scattering vectors and pronounced smearing of a scattering curve.

The scattering vector resolution as a result of the wavelength spread can be obtained by a Taylor expansion of the expression for *q* with respect to the wavelength (Eq. 3.19):

$$\Delta q = -q\Delta\lambda / \lambda . \tag{3.33}$$

It can be seen that variance in scattering vector increases with q. The same procedure with respect to the scattering angle results in:

$$\Delta q = \frac{4\pi}{\lambda} \cos\theta \Delta\theta \approx \frac{4\pi}{\lambda} \Delta\theta \tag{3.34}$$

where $\Delta\theta$ is related to the beam width. It can be seen that distribution of q from collimation discrepancy is q independent at low scattering angles. Assuming that different contributions are mutually independent, the variance of the resolution function is given by:

$$(\Delta q)^2 = q^2 \left[\left(\frac{1}{2\sqrt{2\ln 2}} \frac{\Delta\lambda}{\lambda} \right)^2 \right] + \left[\left(\frac{4\pi}{\lambda} \right)^2 - q^2 \right] (\Delta\theta)^2 . \tag{3.35}$$

It can be seen that at low values of q the variance in q is determined by angle spread, while at higher q it is dominated by the wavelength resolution. The wavelength spread can be measured by a chopper or in time of flight experiment, whereas the second contribution from a variation in scattering angle can be addressed by measuring the direct beam. The resolution function is given by:

$$R(q,q') = \left(\frac{1}{2\pi(\Delta q)^2}\right)^{1/2} \exp\left(-\frac{(q'-q)^2}{2(\Delta q)^2}\right). \quad (3.36)$$

The smeared intensity is given by the 1D convolution smearing integral as:

$$\left[\frac{d\Sigma(q)}{d\Omega}\right]_{smear} = \int_0^\infty dq' R(q,q') \frac{d\Sigma(q'-q)}{d\Omega}. \quad (3.37)$$

3.2.5. Instrument

The present chapter is based on refs. [163-165].

Measurements were performed on several small-angle neutron diffractometers: KWS-1 and KWS-2, operated by the Jülich Centre for Neutron Science (JCNS) outstation at Heinz Maier-Leibnitz Zentrum (MLZ) in Garching, and D22 instrument at Institut Laue Langevin (ILL) in Grenoble. The instruments are designed for studies of material structure at a mesoscopic scale in a wide q-range. The high intensity allows precise measurements of weakly scattering materials.

KWS-1/KWS-2. The instrument has a pinhole geometry, which permits a wide range of momentum transfer 7×10^{-4} Å^{-1} < q < 0.5 Å^{-1}, which could be achieved varying both sample detector distance (SDD = 1 - 20 m) together with a wavelength (λ = 4.5 - 20 Å). Schematic representation of the KWS-1 instrument setup is given in figure 3.10. The neutron beam is monochromatized by a velocity selector with a wavelength resolution of $\Delta\lambda/\lambda$ = 10%. For experiments, where higher resolution is requested, the double-disc chopper with adjustable opening slits is installed. It allows to diminish the wavelength spread from 10% to 1%. Collimation of the resulting beam is performed in the 20 m long collimation tube, which contains the system of 18 neutron guide sections 1 m long each and five apertures. The guides allow variation of source to the sample distance. The collimation of the neutron beam is performed by the system of apertures with the opening varying from 1×1 mm^2 to 50×50 mm^2 and square or rectangular shape, allowing different geometry of the beam. High intensity of the

beam and wider *q*-range is achieved through the use of focusing MgF_2 lenses. Afterwards the signal is recorded by a position sensitive ^6Li scintillation detector with a 64 × 64 cm^2 area and a pixel size of 5.25 mm. The setup includes one 50 × 50 mm beamstop, inserted into a detector, together with a mobile 70 × 70 mm beamstop. Both of them have a window for a ^3He counter, allowing the determination of the intensity of the direct beam for transmission measurements. The detector can be moved closer or further from a sample, as well it can be moved horizontally and laterally. The polarizer is installed for polarized neutron experiments, while the spin flipper is implemented with an aim to flip neutron polarization. The main difference of KWS-2 from KWS-1 is its lower wavelength resolution $\Delta\lambda/\lambda$ = 20%, which is nevertheless reasonable and acceptable value for scattering from polymeric systems in comparison with a highly ordered systems, where higher resolution is required.

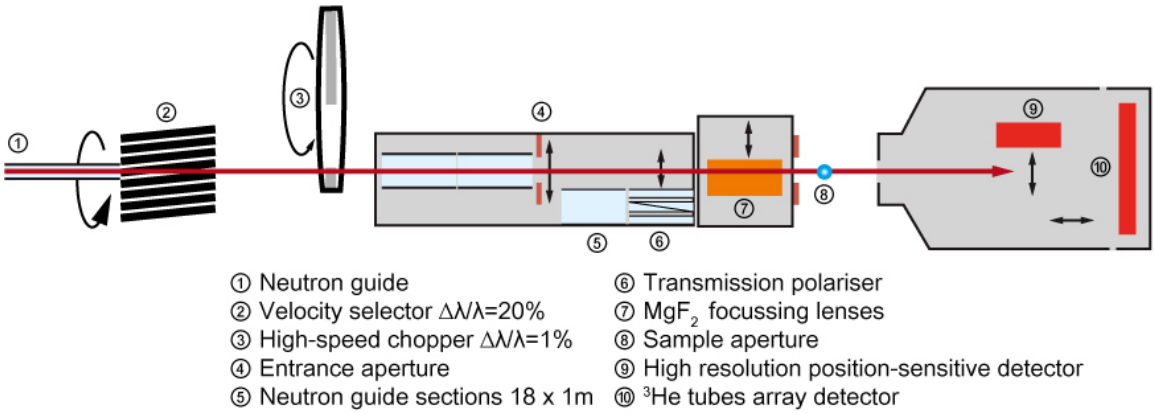

Fig. 3.10: Schematic representation of the KWS-1 instrument setup. From Ref. 166.

D22. The instrument exhibits the same pinhole standard working method as KWS-1/KWS-2. The mechanical velocity selector permits a wavelength range between 4.5 and 40 Å with a wavelength spread of $\Delta\lambda/\lambda$ = 10%. The velocity selector is followed by a number of horizontally and vertically oriented slits, which subsequently define the size of the beam. Collimation of the beam is done by a system of waveguides. By removing or adding the part of collimation it is possible to adjust the neutron flux. In the end the neutron beam is defined by an aperture, located in front of the sample. The scattered neutrons are recorded by a large area 128 × 128 ^3He detector with a pixel size of 8 × 8 mm^2. As in case of KWS-1/KWS-2 a B_4C and cadmium beam-stop are mounted in front of the detector aiming protection of the latter one from beam damage. Variation of wavelength range together with the sample to detector distances allows a *q*-range of $8 \cdot 10^{-4}$ $Å^{-1}$ to 0.8 $Å^{-1}$.

3.2.6. Data analysis

In present chapter we will consider models, which were used for fitting the small-angle neutron scattering curves. Several form factors and structure factors will be demonstrated. The choice of a particular form or a structure factor in each case will be explained further in Chapters 4, 5 and 6.

3.2.6.1. Model-free approach

Guinier law

Present chapter is based on refs. [156-159].

In case shape of particles is not known or it is irregular, the scattering function in the limit of small $q << 1/R_g$ can be described as:

$$P_G(q) = I_G(q)\exp\left(-\frac{1}{3}q^2 R_g{}^2\right) \tag{3.38}$$

where I_G is the scaling factor, R_g the radius of gyration of the scatterer of unknown shape. Thus, it can be a polymer chain, a micelle or a domain in a complex system. This is so called Guinier law. An important limitation to the applicability of this law is that the system is dilute and isotropic, so there is no correlation between particles, and their orientations are random. The radius can be extracted from the slope of a plot of $\ln(P_G(q))$ vs q^2 as:

$$\ln(P_G(q)) = \ln(I_G(q)) - \frac{1}{3}q^2 R_g{}^2. \tag{3.39}$$

Porod law

Present chapter is based on refs. [156-159].

In case of hydrogel networks or any other concentrated systems strong forward scattering from large-scale inhomogeneities obscures the signal, which limits the studies of particle dimensions. Nevertheless the forward scattering can be modelled by a Porod law, which predicts that scattering from a particle with a smooth surface decreases as q^{-4}. Moreover, it allows the measurement of the total area S of the surface between two phases, in other words it considers the existence of the interface:

$$P_P(q) = \frac{I_P}{q^4} \approx \frac{2\pi(\Delta\rho)^2}{q^4}\frac{S}{V} \tag{3.40}$$

where I_P is the scaling factor, $\Delta\rho$ the scattering length density difference between the aggregates and solvent, and S/V the specific surface of the particles. In real systems the particle surface is not always perfect (smooth), which leads to a certain deviations from q^{-4} dependence. In order to describe the scattering from aggregates, whose surface is perturbed, the modified Porod law is valid:

$$P_P(q) = \frac{I_P}{q^{\alpha_P}} \tag{3.41}$$

with an exponent α_P, which contains information about dimensionality of scattering objects. Thus, $\alpha_P = 1$ characterizes the scattering from for rigid rods; slope between $2 < \alpha_P < 3$ is obtained for mass fractal (brunched systems, gel network); slope between $3 < \alpha_P < 4$ characterizes a surface fractal with a fractal dimension D with $\alpha_P = 6 - D$; $\alpha_P > 4$ denotes surface concentration gradient.

Guinier-Porod model

Present chapter is based on ref. [167].

When the shape of aggregates is not known, the Guinier-Porod model, derived from previously described two laws, can be utilized for fitting the data. It applies to spherical together with nonspherical asymmetrical scattering objects, like rods or lamellae, or even the intermediate shapes between them:

$$I_{PG}(q) = \begin{cases} P_G(q) = \dfrac{I_G}{q^s} \exp\left[-\dfrac{q^2 R_G{}^2}{3-s} \right] & \text{for } q \le q_1 \\ P_P(q) = \dfrac{I_P}{q^{\alpha_P}} & \text{for } q \ge q_1 \end{cases} \tag{3.42}$$

where I_G, I_P are the scaling factors of the two contributions; R_G the radius of gyration of the scatterer. The value q_1 is determined from the requirement of continuity of $I_{PG}(q)$ and its first derivative. Parameter s determines the symmetry of the scattering object. Thus, for 3D symmetry objects (spheres) $s = 0$, for 2D symmetry objects (rods) $s = 1$, for 1D symmetry objects (platelets) $s = 2$. $P_P(q)$ is again the modified Porod law, given previously in Eq. 3.41.

3.2.6.2. Form factors

The next three from factors were applied to describe the scattering from micelles. Depending on polymer structure and solvent conditions (pH, ionic strength), several slightly different architectures of scattering objects (micelles) were encountered (fig. 3.11). The reasons, leading to a particular shape formation will be discussed in each case separately further in Chapters 4, 5 and 6.

Form factors of spheres with a Gaussian distribution in size

In charged systems under consideration, micelles form as a result of electrostatically or hydrophobically driven self-assembly of polymer chains. The form factor of homogeneous spheres is the simplest possible form factor with only few parameters, which allows us to estimate the micellar dimensions. Fast spontaneous electrostatically driven complexation inevitably leads to a certain polydispersity in size of aggregates, which also must be taken into account. The intensity of scattering from homogeneous spheres with a Gaussian distribution in size *R*, is given by:

$$P_{sph}(q) = \left(\frac{4\pi}{3}\right)^2 N_0 \Delta\rho^2 \int_0^\infty f(R_{sph}) R_{sph}^6 F^2(qR_{sph}) dR_{sph} \tag{3.43}$$

where N_0 is the number of particles per unit volume; $\Delta\rho^2$ is the scattering length density difference between the particles and medium. Scattering length density from particles is considered to be uniform. The scattering amplitude of a homogeneous sphere is given by:

$$F(qR_{sph}) = \frac{3\left[\sin(qR_{sph}) - qR_{sph}\cos(qR_{sph})\right]}{(qR_{sph})^3}. \tag{3.44}$$

f(*R*) in Eq. 3.43 is the Gaussian distribution:

$$f(R_{sph}) = \frac{1}{\sigma\sqrt{2\pi}} \exp\left[-\frac{1}{2\sigma^2}\left(R_{sph} - \bar{R}_{sph}\right)^2\right] \tag{3.45}$$

where $\bar{R}_{sph}$ is the average radius, σ the width of the distribution, and $p = \sigma / \bar{R}_{sph}$ the corresponding polydispersity.

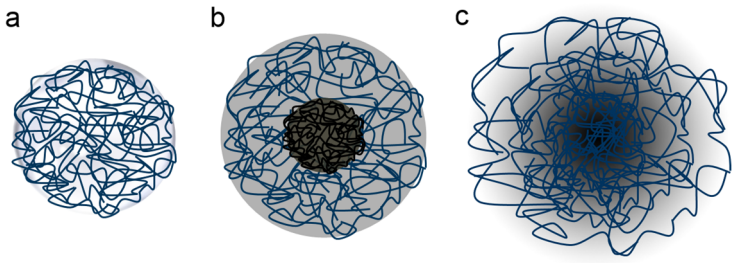

Fig. 3.11: Different architectures of scattering objects (micelles): homogeneous sphere (a), core-shell sphere (b) and fuzzy sphere (c).

Form factors of core-shell micelles

Present chapter is based on refs. [168,169].

In aqueous solutions, the amphiphilic molecules can self-assemble into various nanostructures with a different complexity. In charged systems, the final architecture of micelle is defined by several parameters, such as concentration, molecular geometry, pH and ionic strength. In non-balanced polyampholytes (with a non zero net charge), the electrostatically driven complexation involves only a certain amount of oppositely charged chains, whereas the rest of non-complexed but ionized chains stay outside of the hydrophobic "interpolyelectrolyte core", forming the shell with a different density. For these systems with a non-uniform distribution of chains inside the aggregate, the form factor of spherical core-shell particles was used:

$$P_{mic}(q) = \int_0^\infty G(R_c) P(q, R_c) dR_c \,. \tag{3.46}$$

where R_c is the radius of the core, $P(q, R_c)$ is the single particle form factor:

$$P(q, R_c) = \frac{1}{V_{mic}} \left[\frac{3V_c(\rho_c - \rho_{shell}) j(qR_c)}{qR_c} + \frac{3V_{mic}(\rho_{shell} - \rho_s) j(qR_{mic})}{qR_{mic}} \right]^2 \tag{3.47}$$

where R_{mic} is the radius of the micelle; ρ_c, ρ_{shell} and ρ_s are the scattering length densities of the core, the shell and the solvent, respectively; V_c, V_{mic} are the volumes of the core and the micelle, respectively. $j(x)$ is the first-order Bessel function:

$$j(x) = \frac{\sin x - x \cos x}{x^2} \,. \tag{3.48}$$

$G(R_c)$ in Eq. 3.46 is the normalized Schulz core size distribution:

$$G(R_c) = \frac{R_c^{\,z}}{\Gamma(z+1)}\left[\frac{z+1}{\overline{R_c}}\right]^{z+1} \exp\left(-\frac{(z+1)R_c}{\overline{R_c}}\right) \tag{3.49}$$

where $\Gamma(n)$ is the Gamma function and z is related to a polydispersity of the core, σ_c, defined as:

$$z = \left(\frac{\overline{R_c}}{\sigma_c}\right)^2 - 1. \tag{3.50}$$

Form factors of fuzzy spheres

Present chapter is based on ref. [170].

The model describes the particle as a spherical core with a fuzzy interface (fig. 3.11c), arising from the uneven distribution of polymer chains within the particle. The form factor is given by:

$$P_{Fuz}(q, R_c) = \frac{3\left[\sin(qR_c) - qR_c\cos(qR_c)\right]}{(qR_c)^3}\exp\left(\frac{-(\delta_{surf}q)^2}{2}\right) \tag{3.51}$$

where R_c is the radius of the core of the sphere; δ_{surf} is the width of the Gaussian, describing gradually decreasing particle surface, i.e. the fuzzy interface. Assuming Gaussian distribution of the core size, the average form factor is given by:

$$\overline{P}_{Fuz}(q) = \frac{1}{\sqrt{2}\sigma_c \overline{R_c}\,\overline{V^2}}\int dR_c V(R_c)^2 P_{Fuz}(q, R_c)\exp\left(-\frac{\left(R_c - \overline{R_c}\right)^2}{2\sigma_c{}^2\overline{R_c}^{\,2}}\right) \tag{3.52}$$

with

$$\overline{V^2} = \frac{1}{\sqrt{2}\sigma_c \overline{R_c}}\int dR_c V(R_c)^2 \exp\left(-\frac{\left(R_c - \overline{R_c}\right)^2}{2\sigma_c{}^2\overline{R_c}^{\,2}}\right) \tag{3.53}$$

where $\overline{R_c}$ is the average radius of the core and $V(R_c)$ is the volume of the core of the particle.

3.2.6.3. Structure factors

Percus-Yevick hard-sphere structure factor

Chapter is based on refs. [171-173].

In case of most of dilute solutions of scatterers there is no interparticle correlation, which means that the scattering signal does not depend on the spatial positions of the scatteres. In case of non-dilute solutions the interparticle contribution becomes important and has to be described in terms of interparticle structure factor:

$$S(q) = 1 + \frac{N}{V}\int_V (g(r) - 1)e^{-iqr}dr \tag{3.54}$$

where $g(r)$ is the pair distribution function for a pair of two correlated scattering particles. It gives the probability to find a scatterer at a distance r from the scatterer at the origin. $g(r)$ is related to the interaction potential, $U(r)$ as:

$$g(r) = e^{-\frac{U(r)}{k_B T}}. \tag{3.55}$$

Interaction potential includes many-body interactions: two-body, three-body, N-body. The direct interactions between two scatterers can be described by direct correlation function, $c(r)$, while interactions between these two scatterers through other scatterers are described by the total correlation function, $h(r)$. The total correlation function is related to the pair distribution function by:

$$h(r) = g(r) - 1. \tag{3.56}$$

In order to describe the interparticle contributions the Ornstein-Zernike approach is often used.[171,173] Ornstein-Zernike equation describes the relation between the total and direct correlation functions as:

$$h(q) = c(q) + \bar{N}\ c(q)\ h(q). \tag{3.57}$$

where $\bar{N} = N/V$ is the particle number density. Now the structure factor can be written as:

$$S(q) = 1 + \bar{N}h(q) = \frac{1}{1 - \bar{N}c(q)} \tag{3.58}$$

In order to obtain an expression for a structure factor the numerical solution of the Ornstein-Zernike equation has to be obtained. The equation includes two unknowns, $h(r)$ and $c(r)$, and can be solved while introducing another “closure” relation. Further we will consider Percus-Yevick and Mean Spherical approximations.

One of the structure factors, used in present study with the aim to describe the correlation between the particles in hydrogels, is the Percus-Yevick structure factor. It is the simplest possible structure factor, which contains only two fitting parameters, i.e. the lowest possible number, and allows us to qualitatively estimate the organization inside the network. The closure relation for Percus-Yevick approximation states:

$$c(q) = g(r)\left[1 - \exp\left(-\frac{U(r)}{k_B T}\right)\right]. \tag{3.59}$$

For two spheres of diameter *D*, the hard sphere potential is:

$$\begin{aligned} U(r) &= 0 \quad \text{for } r > D \\ U(r) &= \infty \quad \text{for } r < D \end{aligned}. \tag{3.60}$$

We do not present here the further calculations, they can be found in Ref. 172. The final expression for the Percus-Yevick hard-sphere structure factor is given by:

$$S_{HS}(q) = \frac{1}{1 + 24\eta G(2R_{HS}q)/(2R_{HS}q)} \tag{3.61}$$

where

$$\begin{aligned} G(x) = \gamma \frac{\sin x - x\cos x}{x^2} + \delta \frac{2x\sin x + (2 - x^2)\cos x - 2}{x^3} \\ + \varepsilon \frac{-x^4 \cos x + 4(3x^2 - 6\cos x + (x^3 - 6x)\sin x + 6}{x^5} \end{aligned} \tag{3.62}$$

with the help-functions:

$$\gamma = \frac{(1+2\eta)^2}{(1-\eta)^4},\ \delta = \frac{-6\eta(1+\eta/2)^2}{(1-\eta)^4},\ \varepsilon = \frac{\gamma\eta}{2} \tag{3.63}$$

where R_{HS} is the hard-sphere radius, i.e. half the center-to-center distance between the particles. η is the hard-sphere volume fraction, i.e. fraction of micelles which contribute to the formation of the micellar network.

Rescaled mean spherical approximation (RMSA) structure factor

Present chapter is based on refs. [174,175].

In case the charged particles present in solution, the strong long-range Coulomb interactions significantly influence the internal architecture of the hydrogel. The Coulomb repulsion between particles is given by:[176]

$$\upsilon(r) = \pi\varepsilon\varepsilon_0 D^2 \psi_0^{\ 2} \exp[-\kappa(r - D)]/r, \quad r > D \tag{3.64}$$

where ε is the dielectric constant, ε_0 the permittivity of the free vacuum, ψ_0 the surface potential, D the particle diameter, and r the interparticle center-to-center distance. $\kappa = 1/\lambda_D = [2e^2 10^3 NI/\varepsilon_0 \varepsilon k_B T]^{1/2}$ is the inverse Debye-Hückel screening length λ_D. e is the electronic charge, N the Avogadro number and $I = 1/2\sum c_i Z_i^2$ the ionic strength of solution with c_i and Z_i being the concentration and the valence of the i-th ion, respectively.

The surface potential, ψ_0, is related to the effective particle charge, Ze, by:

$$\psi_0 = Ze/\pi\varepsilon\varepsilon_0 D(2+\kappa D) \tag{3.65}$$

Rewriting $x = r/D$, $k = \kappa D$, $\beta = 1/\mathrm{k_B}T$, the reduced potential can be written as:

$$\beta\upsilon(x) = \gamma \exp(-kx)/x \tag{3.66}$$

with $\gamma = \beta\pi\varepsilon\varepsilon_0 D\psi_0^2 \exp(k)$ being a coupling constant.

The expression for Mean Spherical Approximation (MSA) closure relation in this case is given by:

$$\begin{array}{ll} c(r) = -\beta\upsilon(r) & \text{for } r > D \\ h(r) = -1 & \text{for } r < D \end{array}. \tag{3.67}$$

In case of highly charged systems, when $\gamma >> 1$, or charged systems at the very low concentrations, when $\eta \le 10^{-3}$, where $\eta = \pi D^3 n/6$ denotes the volume fraction, and n is number concentration of particles, solution of the mean spherical approximation (MSA) results in non-physical values for the pair distribution function, $g(r)$. Therefore, to obtain a valuable solution, it was proposed by Hansen and Hayter to introduce a new effective hard core, D' with $\eta' = \pi D'^3 n/6$, fixing the value of Coulomb coupling constant:

$$\Gamma_k = 2\beta\upsilon(r = 2a) \tag{3.68}$$

with $a = (3/4\pi n)^{1/3}$ being the mean interparticle spacing. Eventually, the final expression for rescaled mean spherical approximation (RMSA) structure factor can be given by:

$$S_{RMSA}(Q) = 1/[1 - 24\eta a(q)] \tag{3.69}$$

where $q = QD$. The expression for $a(q)$ is too long to be represented here. It can be found in Ref. 174.

Structure factor of fractal

Present chapter is based on ref. [177].

Before we have shown that at large q values the intensity of the scattering $I(q)$ varies as $q^{-\alpha_P}$, where α_P is the power-law exponent and depends on the dimensionality and morphology of the scattering object. The mass fractal structure is characterized by a value of exponent of $2 < \alpha_P < 3$. An important characteristic of the fractal is the fractal dimension parameter, d_f, which determines the density of packing inside the fractal aggregate. Thus, the particle number density is given by:

$$N(r) = \left(\frac{r}{r_0} \right)^{d_f} \tag{3.70}$$

where r is the radius of the fractal object and r_0 is the radius of its building block. d_f takes values between $2 < d_f < 3$ and equivalent to the Porod exponent. The value of d_f close to 3 manifests the cluster is very dense, whereas lower values suggest a loosely connected network inside the fractal.

The structure factor for mass-fractal aggregates with finite size is given by:

$$S_{FR}(q) = 1 + \frac{1}{(qR_{mic})^{d_f}} \frac{d_f \Gamma(d_f - 1)}{\left[1 + \frac{1}{(qR_{cl})^2} \right]^{(d_f - 1)/2}} \sin\left[(d_f - 1) \tan^{-1}(qR_{cl}) \right] \tag{3.71}$$

where R_{mic} is the radius of a micelle or a building block, R_{cl} is the cluster radius.

Ornstein-Zernike structure factor

With the aim to describe the concentration fluctuations arising from the looping chains in the shell or fuzzy interface of particles or bridging chains inside the network, an Ornstein-Zernike model was used:[178]

$$S_{OZ}(q) = \frac{I_{OZ}}{1 + \xi^2 q^2} \tag{3.72}$$

where I_{OZ} is the amplitude of the contribution and ξ is the correlation length of density fluctuations. Assuming the spatial inhomogeneities in cross-linker density within the particles and inside the network, ξ denotes the average mesh size between the interconnected chains.

3.3. Dynamic light scattering

Present chapter is based on refs. [179-182].

Dynamic light scattering (DLS) is one of the most powerful techniques, which allows to determine the size of particles. It is based on the illumination the sample by the coherent light from a source (laser, fig. 3.12), which causes the oscillating polarization of electrons in the molecules, which act as a secondary source of light and scatter the light.[181] The scattered light is collected by a detector, and afterwards transmitted to a correlator and a computer.

The technique is based on comparing the fluctuation intensity with time. Continuous Brownian motion of particles due to their thermal motion or collision with solvent molecules, causes the fluctuations in intensity of the scattered light. The rate of these is strongly related to the rate of diffusion of the particles, and, hence, their size and interactions between them. In case of cross-linked gels the DLS can give the information on the time scale of the relaxation processes.

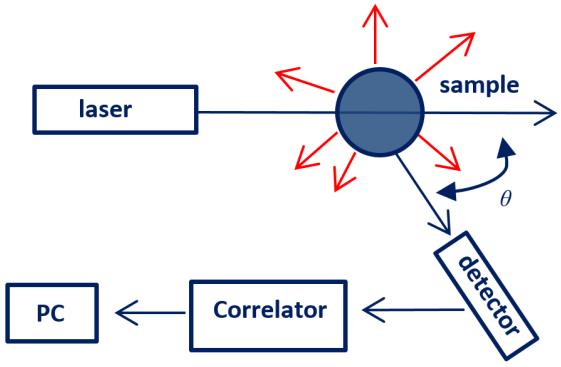

Fig. 3.12: Schematic representation of dynamic light scattering (DLS) setup.

3.3.1. Principle of dynamic light scattering

The valuable information is obtained by constructing the autocorrelation function, $G_2(\tau)$, which describes the time fluctuation of the scattered light intensity by comparing the intensity at initial time *t*, $I(t)$ to the intensity after a delay time τ, $I(t+\tau)$, and so on:

$$G_2(\tau) = \frac{\langle I(t) \cdot I(t+\tau) \rangle}{\langle I(t) \rangle^2} \quad . \tag{3.73}$$

At short delay times, the change in a particle position is very small, which is accompanied by a very small change in scattering intensity. So at this stage the scattering intensity is strongly correlated with the intensity at initial time *t*. At longer delay times, the particles have moved to

a higher extent and the correlation between the intensities at initial time *t* and after longer decay time τ is lower. Thus, autocorrelation function decays until it reaches zero, when the correlation between the particle initial and final position is lost. In absence of any defined interparticle interactions, the particle position is defined mainly by a Brownian motion, and so the autocorrelation curve is related to the particle diffusion coefficient.

The intensity fluctuations are correlated with fluctuations in electric field. Thus, $G_2(\tau)$ can be translated to the correlation function of the scattered electric field, $G_1(\tau)$ as:[182]

$$G_2(\tau) = 1 + \beta \left| G_1(\tau) \right|^2 \tag{3.74}$$

with β being a coherence factor, defined by a geometry of the instrument.

For the sample with monodisperse particles:

$$\left| G_1(\tau) \right| = \mathrm{e}^{-\Gamma \tau} \tag{3.75}$$

where Γ is the relaxation rate, $\Gamma = 1/\tau_r$ with τ_r being the relaxation time:

$$\tau_r = \frac{1}{Dq^2} \tag{3.76}$$

where *D* is the translational diffusion coefficient, and *q* the scattering wave vector:

$$q = \frac{4\pi n_0}{\lambda_0} \sin\frac{\theta}{2} \tag{3.77}$$

where n_0, λ_0 and θ are the refractive index of the solvent, the vacuum wavelength of the incident light and the scattering angle, respectively. For non-interacting particles the hydrodynamic radius, R_H, is related to a diffusion coefficient through Stokes-Einstein equation:

$$D = \frac{k_B T}{6\pi \eta_0 R_H} \tag{3.78}$$

where k_B, T and η_0 are the Boltzmann's constant, the temperature and the solvent viscosity, respectively.

In case of bimodal particle size distribution or two different dynamical processes present in the system, the autocorrelation function can be described by:

$$G_2(\tau) = 1 + C\left[A\exp(-(\tau/\tau_{r1})^{\beta_1} + B\exp(-(\tau/\tau_{r2})^{\beta_2} \right]^2 \tag{3.79}$$

where *A* and B (B=1-*A*) are the relative amplitudes, τ_{r1} and τ_{r2} the relaxation times and β_1 and β_2 the stretching exponents of the two decays, and *C* a correction factor.

The measured autocorrelation functions $G_2(\tau)$ were treated using the algorithm REPES, incorporated in the GENDIST program.[183,184]

3.3.2. Dynamic light scattering from non-ergodic systems

Present chapter is based on refs. [185,186].

In the previous section we have considered ergodic systems where the scattering particles are mobile. It means that on the time scale of experiment all possible spatial configurations are achieved, so the time averaged function is equal to ensemble averaged. In contrary in non-ergodic systems, like cross-linked networks, gels, there are constrained internal inhomogeneities, which exhibit only limited fluctuations around their fixed position. In these systems the scattered light has two origins. The first one is related to the concentration fluctuations, arising from the network, and it carries valuable information. The second contribution is related to the macroscopic inhomogeneities. The movement of the latter ones is restricted, which leads to the time averaged function being not equivalent to the ensemble averaged function. In order to obtain an ensemble averaged function we used a rotational cell.

3.3.3. Instrument

The rotational DLS measurements were performed at the instrument ALV/CGS-8F goniometer (ALV, Langen, Germany), which is shown in figure 3.13a. A monochromatic light from the source, here the Helium–Neon laser with a wavelength of λ = 632.8 nm, shines on the sample. It is possible to reduce the intensity of the incident beam by means of a liquid crystal attenuator (Att) (fig. 3.13a). Afterwards the beam is focused onto the sample. The sample is placed in a cylindrical quartz glass 10 mm diameter cuvette (C), which is positioned in the bath cell. To minimize reflections from the interface between the cuvette and surrounding area, the cell is filled with toluene. The temperature of cell is controlled by a thermostat. The motor-driven goniometer (G) with inserted photomultiplier detector (PMT) allows the wide range of scattering angle (from 20° to 150°), at which the scattered light is collected. Afterwards the signal is transmitted to a fast photon count digital correlator and a computer.

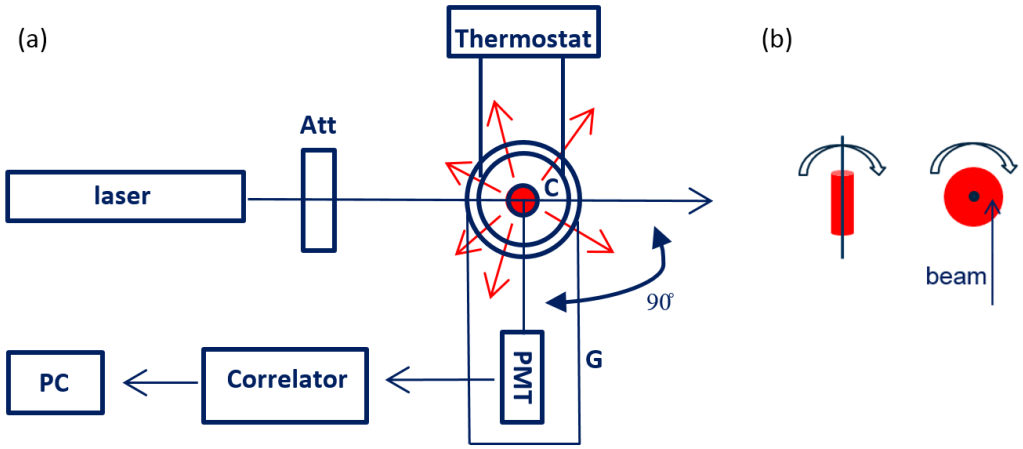

Fig. 3.13: (a) Schematic presentation of ALV-laser experimental setup; (b) In rotational DLS, the cell with sample (C in (a)) constantly rotates in the incident beam during the measurements.

4. Physical hydrogels from triblock polyampholytes and polyelectrolytes

In the present chapter we aim to study the conformational properties of hydrogels from triblock polyelectrolytes P*t*BA-*b*-P2VP-*b*-P*t*BA (P*t*BA and P2VP are poly(*tert*-butyl acrylate) and poly(2-vinylpyridine)) and the corresponding polyampholytes PAA-*b*-P2VP-*b*-PAA (PAA is poly(acrylic acid)), the latter with nonquaternized or quaternized P2VP blocks. Previous rheological studies on these systems have indicated rich pH-dependent behavior. Identification of the underlying changes in the structure can help to understand association mechanisms, resulting in peculiar mechanical properties.

In the first part we will focus on the effect of charge asymmetry on self-organization behavior of the quaternized polyampholyte PAA-*b*-QP2VP-*b*-PAA at different pH values (3.0, 5.0 and 7.0). In this polymer, the QP2VP block is strongly charged, independently of pH, whereas the PAA block exhibits pH-dependent deprotonation. Solution behavior of the polymer is defined by the interplay between the electrostatic repulsive and/or attractive interactions between the charged moieties and the associative hydrophobic interactions of the non-ionized units. By varying pH, it is possible to change the charge ratio $[2VPR^+]/[AA^-]$, and, hence, to influence the strength of both: attractive and repulsive electrostatic interactions, which would eventually affect the resulting gelation ability of the system.

Further, we will focus on the influence of the structure of block copolymers, defined by nature of their building blocks on the polymer associative character and structure of formed hydrogels, which govern their macroscopic behavior. Two systems will be studied here: the nonquaternized polyampholyte PAA-*b*-P2VP-*b*-PAA and the telechelic polyelectrolyte P*t*BA-*b*-P2VP-*b*-P*t*BA. SANS studies will be carried out at pH 3.0, where the maximum viscosity for these systems was previously detected. Lower degree of ionization of the P2VP blocks in PAA-*b*-P2VP-*b*-PAA and P*t*BA-*b*-P2VP-*b*-P*t*BA in comparison to the one in PAA-*b*-QP2VP-*b*-PAA is expected to decrease the influence of electrostatic interactions on the polymer behavior, simultaneously increasing the hydrophobicity in the system due to a high amount of non-ionized units, which would inevitably lead to the differences in structural and rheological behavior of these systems.

4.1. System

For the present study the following systems were chosen: a triblock polyelectrolyte P*t*BA$_{163}$-*b*-P2VP$_{1397}$-*b*-P*t*BA$_{163}$ (P*t*BA and P2VP are poly(*tert*-butyl acrylate) and poly(2-vinylpyridine), Table 4.1) and two successive polyampholyte systems: PAA$_{163}$-*b*-P2VP$_{1397}$-*b*-PAA$_{163}$ and PAA$_{163}$-*b*-QP2VP$_{1397}$-*b*-PAA$_{163}$ (PAA and QP2VP are poly(acrylic acid) and quaternized poly(2-vinylpyridine)). P2VP is a weak polybase and exhibits pH-dependent protonation at low pH values, below pH ca. 5. PAA is a weak polyacid and is deprotonated at all pH values above 4.2.[187] The QP2VP block is a chemically modified, quaternized counterpart of P2VP, which means that almost each 2VP unit on QP2VP is permanently charged, so that the degree of ionization of the QP2VP blocks reaches 97%.[188] P*t*BA is neutral and hydrophobic.

Table 4.1: Molecular characteristics of the polymers.

Polymer	M_w (g/mol)	M_w/M_n	P2VP (wt %)
P2VP	147000	1.29	
P*t*BA-*b*-P2VP-*b*-P*t*BA	192000	1.31	76.6
PAA-*b*-P2VP-*b*-PAA	173000		85.0

All polymer hydrogels were prepared by Dr. Maria T. Popescu (Laboratory of Macromolecular Engineering, Department of Chemical Engineering, University of Patras, Patras, Greece). The polymers were synthesized by Dr. Nikoletta Stavrouli (Department of Chemical Engineering, University of Patras, Patras, Greece). The details of the synthesis and the sample preparation can be found elsewhere.[122,189-190]

The structures of samples were investigated at concentration of 4 wt% in D_2O, which is above the percolation threshold. This makes the studies of present systems more valuable for their further potential applications as injectable hydrogels.

4.2. Instrumental set-up

Rheometry. Measurements were performed on a stress controlled Rheometric Scientific SR 200 rheometer in either a cone-and-plate geometry (diameter 25 mm, cone angle α = 5.7°, truncation 56 μm) or a Couette geometry (gap 1.1 mm) for the less viscous solutions. After each

sample loading, a delay of 5 minutes was applied before each measurement, in order to erase the mechanical history. The temperature was fixed at 25 ± 0.1 °C.

Small-angle neutron scattering (SANS). Measurements of the quaternized polyampholyte at pD 7.0, 5.0 and 3.0 were carried out at the instrument D22 at the Institut Laue-Langevin (ILL) in Grenoble, France. The neutron wavelength was chosen at λ = 0.8 nm with a spread $\Delta\lambda/\lambda$ =10%. The sample-detector distances (SDDs) were chosen at 3.98 m and 13.98 m in order to cover a q range from 0.028 to 2.0 nm^{-1}. The exposure times were 10 min and 15 min at SDD = 3.98 m and 13.98 m, respectively. All measurements were carried out at room temperature. The sample having pD 3.0, was mounted in a 0.5 mm quartz cuvette (Hellma), whereas the samples having pD 5.0 and 7.0, were mounted in a 1 mm quartz cuvette (Hellma). In all cases the renormalization to absolute units was performed through known procedures using the scattering from H_2O. The electronic background was detected while shielding incoming neutron beam by boron carbide B_4C. The resulting data were corrected for absorption and background scattering by subtraction of the scattering of D_2O and the empty cell from the sample scattering. In all cases transmissions were taken into account. The two-dimensional images were azimuthally averaged. The software LAMP from ILL was used for the raw data treatment.

Measurements of the nonquaternized polyampholyte and polyelectrolyte at pD 3.0 were carried out at the instrument KWS-2 at the JCNS outstation at MLZ in Garching, Germany. The neutron wavelength was chosen at λ = 0.45 nm with a spread $\Delta\lambda/\lambda$ = 20%. Using sample-detector distances (SDDs) of 3.64 m and 19.64 m, a range of momentum transfers q = 0.03 to 2 nm^{-1} was covered. The samples were mounted in 0.5 mm quartz cuvettes (Hellma) and were measured at room temperature. The exposure times were 10 min and 15 min at SDD = 3.64 m and 19.64 m, respectively. The scattering of boron carbide was used for correcting the intensities for the dark current. Poly(methyl methacrylate) was used to measure the detector sensitivity and for calibration of the intensity. The scattering of D_2O and the empty cell were subtracted from the sample scattering, taking the transmissions into account. The two-dimensional images were azimuthally averaged. All data reductions were performed with the software QtiKWS provided by JCNS.

4.3. Triblock polyampholyte: Effect of charge asymmetry

The present chapter is based on ref. [191].

4.3.1. System

For the present study of the influence of charge asymmetry on the polymer association behavior, the quaternized polyampholyte PAA_{163}-*b*-$QP2VP_{1397}$-*b*-PAA_{163} was chosen. The degree of ionization of the PAA blocks, α, is pH-dependent (pD-dependent in D_2O) (fig. 4.1a).[191] In presence of the QP2VP, a strong polybase, the pK_α of the PAA blocks is shifted to 3.5 (for PAA homopolymer it is $pK_\alpha = 4.2$, Ref. 187). At the same time, the QP2VP block is strongly charged, independently of pH (pD in D_2O). Thus, by varying pH/pD, it is possible to change the ratio of negatively charged AA units to positively charged Q2VP units, and, hence, to influence the charge asymmetry in the system. The choice of the present system was motivated by two main reasons. Firstly, the fact that QP2VP block is constantly charged and, hence, water soluble in the entire pH range, prevents the polymer precipitation at any pH and makes the studies of the system possible in the entire pH range. In comparison, in the nonquaternized polyampholyte system, the precipitation region was previously detected in the vicinity to the isoelectric point, *i.e.* when the numbers of oppositely charged AA and 2VP units become equal, leading to their mutual neutralization (fig. 4.1b, dashed region).[191]

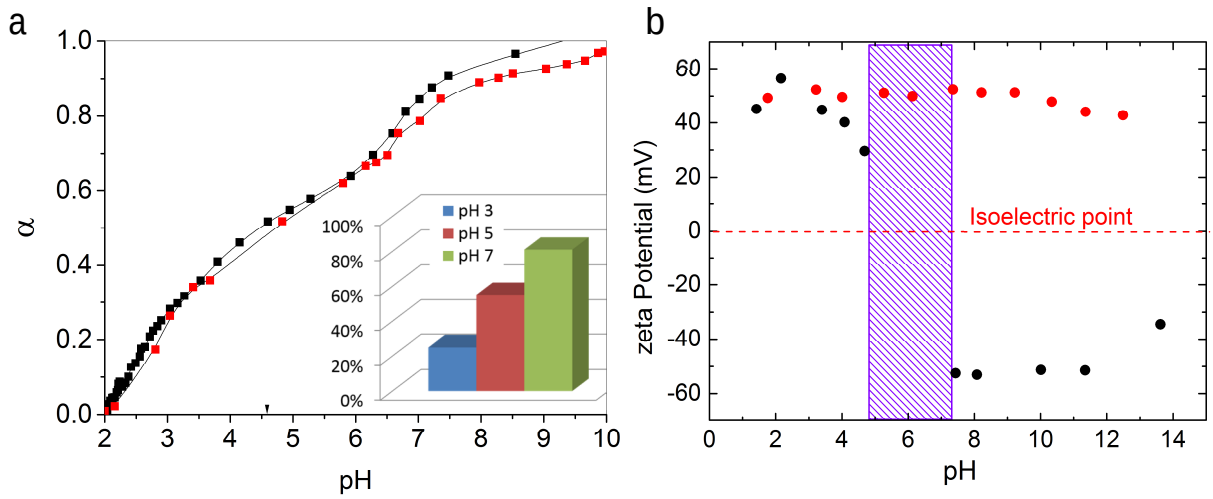

Fig. 4.1: (a) Degree of ionization of the PAA blocks as a function of pH in solutions of PAA_{163}-*b*-$QP2VP_{1397}$-*b*-PAA_{163}: increasing pH by titration with NaOH (red symbols), decreasing pH by titration with HCl (black symbols). In the inset, degrees of ionization of PAA at pH values of interest are shown; (b) Zeta-potential as a function of pH for PAA_{163}-*b*-$P2VP_{1397}$-*b*-PAA_{163} (black circles) and for PAA_{163}-*b*-$QP2VP_{1397}$-*b*-PAA_{163} (red circles). The dashed region indicates the isoelectric point region (4.8 < pH < 6.8) for PAA_{163}-*b*-$P2VP_{1397}$-*b*-PAA_{163}. Taken from Ref. 191.

The second argument towards studies of the quaternized polyampholyte is the enhanced control over the net charge of polymer. Thus, pronounced block length difference, *i.e.* the prevailing number of positively charged 2VP units over negatively charged AA units is at the origin of high positive *z*-potential at all pH values (fig. 4.1b). In comparison, in the nonquaternized polyampholyte the degree of ionization of both PAA and P2VP blocks is pH-dependent and varies simultaneously with increasing pH. From figure 4.1b it can be seen that the *z*-potential changes its sign from positive at low pH, where protonated P2VP segments prevail, to negative at high pH, where 2VP units lose their charge, whereas deprotonated ionized PAA segments become dominating. This diverse behavior hampers the understanding of the association behavior of the nonquaternized polyampholyte in a wide range of pH. Another complication arises from the fact that the hydrophobic associations of non-ionized blocks and the interpolyelectrolyte complexation between oppositely charged blocks in the nonquaternized system become indistinguishable.

4.3.2. Rheological studies

The present chapter is based on ref. [191].

Measurements were carried out by Dr. Maria T. Popescu (Laboratory of Macromolecular Engineering, Department of Chemical Engineering, University of Patras, Patras, Greece).

The gelation ability of the PAA_{163}-*b*-$QP2VP_{1397}$-*b*-PAA_{163} triblock polyampholyte was studied in aqueous solutions at 4 wt% in the range of pH from 2.5 to 7.[191] In the low pH region, *i.e.* at pH 3.0 and 4.0, the polyampholyte forms transparent free-standing gels, which turn into free flowing opaque solutions at higher pH values (fig. 4.2a). Steady state shear viscosity measurements on obtained solutions/gels were carried out, and the viscosity versus shear stress profiles are presented in figure 4.2b. For viscosity profiles below pH 6, increasing the shear stress, a low-shear Newtonian region was indicated, followed by a sharp viscosity decrease.

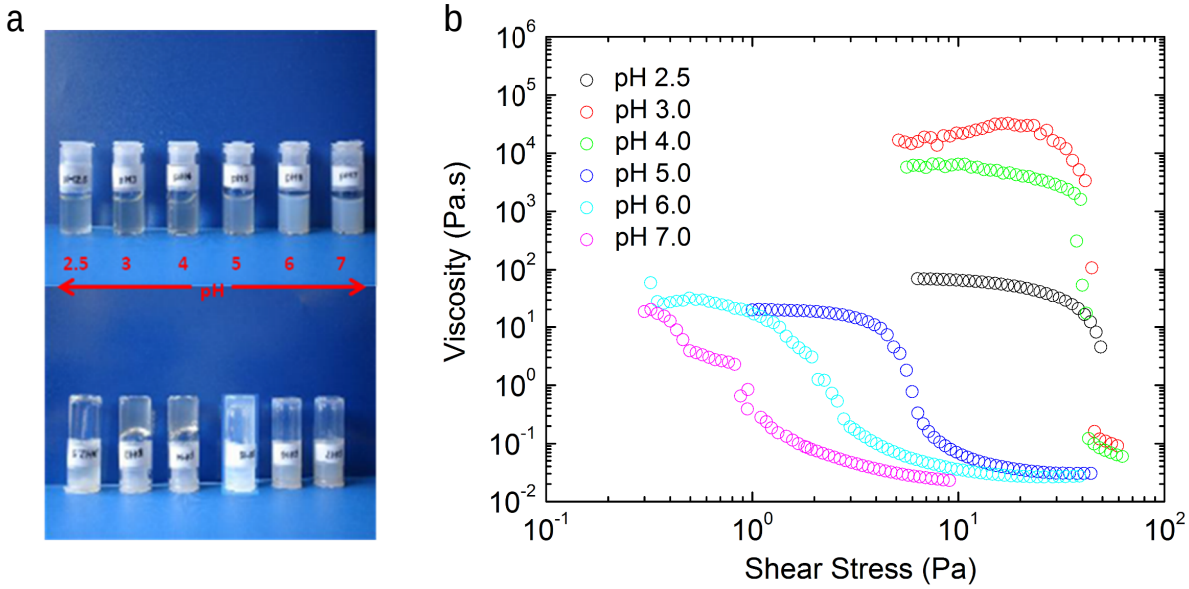

Fig. 4.2: (a) Photos demonstrating free-standing gels at pH 3 and 4 and solutions at other pH values; (b) Apparent viscosity as a function of shear stress of aqueous solutions of PAA_{163}-*b*-$QP2VP_{1397}$-*b*-PAA_{163} at 4 wt% at different pH values. Modified from Ref. 191.

At pH 7, the viscosity is shown to be a non-Newtonian with nearly continuous shear-thinning behavior. The solution maximum viscosity (of the order of several 10^4 Pa.s) was detected at pH 3, manifesting the formation of a strong free-standing hydrogel. The zero shear viscosity, obtained from figure 4.2b for different pH values is presented in figure 4.3.[191] For the sake of comparison, the zero shear viscosity of the precursor system PAA_{163}-*b*-$P2VP_{1397}$-*b*-PAA_{163}

at 1.2 wt% is presented in the inset. Both systems were shown to have similar viscosity profile below pH ~ 4.5, where the nonquaternized polyampholyte precipitates. The maximum viscosity for both systems was detected close to pH 3, implying the electrostatic interactions is the main driving force for the network formation since all Q2VP units in the quaternized system are ionized, excluding or minimizing the contribution from hydrophobic associations of the non-ionized segments, that may occur in the nonquaternized system.

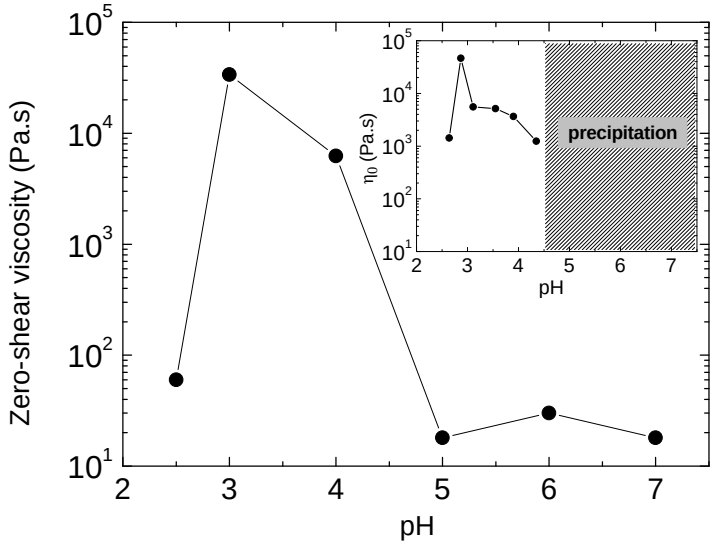

Fig. 4.3: Zero-shear viscosity, η_o, as a function of pH of 4 wt% PAA_{163}-*b*-$QP2VP_{1397}$-*b*-PAA_{163} aqueous solutions and its precursor PAA_{163}-*b*-$P2VP_{1397}$-*b*-PAA_{163} at c = 1.2 wt% (inset). Modified from Ref. 191.

From figure 4.3 it can be seen that the viscosity drops significantly at pH 2.5 and 5, manifesting that the pH defined charge asymmetry (ratio $[AA^-]/[2VPR^+]$) on the polyampholyte strongly influences its resulting gelation ability. Further studies on the viscoelastic behavior revealed two different viscoelastic responses, depending on pH (fig. 4.4). From figure 4.4 it can be seen that at pH 3 and 4, $G' > G''$ in the whole frequency range. The long relaxation times − higher than 500 s (the G', G'' crossover is not visible) were correlated with the appearance of free-supporting hydrogels in this pH region (fig. 4.2). The change of the viscoelastic behavior from gel-like to viscoelastic was detected at pH 5. Both moduli were found to be lower than those at pH 3 and 4, whereas the terminal relaxation time decreases to 50 s (the G', G'' crossover occurs at f = 0.02 Hz).[191] The authors attribute the change in the viscoelastic behavior to the gel-to-sol transition, detected earlier (fig. 4.2a, 4.3).

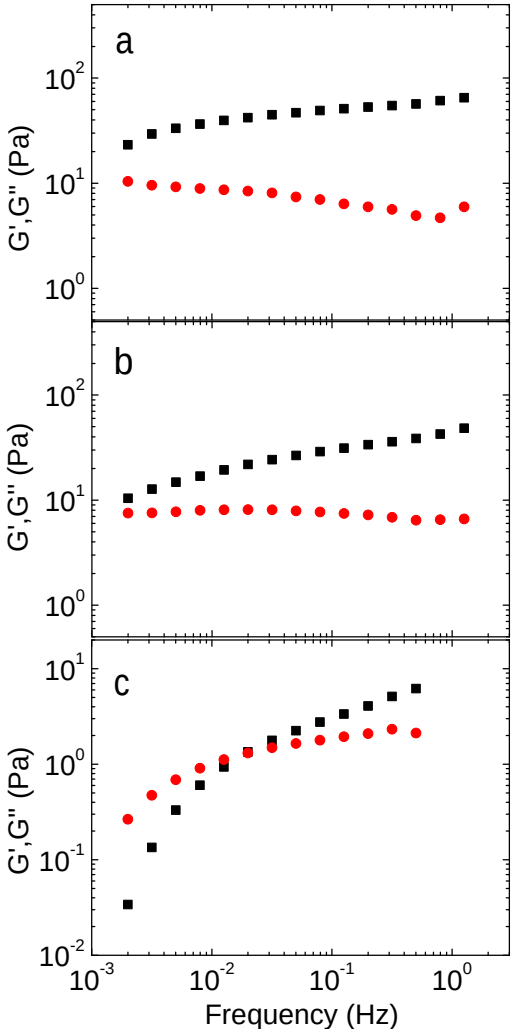

Fig. 4.4: Frequency dependence of dynamic moduli, G' (black symbols) and G'' (red symbols) of 4 wt% PAA_{163}-*b*-$QP2VP_{1397}$-*b*-PAA_{163} aqueous solutions at pH 3 (a), pH 4 (b), and pH 5 (c). Taken from Ref. 191.

4.3.3. Structural investigation

The present chapter is based on ref. [191].

In order to get insight into the association mechanisms and the corresponding changes in the internal structure, being at the origin of the detected rheological response upon pH variation, the small-angle neutron scattering (SANS) on the present system was performed in D_2O at 4 wt% at three different pD values: 7.0, 5.0 and 3.0, where the strongest variations in mechanical response were detected (fig. 4.3). Figure 4.5a shows the degrees of ionization of the QP2VP, P2VP and PAA blocks at pH (pD in D_2O) values of interest. In figure 4.5b, the schematic representation of the quaternized polyampholyte structures upon pH/pD variation is depicted.

a

Degree of ionization	pH 3.0	pH 5.0	pH 7.0
QP2VP	QP2VP fully charged		
P2VP	40%		
PAA	25%	55%	80%

b

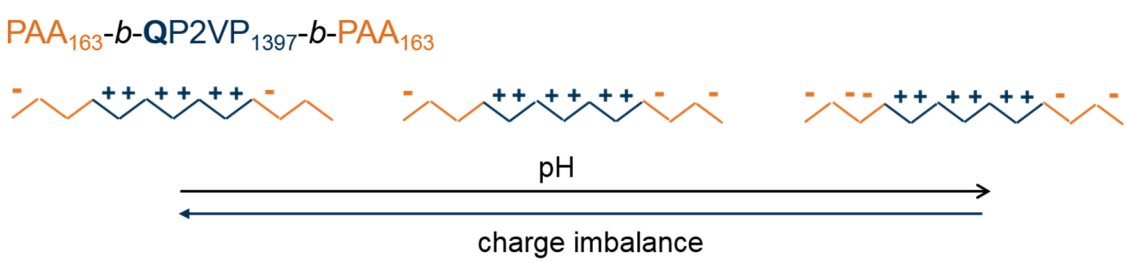

Fig. 4.5: (a) Degrees of ionization of different blocks at three chosen pH values; (b) Schematic representation of structures of PAA_{163}-*b*-$QP2VP_{1397}$-*b*-PAA_{163} with increasing pH.

Figure 4.6 shows the compiled SANS curves from the quaternized polyampholyte at pD 7.0, 5.0 and 3.0, increasing the charge imbalance. All curves have different shapes, disclosing the different morphology in each case. The curve at pD 7.0 shows a decay with a shallow minimum at $q \sim 0.1$ nm^{-1}, whereas the curve at pD 5.0 features a shallow minimum at $q \sim 0.2$ nm^{-1}. The curve at pD 3.0 significantly differs from those at pD 7.0 and 5.0 by the presence of a maximum at $q \sim 0.08$ nm^{-1}, followed by a shoulder at $q \sim 0.2$ nm^{-1} together with a broad decay at $q > 0.4$ nm^{-1}.

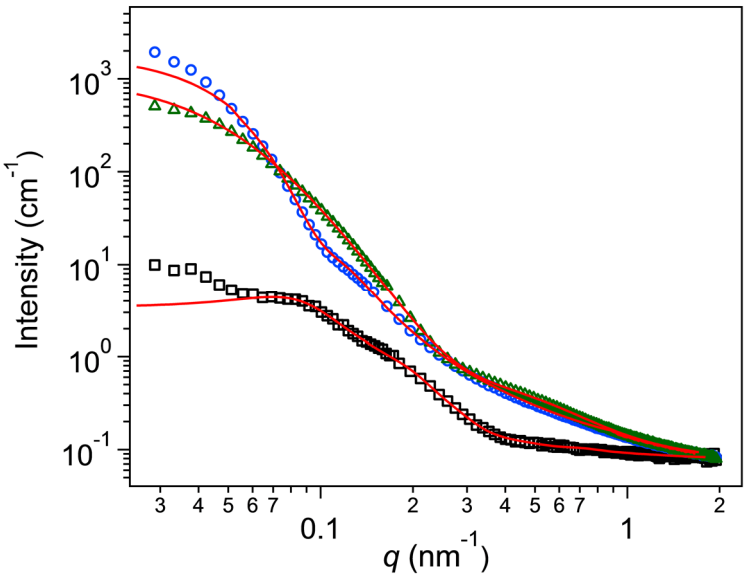

Fig. 4.6: SANS curves of 4 wt% PAA_{163}-*b*-$QP2VP_{1397}$-*b*-PAA_{163} aqueous solutions at 26 ºC at pD 7.0 (blue circles), pD 5.0 (green triangles) and pD 3.0 (black squares). The solid lines represent the model fits, see text. Taken from Ref. 191.

Previously, in chapter 2 we have shown that, depending on the charge imbalance on the polyampholyte chain, it adopts different chain conformations. Strongly non-balanced chains (with a non zero net charge) are located in the polyelectrolyte regime, which means they are stretched and may form network connections. Charge balanced chains with a net charge zero collapse due to the fluctuation-induced attraction of chain segments with opposite charges. In nearly charge balanced polyampholyte systems, the final polymer conformation is defined by the interplay between the electrostatic attraction of opposite charges and repulsion between excess charges of one sign. Therefore, we expect different pH-dependent morphologies with increasing charge asymmetry.

At pD 7.0 the net charge imbalance is minimum. The degree of ionization of the PAA blocks, α, is 80% (fig. 4.1a). In presence of high number of both Q2VP and AA ionized units, extended attractive electrostatic interactions take place. The scattering curve was successfully fitted by Eq. 4.1, describing the scattering from polydisperse spheres with a Gaussian size distribution. The contribution at high q (> 0.4 nm^{-1}) was related to the scattering from concentration fluctuations of the network of complexed chains and accounted by the Ornstein-Zernike term, $S_{OZ}(q)$ (Eq. 3.72):

$$I(q) = P_{sph}(q) + S_{OZ}(q) + I_{bkg}\,. \qquad (4.1)$$

$\Delta\rho^2 = (\rho_{sph} - \rho_s)^2$ in $P_{sph}(q)$ (Eq. 3.43) is the contrast factor and I_{bkg} the incoherent background intensity. ρ_{sph} and ρ_s are the mean scattering length densities (SLD) of the sphere and the solvent, respectively. The SLDs of PAA and QP2VP were calculated at 1.66×10^{-4} nm^{-2} and 1.26×10^{-4} nm^{-2}. The SLD of D_2O was taken at $\rho_s = 6.36 \times 10^{-4}$ nm^{-2}. The contributions to the model fit are presented in dashed lines in figure 4.7a.

We suppose that the deduced spherical aggregates represent microgels from complexed positively charged QP2VP segments on the middle blocks and negatively charged PAA segments on the outer blocks. These aggregates are not densely packed, instead they contain a certain amount of solvent, *i.e.* about 14%. The value was derived from the difference between experimental SLD value of the sphere (SLD_{exp} is found at 2.0×10^{-4} nm^{-2}) and calculated one for a 1:1 mixture of PAA and QP2VP. Absence of a structure factor suggests no correlation between these microgels. Presumably, excess positive charges from $P2VPCH_3^+$ on each microgel induces repulsion between them, keeping them apart from each other and stabilizing in this way the solution. These findings explain the origin of low viscosity of the sample at this pH, previously detected by rheology.

By fitting Eq. 4.1, we derived the characteristic dimensions in the system. The average microgel radius is deduced at $R_{sph} = 37.1 \pm 1.9$ nm with a polydispersity $p = 0.27 \pm 0.08$. From fitting of the Ornstein-Zernike term in Eq. 4.1, the correlation length is determined at $\xi = 2.6 \pm 0.6$ nm and is attributed to an average distance between complexed PAA and QP2VP chains in the network within the microgel. We suppose that the concentration fluctuations arise at small length scales within the aggregates due to non-compact conformation of complexed chains as a result of fast electrostatically driven aggregation process, which may also lead to the imbalanced ratio of oppositely charged chains inside the microgel.

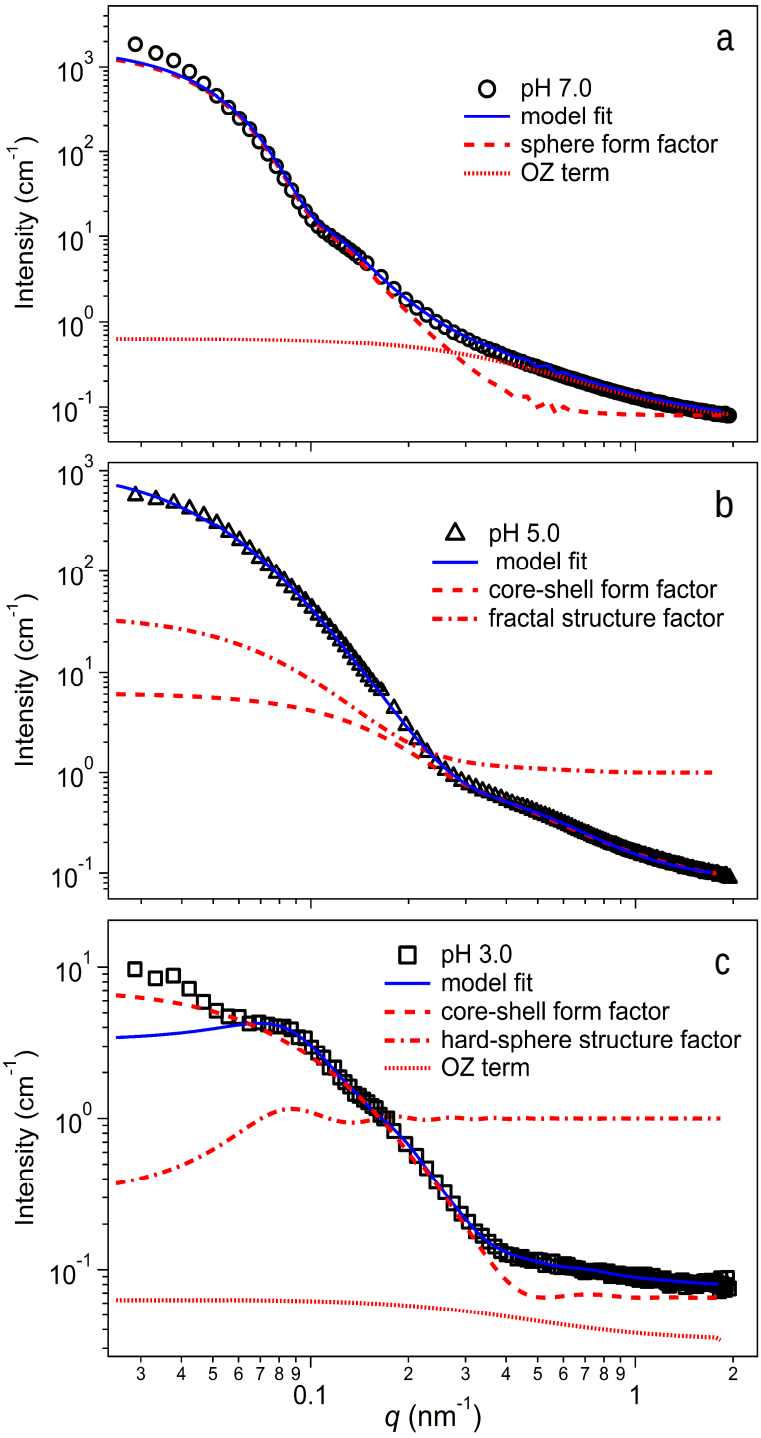

Fig. 4.7: SANS curves of 4 wt% PAA_{163}-*b*-$QP2VP_{1397}$-*b*-PAA_{163} aqueous solutions from Fig. 4.6: at pD 7.0 (a), pD 5.0 (b) and pD 3.0 (c). The symbols represent the experimental data, and the solid lines the overall model fits. The non-continuous lines represent the contributions to the model. Taken from Ref. 191.

At pD 5 the charge imbalance is higher than at pD 7 due to the lower fraction of negatively charged AA units on the outer blocks (degree of ionization of PAA is 55%, fig. 4.1a). The SANS curve of a solution of PAA_{163}-*b*-$QP2VP_{1397}$-*b*-PAA_{163} at pD 5.0 is depicted in figure 4.7b. At low q-values ($q < 0.2$ nm^{-1}), the curve features a bend, followed by a shallow minimum at $q \sim 0.2$ nm^{-1} together with a broad maximum at higher q (~ 0.5 nm^{-1}). The scattering curve was successfully fitted with the model, describing the scattering from fractal aggregates of finite size, formed by spherical core-shell micelles:

$$I(q) = P_{mic}(q)S_{FR}(q) + I_{bkg}\,. \tag{4.2}$$

From fitting the $P_{mic}(q)$ in Eq. 4.2, the radius of the micellar core is found at $R_c = 3.4 \pm 1.1$ nm with a polydispersity of $p = 0.35 \pm 0.06$. From the difference between the established total micellar radius at $R_{mic} = 4.7 \pm 1.1$ nm and the radius of the micellar core, the shell thickness is estimated at 1.3 ± 0.8 nm. Thus, each micelle is rather small and consists of approximately 1-2 polymer chains. This is a result of the reduced number of ionized AA units, which leads to a lower complexation degree with the corresponding number of oppositely charged Q2VP units, and, hence, smaller micellar dimensions. Moreover, due to the localization of charges on the PAA blocks, the PAA_{163}-*b*-$QP2VP_{1397}$-*b*-PAA_{163} molecule does not "see" other distantly located charges from $P2VPCH_3^+$ on other molecules, instead short-range attractive electrostatic interactions prevail and the molecule prefers to fold together. The non-complexed ionized QP2VP segments on the middle chains form a dense shell around the core and may connect several micelles into a loosely packed matrix of the aggregate. Moreover, due to the repulsive electrostatic forces between equally charged segments on the QP2VP block, it can stretch and bridge different aggregates. The fractal dimension is derived at $d_f = 2.8 \pm 0.2$, which implies relatively compact aggregate. From the deduced aggregate radius $R_{cl} = 17.8 \pm 1.3$ nm, the average number of micelles inside the aggregate is estimated at ~ 50. We explain the transition from big spherical particles at pD 7.0 to fractal-like aggregates upon increase in charge asymmetry at pD 5.0 by tendency of the particle to minimize its surface energy. As a result, it splits into smaller aggregates, carrying lower excess positive surface charge from non-complexed ionized P2VP segments. The fact that aggregates are only loosely connected explains why at times longer than 50 s they can be destroyed by shear forces (fig. 4.4c).

Decreasing the pD of the solution to 3.0, the charge imbalance on the molecule increases further. The degree of ionization of PAA reduces to 25% (fig. 4.1a), which leads to a significantly lower

extent of $P2VPCH_3^+/PAA^-$ complexation, and, respectively, smaller hydrophobic micellar cores in comparison with those at pD 5.0. The scattering curve from pD 3.0 is presented in figure 4.7c. It has more complex shape in comparison to the curves at higher pD values. The shoulder at $q \sim 0.2$ nm^{-1} was ascribed to the form factor, describing the architecture of micelles, whereas the maximum at $q \sim 0.1$ nm^{-1} was attributed to the structure factor, which accounts for the correlation between the micelles. The scattering curve was successfully fitted with the model, describing the scattering from polydisperse spherical core-shell particles, which are correlated into a 3D network:

$$I(q) = P_{mic}(q)S_{HS}(q) + S_{OZ}(q) + I_{bkg} \tag{4.3}$$

where $S_{HS}(q)$ is the Percus-Yevick structure factor (Eq. 3.61). As at pD 7.0, the additional scattering at high q values (> 0.4 nm^{-1}) was accounted by the Ornstein-Zernike term, $S_{OZ}(q)$ (Eq. 3.72). An attempt to model the particle shape with a form factor of polydisperse spheres instead of a form factor of core-shell spheres was not successful. From fitting Eq. 4.3, the radius of the micellar core is found at $R_c = 2.7 \pm 0.9$ nm with a polydispersity of $p = 0.4 \pm 0.2$. The shell thickness is deduced at 12.2 ± 1.6 nm, which is considerably larger than the one at pD 5.0. The nature of these core-shell micelles is analogous to the one at pD 5.0. The counterion release initiates the complexation of oppositely charged chains with the formation of a hydrophobic core. The large fraction of non-associated ionized QP2VP sequences on the middle block is pushed out of the core. Being charged and water-soluble, they stretch in space forming spacious shell and may bridge the neighboring micelles. The fact that QP2VP chains form well defined shell we explain with condensation of counterions, which, being distributed in the shell, partially screen excess positive charge on QP2VP chains and reduce their stretching. Nevertheless, we do not exclude the possibility of finding the shell everywhere around the particles with a continuously decreasing density, so it cannot be distinguished by SANS.

From fitting of the Percus-Yevick structure factor in Eq. 4.3, the hard-sphere radius is derived at $R_{HS} = 30.8 \pm 2.1$ nm. It corresponds to the half distance between bridged micelles. The volume fraction of micelles correlated into the network is found at $\eta_{HS} = 0.21 \pm 0.08$. The characteristic distance between micelles, which is almost twice bigger than the micellar size, is a consequence of the mutual repulsion between micelles due to the high surface positive charge on each one of them, which additionally stabilizes the entire 3D network. From fitting of the Ornstein-

Zernike term in Eq. 4.3, the correlation length is found at ξ = 1.3 ± 0.5 nm. We attribute it to the mesh size in the network of interconnected QP2VP chains around the micelles.

The deduced internal organization of the hydrogel, *i.e.* three-dimensional network from interpolyelectrolyte complexes, bridged by non-complexed ionized QP2VP sequences on the middle blocks, explains the origin of the stiff gel formation at this pH (figs. 4.2, 4.3).

4.4. Triblock polyampholyte: Effect of quaternization

The present chapter is based on ref. [191].

4.4.1. System

In the previous section, we studied the effect of charge asymmetry on the self-organized structure of the quaternized polyampholyte PAA_{163}-*b*-$QP2VP_{1397}$-*b*-PAA_{163}. The choice of the system was driven by the possibility to study its properties in the entire pH range. It becomes possible due to a chemical modification of the middle P2VP block, which allows its high degree of ionization (~ 97%), independently on pH, preventing polymer precipitation. In comparison in the nonquaternized polyampholyte, the degree of ionization of the P2VP block is lower than for its counterpart and is of 40% at pH 3 (fig. 4.5a). It decreases further with increasing pH. This rises the influence of hydrophobicity in the system due to a large amount of non-ionized, and, hence, hydrophobic P2VP units, not involved into the $P2VPH^+/PAA^-$ electrostatic complexation. In addition, the degree of ionization of PAA is lower than 25% since now its pK_α is not shifted as it happens in the quaternized polyampholyte. Previous rheological studies have shown that both quaternized and nonquaternized systems exhibit a maximum gelation in the low pH region (fig. 4.3). In figure 4.8, the zero shear viscosity as a function of concentration for two systems is depicted. It can be seen that for both the viscosity strongly increases, *i.e.* by more than 6 orders of magnitude, in the very narrow concentration range, suggesting the formation of a 3D network. However, in the nonquaternized system, the percolation threshold lies at lower polymer concentration, ca. 0.4 wt%, in comparison to the quaternized system, where C_{gel} is at 1.0 wt% (fig. 4.8).

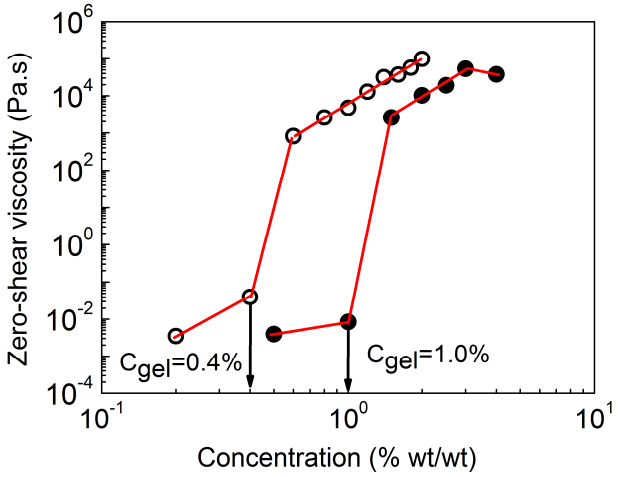

Fig. 4.8: Zero shear viscosity as a function of concentration for PAA_{163}-*b*-$QP2VP_{1397}$-*b*-PAA_{163} at pH 3.0 (closed symbols) and PAA_{163}-*b*-$P2VP_{1397}$-*b*-PAA_{163} at pH 2.9 (open symbols). Both chosen pH values correspond to the maximum viscosity of the corresponding system. Lines guide the eyes and arrows indicate the gelation threshold concentration. Taken from Ref. 191.

Further studies on viscoelastic behavior have shown that the plateau modulus for the nonquaternized system exceeds the one for the quaternized about four times (both systems were studied at 2 wt%), which was linked by authors to a higher bridging degree for the former.[191] In respect that the molecular characteristics, such as composition and relative lengths of the different blocks are the same for two systems, the difference in both: the degrees of ionization of both blocks and the total charge density on polymer were affirmed to be at the origin of different mechanical response in two systems.

4.4.2. Structural investigation

In the present chapter we aim to identify the structural differences of two hydrogels from PAA_{163}-*b*-$QP2VP_{1397}$-*b*-PAA_{163} and PAA_{163}-*b*-$P2VP_{1397}$-*b*-PAA_{163} at pD 3, and to correlate these with the differences in their rheological behavior.

The SANS curves of the quaternized and the nonquaternized polyampholyte solutions are compiled in figure 4.9. Both curves exhibit the same features: the first maximum at low q values (at q = 0.1 nm^{-1} for the quaternized polyampholyte and at q = 0.08 nm^{-1} for the nonquaternized one), associated to the structure factor together with a shoulder at higher q (at q ~ 0.13 nm^{-1}), ascribed to the form factor of micelles. Nevertheless, the curve of the nonquaternized polyampholyte has stronger features, implying the structure is more pronounced.

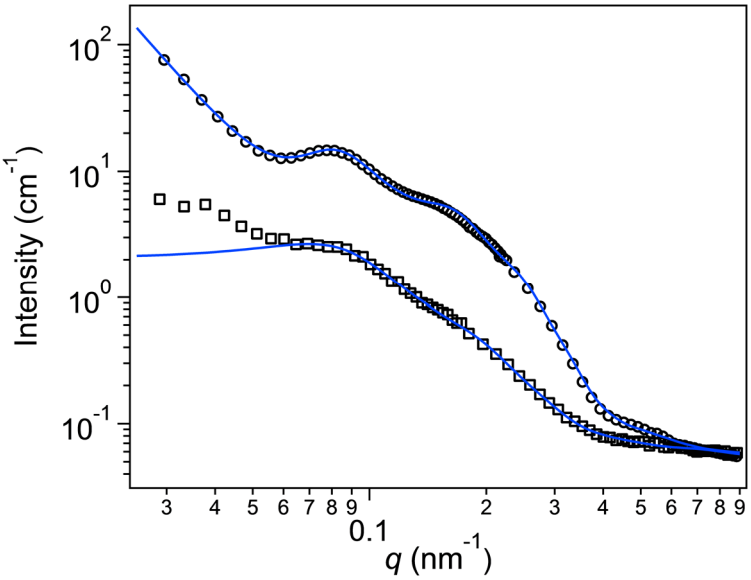

Fig. 4.9: SANS curves of solutions of PAA_{163}-*b*-$QP2VP_{1397}$-*b*-PAA_{163} (squares) and PAA_{163}-*b*-$P2VP_{1397}$-*b*-PAA_{163} (circles) at c = 4 wt% at pD 3.0 at 26 ºC. The solid lines represent the model fits. Taken from Ref. 191.

The curve of the nonquaternized hydrogel was analyzed using Eq. 4.4, which contains the same parameters as Eq. 4.3, but now the modified Porod law, $P_P(q)$ (Eq. 3.41), which accounts for the forward scattering at low q values (< 0.05 nm^{-1}), was included:

$$I(q) = P_{mic}(q)S_{HS}(q) + P_P(q) + S_{OZ}(q) + I_{bkg}\,. \tag{4.4}$$

From fitting the Percus-Yevick structure factor, $S_{HS}(q)$, in Eq. 4.4, the hard-sphere radius for the nonquaternized polyampholyte is found at R_{HS} = 36.1 ± 2.2 nm, thus higher than in the quaternized polyampholyte (R_{HS} = 30.8 ± 2.1 nm), which is consistent with its low percolation threshold (fig. 4.8). Thus, even at low concentrations, the network formation becomes possible due to a high effective length of bridging P2VP chains. The volume fraction of correlated micelles is deduced at η_{HS} = 0.25 ± 0.06 (in comparison with η_{HS} = 0.21 ± 0.08 in the quaternized gel). The micellar radius for the nonquaternized polyampholyte is found at R_{mic} = 10.4 ± 1.5 nm, which is lower than in the quaternized polyampholyte (R_{mic} = 14.9 ± 1.6 nm). In both cases, the micelles consist of the hydrophobic core from complexed PAA and QP2VP/P2VP moieties, surrounded by the shell from non-complexed QP2VP/P2VP segments on the middle chains. From fitting Eq. 4.4, the Porod exponent is deduced at α_P = 3.7, suggesting rather rough surface of the aggregates.

The core radius in the nonquaternized system is found at $R_c = 4.4 \pm 1.1$ nm, thus it is larger than in the quaternized system ($R_c = 2.7 \pm 0.9$ nm). This is due to a larger fraction of non-ionized P2VP units in the nonquaternized polyampholyte, which are concentrated mainly in the hydrophobic core, and so the smaller fraction of hydrophilic $P2VPH^+$ remains in the shell. The bigger core size in the nonquaternized system suggests a higher number of chains, involved in the core formation, and, hence, higher cross-linking functionality and stronger network. In addition to that, we suppose that some of non-charged neighboring P2VP moieties can collapse with a formation of small hydrophobic blobs on the bridging chains, increasing in this way their rigidity. The stronger gel and highly cross-linked network in the nonquaternized system are therefore related to the enhanced hydrophobicity of non-ionized bridging P2VP chains. Being frozen, these contribute to the stiffening of the network. Whereas in the quaternized polyampholyte, the number of charged bridging $P2VPCH_3^+$ chains is high, which causes the repulsion between them, increasing in this way their mobility. This limits the ability of the P2VP chains to preserve high connectivity in the network, resulting in the formation of a weak dynamic gel. These findings explain why the nonquaternized polyampholyte forms stronger gel at lower percolation threshold in comparison to the quaternized polyampholyte.

4.5. Triblock polyelectrolyte

The present chapter is based on ref. [191].

In the previous section we compared the network properties from two polyampholytes with the same triblock architecture and block lengths but with different degree of ionization of the P2VP block. It was shown that the final gel properties are influenced by the rigidity of the bridging elastic chains. The network properties in physical hydrogels are additionally influenced by the stability of physical junctions (cross-links) and the rate of exchange dynamics between them. In polyampholyte systems, these consist of the interpolyelectrolyte complexes from oppositely charged chains. In the present section we aim to study the effect of the different nature of physical cross-links on the structure of hydrogels from the triblock polyelectrolyte P*t*BA-*b*-P2VP-*b*-P*t*BA (P*t*BA is poly(*tert*-butyl acrylate)) with the hydrophobic outer P*t*BA blocks. The system will be studied at pH of the maximum viscosity, *i.e.* 3. In the end the deduced hydrogel nanostructure will be compared to the one from the quaternized polyampholyte PAA-*b*-QP2VP-*b*-PAA at pH 3.

4.5.1. System

Let us recall the charge conditions in two systems. In PAA_{163}-*b*-$QP2VP_{1397}$-*b*-PAA_{163}, the middle P2VP block is a strong polybase (its degree of ionization is of ~ 97%), whereas only 25% of the PAA blocks are charged (Table 4.1, fig. 4.1a). In the telechelic polyelectrolyte P*t*BA_{163}-*b*-$P2VP_{1397}$-*b*-P*t*BA_{163}, the degree of ionization of the P2VP blocks reaches 40%.

The carried earlier rheological studies on similar triblock systems with slightly shorter block lengths have indicated significant differences in their behavior. Thus, the gelation percolation threshold for the telechelic polyelectrolyte was found to be even lower than the one for the nonquaternized polyampholyte, and hence, lower than the one for the quaternized sample.[192] Secondly, the fraction of elastically active chains, and hence elasticity in the polyelectrolyte system was found to be much higher than for the quaternized polyampholyte, leading to the formation of a strong stiff gel in a former case.[192] The authors attribute their findings to the different association mechanism in these two systems, governed by different intra and inter-molecular interactions, defined by the nature of the outer blocks.

4.5.2. Structural investigation

In order to bind observed rheological discrepancies to the morphological characteristics, we compare the SANS data from these two systems (fig. 4.10). Both curves show a structure factor peak at low *q*, which accounts for the distance between the micelles and extent of their correlation, and a shoulder at higher *q*, which was associated with the form factor of micelles. The curve of the polyelectrolyte was described with the same model (Eq. 4.3), used previously for fitting of the curve of the quaternized polyampholyte. The structure factor peak at $q = 0.1$ nm^{-1} in the quaternized system is shifted to $q = 0.06$ nm^{-1} in the telechelic polyelectrolyte, suggesting increase in hard-sphere radius from $R_{HS} = 30.8 \pm 2.1$ nm to $R_{HS} = 55.5 \pm 1.9$ nm in the latter. In the polyampholyte, negatively charged PAA groups interact with ionized QP2VP units on the middle block. As a result, a certain fraction of charges on the middle block is neutralized, accompanied by its simultaneous shrinkage. The resulting length of potentially elastic bridging QP2VP chains, remaining non-complexed with PAA, decreases, which leads to shorter distances between the hydrophobic micelles. Additionally, mobile charged PAA groups can be electrostatically bound to ionized QP2VP sequences on different parts of the middle block, decreasing its effective length not evenly. In comparison, in the polyelectrolyte where the P*t*BA end-blocks are neutral, the non-perturbed charges on bridging P2VP chains strongly repel each other, leading to the stretching of the latter ones and larger intermicellar distances.

The shoulder at $q \sim 0.13$ nm^{-1} in the curve of the telechelic polyelectrolyte was correlated with the form factor of micelles. The core-shell architecture as in the quaternized polyampholyte was deduced. The micellar radius is found at $R_{mic} = 17.8 \pm 1.5$ nm with a core radius of $R_c = 10.8 \pm 1.5$ nm (in comparison with $R_{mic} = 14.9 \pm 1.6$ nm and $R_c = 2.7 \pm 0.9$ nm in the quaternized polyampholyte). In the polyampholyte, the hydrophobic cores arise from electrostatic associations of the oppositely charged chains. A low fraction of ionized PAA units (25%, fig. 4.1a) implies lower degree of complexation with QP2VP, and, as a result, rather small cores. In comparison in the polyelectrolyte, the cores are composed entirely from P*t*BA end-blocks, while P2VP chains form a shell around these cores, preventing their contact with water. The resulting size of the core is determined by the balance between the surface tension of the hydrophobic core and electrostatic repulsive interactions within the P2VP shell. We suppose that “frozen” physical cross-links from P*t*BA blocks in the polyelectrolyte system

make bridging P2VP chains stuck in their junctions, lowering the rate of exchange dynamics between the latter ones and enhancing rigidity of the network. Bigger hydrophobic cores imply higher number of chains, contributing to the network formation, and, hence, higher cross-linking degree in comparison to the quaternized system. These findings explain the origin of a stiff gel formation in case of the telechelic polyelectrolyte.

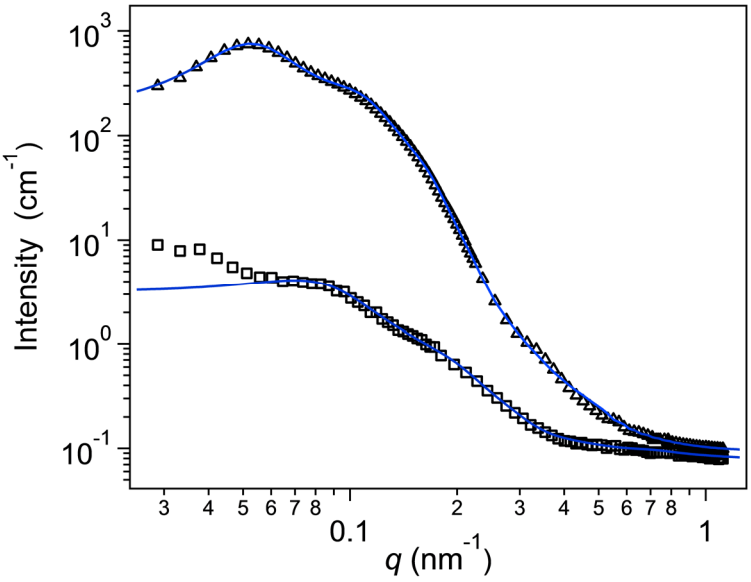

Fig. 4.10: SANS curves of solutions of P*t*BA$_{163}$-*b*-P2VP$_{1397}$-*b*-P*t*BA$_{163}$ (triangles) and PAA$_{163}$-*b*-QP2VP$_{1397}$-*b*-PAA$_{163}$ (squares) at c = 4 wt% at pD 3.0 at 26 ºC. The solid lines represent the model fits. Taken from Ref. 191.

4.6. Conclusions

We have studied the conformational properties of the quaternized polyampholyte in aqueous solutions as a function of charge asymmetry on the polymer. For this reason, SANS measurements of the quaternized polyampholyte were performed at three different pD values, increasing the charge imbalance in the system. The continuous structure evolution was detected decreasing pD from 7.0 to 3.0 (fig. 4.11).

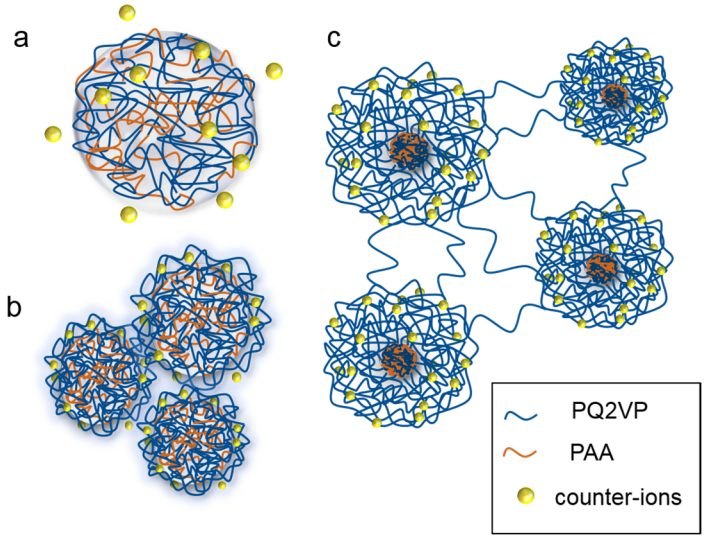

Fig. 4.11: Schematic illustration of self-associated structures in PAA_{163}-*b*-$QP2VP_{1397}$-*b*-PAA_{163} system, deduced from fitting of the SANS curves: dense microgel at pD 7.0 (a), micellar clusters at pD 5.0 (b) and 3D network at pD 3.0 (c). Taken from Ref. 191.

At pD 7.0, extensive and spontaneous electrostatic complexation of the oppositely charged units on polymer results in the formation of uncorrelated dense microgels. At pD 5.0, higher fractional imbalance $[2VPR^+]/[AA^-]$ leads to a lower extent of complexation, and formation of small hydrophobic compartments, surrounded by the corona from non-complexed P2VP chains. The resulting core-shell micelles form fractal clusters. Moving to even higher charge asymmetry, a 3D network from connected core-shell micelles is formed. The micellar core has the same nature as at pD 5.0 with the difference that even fewer oppositely charged chains complex, while the large fraction of non-associated ionized QP2VP chains remain stretched in the shell and can bridge neighboring micelles. High ionization degree on the QP2VP blocks provokes intense *I*-ion condensation, preventing the corona from being completely stretched. Nevertheless, excess positive surface charge on each micelle causes long-ranged electrostatic repulsion between them, affecting the intermicellar distances in the network. Therefore, we demonstrated that the particular rheological behavior of the polyampholyte system is directly related to its internal structure, which, in turn, is determined by the charge imbalance in the system.

The comparison of structures of the quaternized and nonquaternized polyampholytes emphasized the influence of enhanced hydrophobicity of non-ionized P2VP chains in the latter case on the stiffening of the network. Thus, high stability of these “frozen” bridging P2VP

chains is at the origin of the stiff gel formation and lower percolation threshold in the nonquaternized system, whereas in the quaternized polyampholyte the number of charged and hence mobile chains is considerably higher, resulting in a weaker dynamic gel.

In the telechelic polyelectrolyte, 3D network arises from the interplay between the hydrophobic associations of the P*t*BA blocks and the repulsive electrostatic interactions along the middle P2VP blocks. The enhanced stability of "frozen" physical cross-links from P*t*BA blocks and bridging P2VP chains is at the origin of the rigid free-standing gel formation.

Table 1. Parameters, obtained from SANS analysis for three different hydrogels at pD 3.

	PAA-QP2VP-PAA	PAA-P2VP-PAA	P*t*BA-P2VP-P*t*BA
R_c (nm)	2.7 ±0.9	4.4 ± 1.1	10.8 ± 1.5
R_{mic} (nm)	14.9 ±1.6	10.4 ± 1.5	17.8 ± 1.5
R_{HS} (nm)	30.8 ± 2.1	36.1 ± 2.2	55.5 ± 1.9
η_{HS}	0.21 ± 0.08	0.25 ± 0.06	0.19 ± 0.06
ξ (nm)	1.3 ± 0.5	1.9 ± 0.9	3.7 ± 1.0

In the end, we were able to correlate the observed earlier rheological response in these three systems, particularly the percolation threshold dependence, C_{gel}: C_{gel} (telechelic polyelectrolyte) < C_{gel} (nonquaternized polyampholyte) < C_{gel} (quaternized polyampholyte) with the opposite trend in the average distance between correlated micelles: R_{HS} (telechelic polyelectrolyte) > R_{HS} (nonquaternized polyampholyte) > R_{HS} (quaternized polyampholyte). Thus, the higher is the effective length of bridging chains, the lower is the percolation threshold and stronger the gel. A soft gel from the quaternized polyampholyte is due to a large number of equally charged units on the middle QP2VP block, which are not fully screened by counterions. Strong repulsive forces along and between the different QP2VP blocks enhance their mobility, which in turn lowers their ability to bridge the micelles. Free-standing gels from the nonquaternized counterpart and the polyelectrolyte can be explained by enhanced hydrophobicity of the non-ionized bridging P2VP chains and stability of physical cross-links in the network.

5. Hydrogels from triblock polyampholytes – effect of ionic strength

In the previous chapter 4, we studied the influence of charge asymmetry on conformational properties of polyampholyte chains and resulting aggregation mechanisms. In the present chapter we will focus on the second parameter, influencing the gelation ability of the system, namely ionic strength. In charged systems it is expected that, at fixed pH, increase in ionic strength will reduce the charge density of ionizable blocks, influencing in this way an extent of electrostatic interactions and leading to variations in the structure of formed hydrogels and their mechanical stability. For this study two polyampholyte systems were chosen: PAA-*b*-P2VP-*b*-PAA at pD 3 (PAA and P2VP are negatively charged poly(acrylic acid) and positively charged poly(2-vinylpyridine)) and its quaternized counterpart PAA-*b*-QP2VP-*b*-PAA at pD 5 (QP2VP is chemically quaternized P2VP, a strong polybase). The present systems have nearly the same composition as previously studied polyampholyte systems (Chapter 4), but with lower degrees of polymerization of both blocks. These particular pD values were chosen due to the reason that both polyampholytes form gels at these pD. Understanding of the hydrogel behavior upon variation in ionic strength and further possibility to tune its rheological properties may rise an interest to these systems in terms of their potential applicability as injectable hydrogels. Due to the same reason, the changes in micellar network morphology of both systems were studied after addition of NaCl at values in vicinity to physiological value (~ 0.1 M NaCl).

5.1. System

All polymer hydrogels were prepared by Dr. Maria T. Popescu and Sandra Gkermpoura (Laboratory of Macromolecular Engineering, Department of Chemical Engineering, University of Patras, Patras, Greece). The polymers were synthesized by Dr. Nikoletta Stavrouli (Department of Chemical Engineering, University of Patras, Patras, Greece). The details of the synthesis and the sample preparation can be found elsewhere.[122,189,191-192]

Let us review the charge conditions in both systems. In PAA_{109}-*b*-$P2VP_{819}$-*b*-PAA_{109} (M_w = 102000 g/mol; M_w/M_n = 1.23),[193] the degrees of ionization of the PAA and the P2VP blocks are pH-dependent (pD-dependent in D_2O). The pK_α of P2VP is 5.0 and for all pD < pK_α,

the P2VP blocks are ionized (protonated). At pD 3.0, ~ 40% of the 2VP units are protonated. The pK_α of PAA is 4.2,[187] and at low pD of interest, the degree of ionization (deprotonation) of the PAA blocks is of ~ 25%.[191] Thus, at pD 3.0, PAA_{109}-*b*-$P2VP_{819}$-*b*-PAA_{109} can be considered as a weak cationic polyelectrolyte due to the prevailing number of positively charged 2VP units, resulting in a net positive charge on polymer. Nevertheless, high fraction of non-ionized segments on the middle P2VP blocks are responsible for the enhanced hydrophobicity in the nonquaternized polyampholyte. In PAA_{109}-*b*-$QP2VP_{819}$-*b*-PAA_{109} at pD 5.0, the degree of ionization of the PAA blocks increases to 55%.[191] QP2VP is a strong polybase with the degree of ionization of 97%. Thus, the charge density in the quaternized polyampholyte is considerably larger than in the nonquaternized, making electrostatic interactions the prevailing factor, determining the behavior in solution. In the previous chapter, in studies on similar polyampholyte systems, we could deduce the correlation between the strength of formed hydrogels and the stability of elastic bridging chains in the network, defined by their hydrophobicity. Therefore, for the present systems, different in charge density of both PAA and P2VP ionizable blocks, we expect a different scenario of the network structure evolution upon increasing ionic strength.

5.2. Experimental set-up

Rheometry. Measurements were performed on a stress controlled Rheometric Scientific SR 200 rheometer, equipped with a cone-and-plate geometry (diameter 20 mm, cone angle $\alpha = 4°$, truncation 111 μm). After each sample loading, a delay of 10 minutes was applied before each measurement, in order to erase the mechanical history. The temperature was fixed at 25 ± 0.1°C. The linear viscoelastic regime was established by oscillatory strain sweeps at constant frequency of 1 Hz. Creep tests were run by keeping the stress constant within the linear viscoelastic regime.

Small-angle neutron scattering (SANS). Measurements were carried out at the instrument KWS-2 at the JCNS outstation at MLZ in Garching, Germany. The neutron wavelength was chosen at $\lambda = 0.45$ nm with a spread $\Delta\lambda/\lambda = 20\%$. The sample-detector-distances (SDDs) were chosen at 0.99 m, 3.63 m and 19.63 m in order to cover a range of momentum transfer q from $q = 0.022$ to 5.5 nm^{-1}. The samples were mounted in 0.5 mm quartz cuvettes (Hellma). The exposure times were 5 min, 10 min and 20 min at SDD = 0.99 m, 3.63 m and 19.63 m,

respectively. All samples were measured at room temperature. The raw data treatment was performed following the procedures, described in Chapter 4 (section 4.2).

Rotational dynamic light scattering (DLS). Measurements were performed at the instrument ALV/CGS-8F goniometer (ALV, Langen, Germany). The scattering angle was chosen at 90°. The temperature was fixed at 26 ± 0.05 °C. For data acquisition, the software ALV-5000/E was used. The autocorrelation curve was accumulated 100 times. The duration of each run was 5 s.

5.3. Rheological studies

The present chapter is based on ref. [193].

Measurements were carried out by Dr. Maria T. Popescu and Sandra Gkermpoura (Laboratory of Macromolecular Engineering, Department of Chemical Engineering, University of Patras, Patras, Greece).

With the aim to study the influence of ionic strength on the mechanical response of the nonquaternized polyampholyte, rheological measurements were carried out on 3 wt% aqueous solutions of PAA_{109}-*b*-$P2VP_{819}$-*b*-PAA_{109} at pH 3. In figure 5.1a, the elastic, G', and loss modulus, G'', obtained in the linear viscoelastic regime, are plotted as a function of frequency at various NaCl concentrations. Both, G' and G'' were found to be independent of frequency, with G' being higher than G'' in the whole frequency range. The long relaxation times (higher than 100 sec) were correlated by authors with the free-supporting behavior of the hydrogels. Therefore, the hydrogels preserve their elastic response over the entire studied NaCl concentration range.

The zero-shear viscosity was found to steadily decrease with increasing ionic strength (fig. 5.1b). Thus, for the salt-free hydrogel, it is at 2.8×10^5 Pa·s, whereas it decreases to 9.3×10^3 Pa·s at 0.5 M NaCl. The authors correlate the continuous viscosity drop with the decrease of the terminal relaxation time, obtained from creep measurements (fig. 5.2).

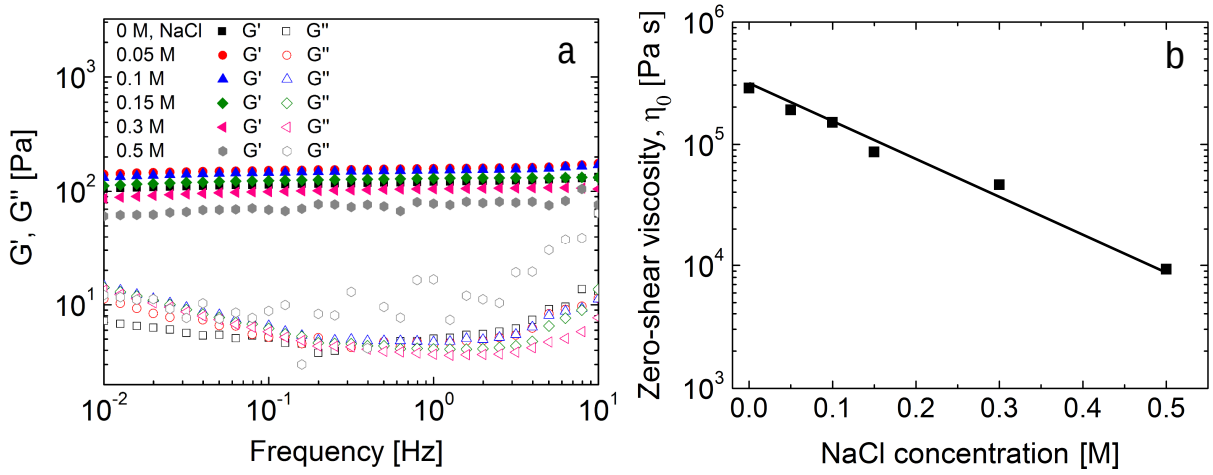

Fig. 5.1: Dynamic moduli, G' (filled symbols) and G'' (open symbols) as a function of frequency at different NaCl concentrations (a) and zero shear viscosity, η_0, as a function of NaCl concentration of 3 wt% PAA_{109}-*b*-$P2VP_{819}$-*b*-PAA_{109} aqueous solutions at pH 3. Taken from Ref. 193.

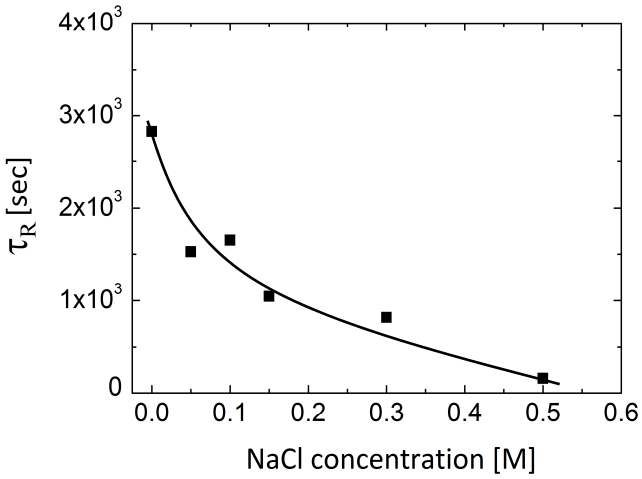

Fig. 5.2: Salt concentration dependence of the terminal relaxation time of 3 wt% PAA_{109}-*b*-$P2VP_{819}$-*b*-PAA_{109} aqueous solutions at pH 3. Taken from Ref. 193.

In the previous chapter, in studies on similar polyampholyte systems, we have shown that the fluctuation-induced attractions between oppositely charged PAA and P2VP chains leads to the formation of interpolyelectrolyte complexes (IPEC). The latter ones act as physical cross-links and maintain the integrity of the network. According to authors, significant reduction in viscosity and terminal relaxation time is due to enhanced exchange dynamics of the PAA chains from their junctions, caused by weakened integrity of the latter ones upon electrostatic screening inside the IPEC after salt addition.

5.4. Structural investigation

The present chapter 5.4 is based on ref. [193].

In order to identify the changes in the mesoscopic structure of hydrogels, being at the origin of the observed rheological behavior, we perform small-angle neutron scattering on hydrogels at low NaCl concentrations, *i.e.* up to 0.15 M. The choice of studied salt concentration range was driven by the proximity to the physiological conditions (~ 0.1 M NaCl).

5.4.1. Hydrophobic effect

In the present chapter we focus on the influence of ionic strength on the structure of hydrogels from the nonquaternized polyampholyte PAA_{109}-*b*-$P2VP_{819}$-*b*-PAA_{109}, *i.e.* the system with a prevailing hydrophobic effect. In figure 5.3, the SANS curves of PAA-*b*-P2VP-*b*-PAA at pD 3.0 and different NaCl concentrations are compiled. For the salt-free solution, the scattering curve shows two pronounced peaks (fig. 5.3a). The shoulder at q ~ 0.2 nm^{-1} was associated with a micellar form factor, whereas the peak at lower q values (~ 0.1 nm^{-1}) was ascribed to the structure factor, describing the interaction between the micelles. The scattering curves for solutions of PAA-*b*-P2VP-*b*-PAA with 0.05 M and 0.1 M of NaCl are very similar to the one of the salt-free solution. All these three curves were successfully fitted with the same model, which includes the form factor of homogeneous spheres with a Gaussian distribution of the radii ($P_{sph}(q)$, Eq. 3.43) together with a Percus-Yevick structure factor ($S_{HS}(q)$, Eq. 3.61), a modified Porod law ($P_P(q)$, Eq. 3.41), accounting for the scattering at q < 0.05 nm^{-1}, and an Ornstein-Zernike term:

$$I(q) = P_{sph}(q)S_{HS}(q) + S_{OZ}(q) + P_P(q) + I_{bkg} \tag{5.1}$$

implying the formation of a 3D network from spherical particles. These particles resemble the interpolyelectrolyte complexes, which form as a result of attractive electrostatic interactions between positively charged P2VP and negatively charged PAA chains. The complexation is accompanied by a simultaneous release of counterions, which are further substituted with oppositely charged polymer chains. In previous studies on similar polyampholyte systems (Chapter 4), the core-shell architecture instead of homogeneous spherical shape of aggregates was deduced. The cores were assigned to interpolyelectrolyte complexes, surrounded by the shell from non-complexed ionized P2VP chains. We explain this discrepancy by the fact, that

the polyampholyte system in the present study has shorter block lengths and is at lower concentration, which assumably results in a more random distribution of complexed P2VP and PAA chains inside the particle, so the shell cannot be distinguished.

In figure 5.4, the parameters obtained from fitting of the SANS curves in figure 5.3 are presented. From figure 5.4a it can be seen that the resulting particle radius does not vary significantly with increasing ionic strength up to 0.1 M NaCl. It is found at R_{sph} = 8.1 ± 0.6 nm, 7.2 ± 0.6 nm and 8.3 ± 0.9 nm for the hydrogel without salt, with 0.05 M and 0.10 M of NaCl, respectively. These complexes are bridged by the non-associated ionized P2VP segments on the middle chains. The repulsion between equally charged units on bridging P2VP chains leads to their stretching, resulting in a large average distance between the micelles. The hard-sphere radius is found at R_{HS} = 29.5 ± 0.3 nm and 31.5 ± 0.7 nm for the hydrogel without salt and with 0.10 M of NaCl, respectively (fig. 5.4a), demonstrating weak dependence on ionic strength. The volume fraction of micelles being part of the network, slightly increases from η_{HS} = 0.21 ± 0.05 for the hydrogel without salt to 0.25 ± 0.02 at 0.10 M NaCl (fig. 5.4b). From the forward scattering, the Porod exponent is found at α_P = 4.4 ± 0.2, 4.1 ± 0.2 and 4.6 ± 0.1 at 0 M, 0.05 M and 0.1 M of NaCl, respectively, which denotes the formation of compact aggregates with a surface concentration gradient.

Therefore, below the concentration of 0.1 M NaCl, there are no significant changes in the internal architecture of the hydrogel, but only minor redistribution of chains between the complexes, implying that the network is stable in this NaCl concentration range.

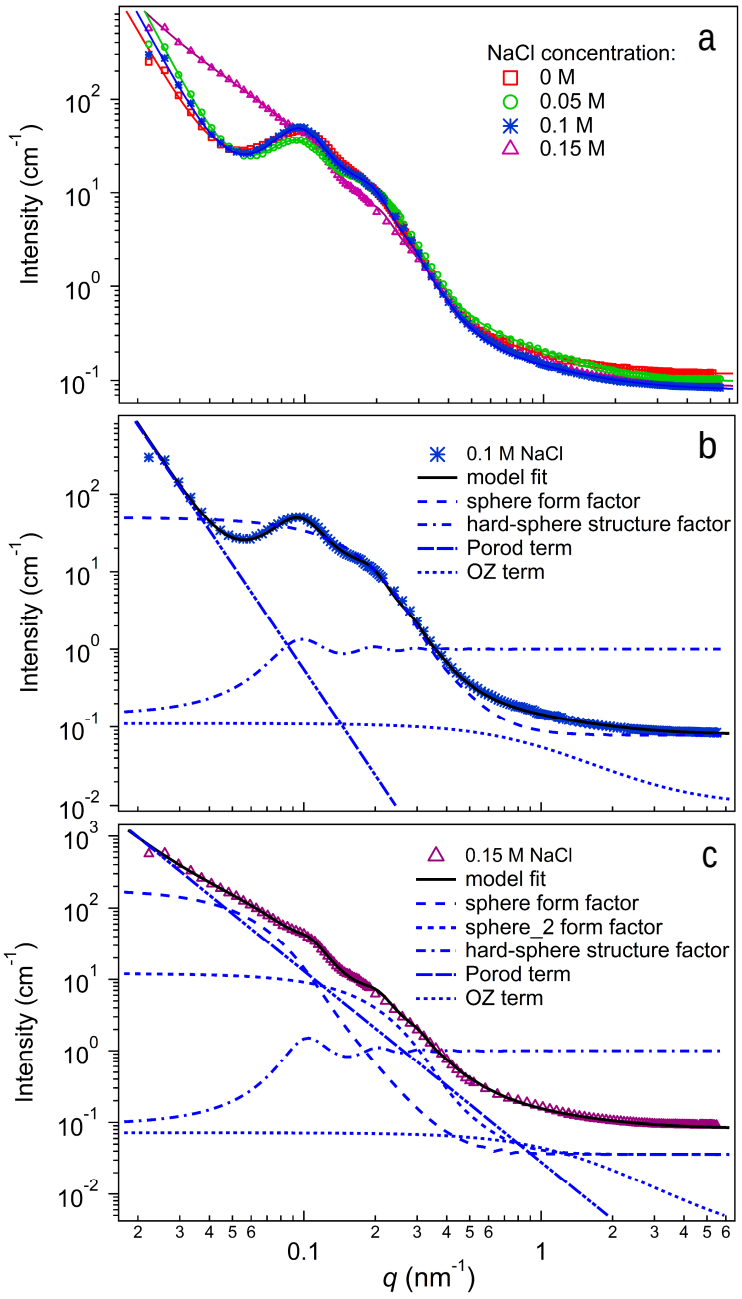

Fig. 5.3: SANS curves of 3 wt% PAA_{109}-*b*-$P2VP_{819}$-*b*-PAA_{109} aqueous solutions at pD 3 and 26 °C with different NaCl concentrations (a); (b,c) Same experimental data from (a) with the contributions to the model fit: with 0.1 M (b) and 0.15 M of NaCl (c). The symbols represent the experimental data. The solid lines represent the model fits, and the non-continuous lines contributions to the model. Taken from Ref. 193.

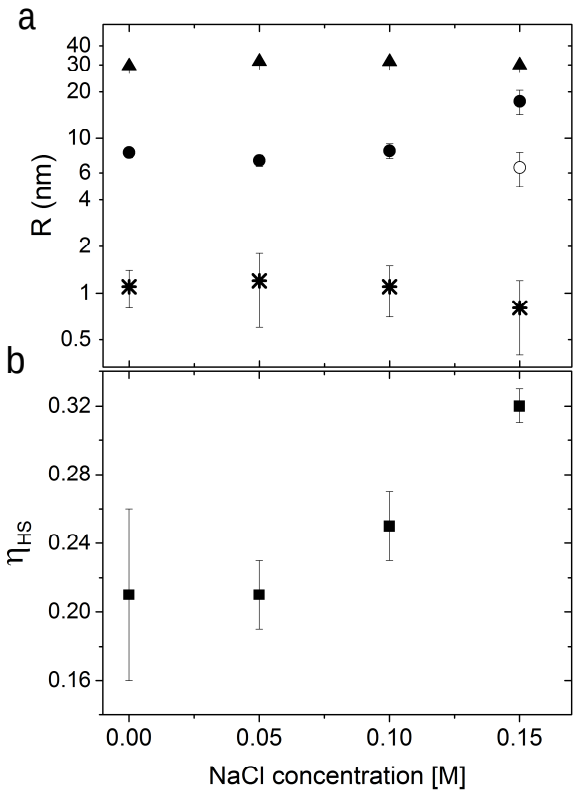

Fig. 5.4: Parameters from fitting of the SANS curves of PAA_{109}-*b*-$P2VP_{819}$-*b*-PAA_{109} at pD 3 in Fig. 5.3: (a) sphere radius, R_{sph} (solid circles); radius of small spheres, R'_{sph} (open circle); hard-sphere radius, R_{HS} (solid triangles) and correlation length, ξ (stars); (b) Volume fraction, η_{HS}. Taken from Ref. 193.

The scattering curve of the hydrogel with 0.15 M of salt has a significantly different shape in comparison to the ones at lower NaCl concentrations (fig. 5.3c). Thus, both, the shoulder at $q \sim 0.2$ nm^{-1} and the peak of a structure factor become weaker, whereas the forward scattering at $q < 0.05$ nm^{-1} changes its slope and becomes more pronounced. The scattering curve was fitted using the model, which includes the same parameters as at lower salt concentrations (Eq. 5.1), but now the additional form factor of small spherical particles, $P'_{sph}(q) = P_{sph}(q)$ (Eq. 3.43), not correlated into a network, was included (fig. 5.3c):

$$I(q) = P_{sph}(q)S_{HS}(q) + P'_{sph}(q) + S_{OZ}(q) + P_P(q) + I_{bkg}\,. \tag{5.2}$$

The radius of big complexes is found at $R_{sph} = 17.4 \pm 3.1$ nm (fig. 5.4a). We suppose that these are formed by small micelles, initially present in solution. Upon screening of charges, the micelles become more hydrophobic and aggregate with each. In addition to that, salt ions

partially screen the excess positive charge on ionized bridging P2VP blocks, which shrink and bring different micelles together, forming bigger aggregates.

The radius of small uncorrelated spheres is determined at R'_{sph} = 6.5 ± 1.6 nm, which is similar to the size of micelles at lower salt concentrations. Presumably, these small spheres are formed from collapsed neighboring P2VP moieties upon their partial neutralization on long bridging chains. The big complexes are correlated into a 3D network. The hard sphere radius is determined at R_{HS} = 29.9 ± 0.8 nm, which is similar to the one at lower salt concentrations. Thus, the size of complexes grows, whereas the distance between them remains unchanged. This is a result of the simultaneous shrinkage of bridging P2VP chains upon salt addition, which brings the complexes closer to each other. Additional factor, influencing the distance between the aggregates, is their uncompensated surface charge from ionized $P2VPH^+$. Thus, it gets screened with increasing ionic strength, lowering the repulsion between the aggregates.

The modified Porod term gives a Porod exponent α_P = 2.7 ± 0.1, which is significantly lower than at lower salt concentrations. We assume that big aggregates, which were present at lower ionic strengths, disintegrate into smaller fractal-like aggregates. Thus, increase in ionic strength provokes the breakup at large length scales, which explains the continuous decrease of the viscosity (fig. 5.1b). From fitting of the Ornstein-Zernike term in Eq. 5.2, we derive the average distance between the interconnected chains at ξ = 1.0 nm, similar to that one observed at lower NaCl concentrations. This supports an idea that the network organization occurs as a result of attractive electrostatic interactions. In figure 5.5, the schematic structures of the hydrogels, derived from SANS analysis, are depicted.

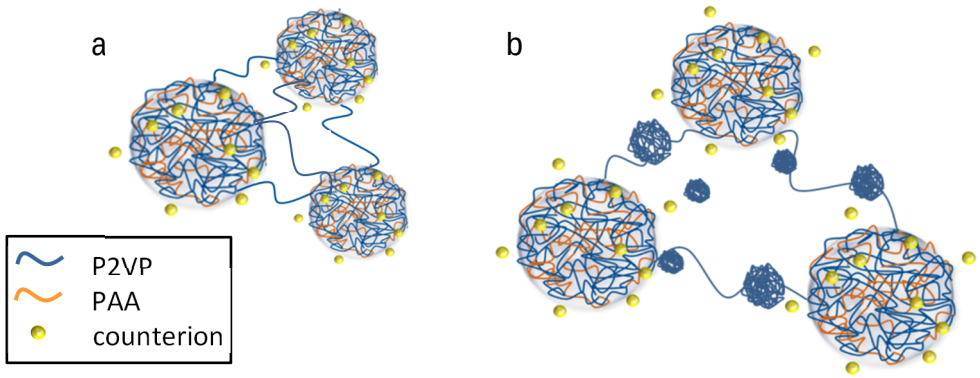

Fig. 5.5: Schematic illustration of self-associated structures of the hydrogels from PAA_{109}-*b*-$P2VP_{819}$-*b*-PAA_{109} without salt (a) and with 0.15 M of NaCl (b). Taken from Ref. 193.

5.4.2. Electrostatic effect

In chapter 4, in studies on similar systems, it was shown that the nonquaternized polyampholyte forms a stronger gel and has a lower percolation threshold in comparison to the one from the quaternized system. We correlated this finding with a higher number of P2VP bridging chains in the former case. The bridging chains are hydrophobic and, being "frozen", contribute additionally to the stiffening of the network. In the quaternized system, the number of ionized QP2VP chains is considerably higher. Repulsion between these increase their mobility, lowering in this way the integrity of bridging chains. In order to evaluate the influence of hydrophobicity and charge density on the response to ionic strength variation, we perform SANS on PAA_{109}-*b*-$QP2VP_{819}$-*b*-PAA_{109} at pD 5.0. At this pD, the fraction of ionized AA units reaches 55%; at the same time QP2VP is almost fully (~97%) charged. Because of this high charge density, we expect that predominantly electrostatic interactions will define the response of the system upon NaCl addition.

In figure 5.6a, the compiled SANS curves of PAA_{109}-*b*-$QP2VP_{819}$-*b*-PAA_{109} at pD 5.0 are presented for NaCl concentrations up to 0.15 M. The scattering curve of the salt-free solution is very similar to the one of the salt-free nonquaternized hydrogel at pD 3.0 (fig. 5.3a). However, for the present system, the curves undergo some changes at lower NaCl concentrations, reflecting faster structural changes.

The curve of the salt-free solution was successfully fitted using Eq. 5.1. The same architecture as in the salt-free nonquaternized polyampholyte system was deduced – a network, consisting of spherical interpolyelectrolyte complexes of oppositely charged P2VP and PAA chains. The radius of complexes is found at R_{sph} = 7.1 ± 0.8 nm with rather high polydispersity of p = 0.5 ± 0.1. The hard-sphere radius, or the half-distance between the complexes, is of R_{HS} = 33.6 ± 0.5 nm, which is slightly bigger than the one in the nonquaternized system. We explain it by stretching of strongly protonated bridging P2VP chains. The volume fraction of correlated micelles is of η_{HS} = 0.19 ± 0.06, which is similar to the value for the nonquaternized system.

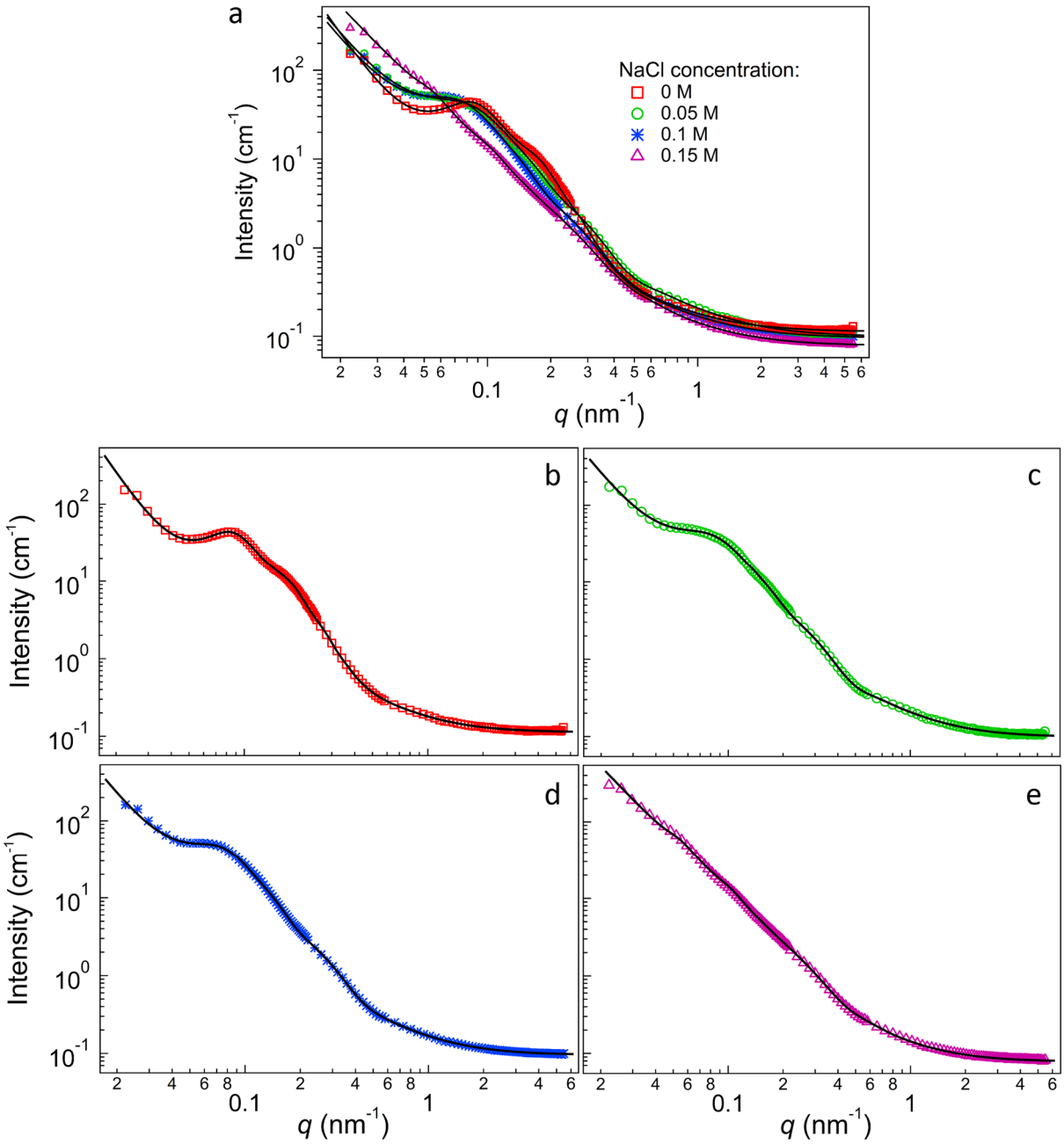

Fig. 5.6: SANS curves of 3 wt% PAA_{109}-*b*-$QP2VP_{819}$-*b*-PAA_{109} aqueous solutions at pD 5 and 26 °C together (a) and separately (b-e) with different NaCl concentrations: salt-free (b), 0.05 M (c), 0.1 M (d) and 0.15 M (e). The symbols represent the experimental data, and the solid lines the model fits, see text. Taken from Ref. 193.

The scattering curves after addition of salt were modelled using Eq. 5.2. The complex radius increases from R_{sph} = 14.2 ± 0.3 nm at 0.05 M to 18.5 ± 0.4 nm at 0.15 M NaCl (fig. 5.7a). Therefore, in contrast to the nonquaternized system, the size of complexes starts to grow already

after addition of 0.05M NaCl. Salt ions screen charges on both ionized blocks inside the complexes, resulting in enhanced hydrophobicity of the latter ones. This, in turn, provokes their further agglomeration into large aggregates. As in the nonquaternized hydrogel, the small additional globules from collapsed P2VP segments on bridging blocks are present. From figure 5.7a it can be seen that the radius of these globules does not vary significantly with increasing ionic strength. Thus, it is of R'_{sph} = 7.3 ± 0.3 nm at 0.05 M and 8.6 ± 0.5 nm at 0.15 M.

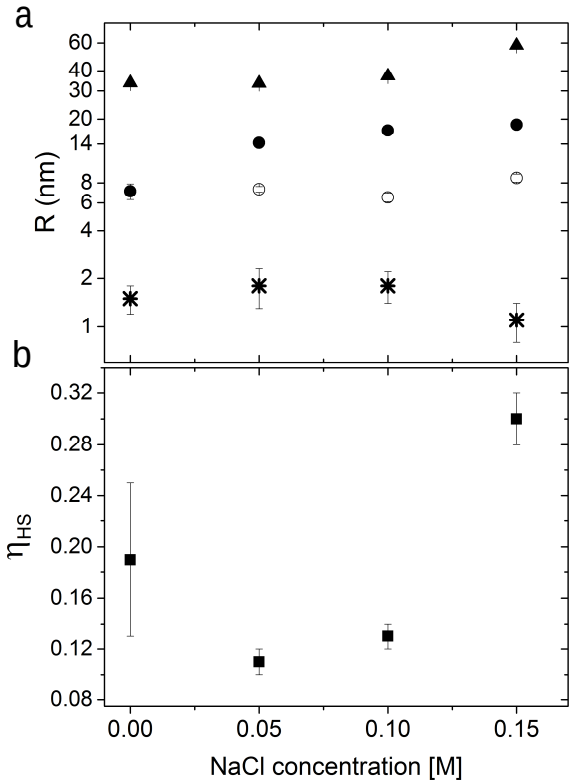

Fig. 5.7: Parameters from fitting of the SANS curves of PAA_{109}-*b*-$QP2VP_{819}$-*b*-PAA_{109} at pD 5 in Fig. 5.6: (a) sphere radius, R_{sph} (solid circles); radius of small spheres, R'_{sph} (open circles); hard-sphere radius, R_{HS} (solid triangles) and correlation length, ξ (stars). (b) Volume fraction, η_{HS}. Taken from Ref. 193.

In contrast to the situation in the nonquaternized hydrogel, here, the hard-sphere radius grows in line with the complex radius increasing ionic strength. It increases from R_{HS} = 33.6 ± 0.5 nm in the salt-free hydrogel to R_{HS} = 57.9 ± 1.1 nm at 0.15 M NaCl (fig. 5.7a). We assume that NaCl ions at this concentration are not sufficient to screen excess positive charge on P2VP chains, which keeps the complexes at preferred distance from each other.

The volume fraction is found to decrease from η_{HS} = 0.19 ± 0.06 in the salt-free solution to η_{HS} = 0.11 ± 0.01 at 0.05 M of NaCl (fig. 5.7b). We explain it by lowered connectivity in the system due to the reason that a certain fraction of the P2VP segments aggregate now into small globules, reducing the number of potentially bridging chains. Additionally, middle P2VP blocks become shorter, carrying collapsed P2VP "blobs", and cannot bridge the complexes. Increasing salt concentration to 0.15 M, the volume fraction increases to η_{HS} = 0.3 ± 0.02, manifesting the network is again strongly correlated. This is presumably due to the hydrophobic effect of the non-ionized QP2VP blocks, whose fraction rises with increasing salt content.

From fitting Eq. 5.2, the Porod exponent is found to gradually decrease from α_P = 3.4 ± 0.2 in the salt-free solution to α_P = 3.1 ± 0.1, 3.0 ± 0.1 and 2.5 ± 0.1 after addition of 0.05 M, 0.1 M and 0.15 M of NaCl. Upon screening of electrostatics, degree of the density of packing in the aggregates decreases, followed by their partial disintegration. The average value of the correlation length is deduced at ξ = 1.5 nm, which is similar to the one in the nonquaternized system.

Concluding, both systems form a three dimensional network. The high connectivity is possible due to the presence of high number of elastically active charged QP2VP/P2VP chains, which act as bridging links. In both systems, salt ions screen the electrostatic repulsion along the bridging chains and between the complexes, resulting in the hydrophobic aggregation of the latter ones. The hydrogel from the nonquaternized polyampholyte maintains its initial conformation upon higher variations in ionic strength, *i.e.* 0.1 M of NaCl, demonstrating only small internal rearrangements in the network. This is due to the enhanced hydrophobic effect from large fraction of non-ionized P2VP chains, which strengthen the network and lower the impact from screening. At higher salt concentrations, despite the structure changes, network is still present. Presumably, higher salt amounts are needed to screen charges along the bridging P2VP chains to shorten them sufficiently in order to disrupt the integrity of the network. In contrast in the quaternized system, significant changes in the network architecture are observed already at 0.05 M of NaCl. We correlate this with the higher charge density in the system, *i.e.* higher number of ionized Q2VP/AA units, which can be readily screened, leading to faster structural changes in the network.

5.5. Dynamical studies

The present chapter is based on ref. [193].

By means of dynamic light scattering (DLS) we aim to study dynamics in the polyampholyte hydrogel. Hydrogels represent complex systems, which demonstrate dynamic behavior of both: liquid – on the short-time scale, and solid – on the long-time scale. Therefore, several relaxation processes may be expected, such as diffusion of single complexes and aggregates or correlated network dynamics. Most of hydrogels, being non-ergodic and highly elastic systems, are difficult to study using conventional DLS. In figure 5.8, the intensity autocorrelation curve from conventional DLS of the solution of PAA_{109}-*b*-$P2VP_{819}$-*b*-PAA_{109} at concentration of 3 wt% at pD 3 is presented. The curve exhibits strong oscillations, characteristic for elastic systems, like gel networks.

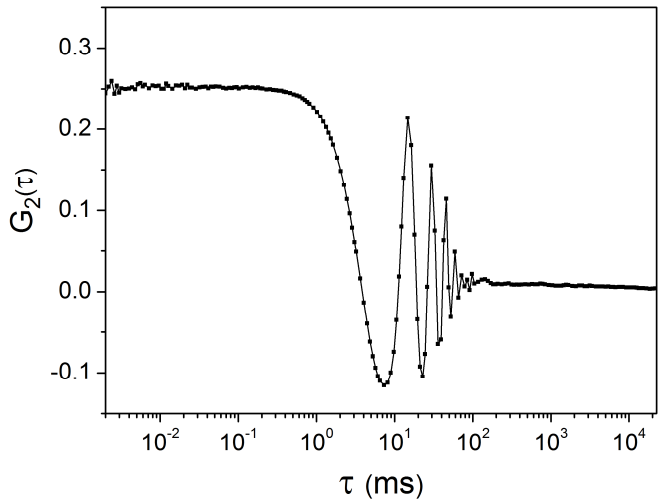

Fig. 5.8: Intensity autocorrelation curve from conventional DLS of 3 wt% aqueous solution of PAA_{109}-*b*-$P2VP_{819}$-*b*-PAA_{109} at pD 3 at 26 °C.

In order to suppress the long-time correlations, and to measure the fast internal dynamics of the network independently, the sample was constantly rotated in the incident beam during the measurements.

In figure 5.9a, the intensity autocorrelation curves from rotational DLS of the solutions of PAA_{109}-*b*-$P2VP_{819}$-*b*-PAA_{109} in D_2O at pD 3.0 with different salt concentrations are presented. All correlation functions have similar shape and exhibit a fast decay at $\tau \sim 1$ ms. The second decay, denoting a slow dynamics in the system ($\tau >$ a few ms), is still visible, although it is strongly suppressed by rotation. We associate the second decay with the slow diffusion of large

aggregates, which were observed earlier from the forward scattering in SANS (fig. 5.3a). The autocorrelation curves were fitted using Eq. 3.79, a double stretched exponential decay. The fitting with a single exponential decay gives unsatisfactory fit at longer relaxation times. Nevertheless, since the second decay indicates the contribution from the ultraslow non-ergodic dynamics, it was not evaluated quantitatively.

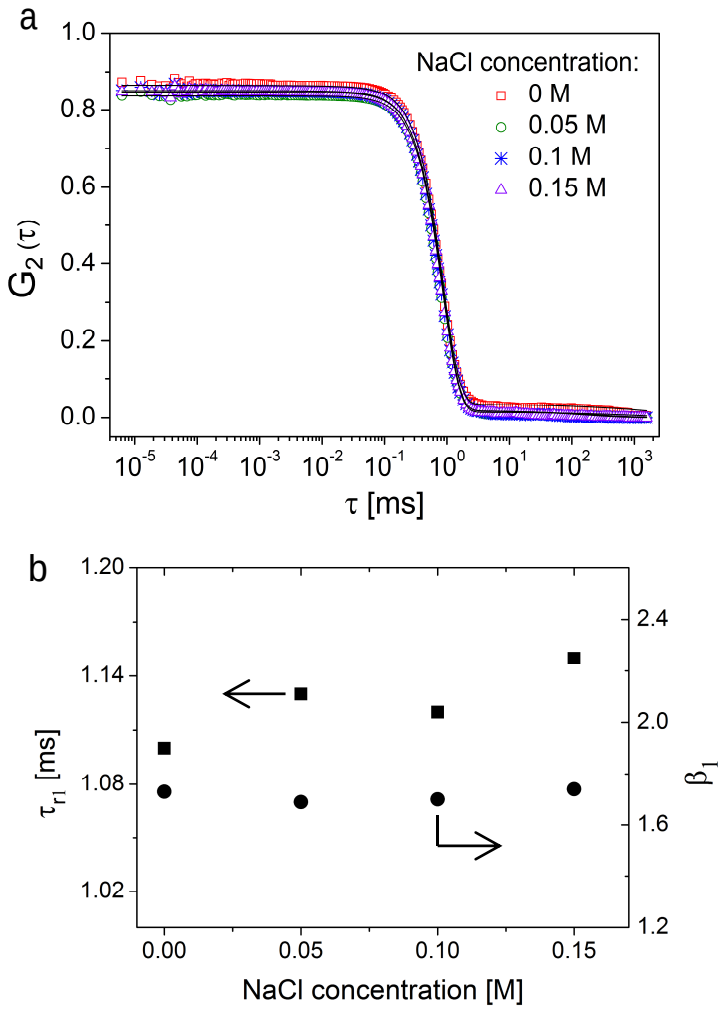

Fig. 5.9: (a) Intensity autocorrelation curves from rotational DLS of 3 wt% PAA_{109}-*b*-$P2VP_{819}$-*b*-PAA_{109} aqueous solutions at pD 3 at 26 °C for different NaCl concentrations. The solid black lines are the model fits. (b) Parameters from fitting of the DLS curves from (a): relaxation times of the fast decay, τ_{r1} (squares, left axis) and stretching exponents, β_1 (circles, right axis). Taken from Ref. 193.

The fast decay describes the fast dynamics in the hydrogel. From figure 5.9a it can be seen that the fast mode is not significantly influenced with increasing ionic strength. The relaxation time

has a weak dependence on salt concentration and is in the range τ_{r1} = 1.10 – 1.15 ms (fig. 5.9b). By fitting Eq. 3.79, we derive the value of stretching exponent in the range β_1 = 1.69 – 1.74. The unusually high value of exponent is indicative of the dynamic behavior in concentrated frozen systems with constrained internal inhomogeneities. Bandyopadhyay et al.[194] in their studies on solutions of highly charged laponite particles have shown that the electrostatic repulsion between the latter ones restricts their motion, resulting in a stretching exponent of 1.5. Similar findings were observed by Cipelletti et al. in their studies on jammed soft materials.[195] They propose that the ultraslow, large length scale ballistic motion of the scatterers ($\beta \sim 1.5$) is caused by the relaxation of internal stresses, emerged during the jamming transition. Among the other factors, influencing the dynamics, are variations in solvent quality or phase separation.[196] We suppose that the steep decay for the salt-free system is related to the relaxation of the inner stress, arising from the presence of both – electrostatic attraction between the chains inside the complexes and repulsion between the charged aggregates. As a result, the network appears "frozen" and cannot relax on the time scale of the measurement. The weak salt dependence of the relaxation time indicates that the complexes are stable in the entire range of NaCl concentrations, chosen for the present study.

The findings from the dynamic studies are consistent with the conclusions, derived from SANS studies, that the network maintains its connectivity even at high ionic strengths.

5.6. Conclusions

The influence of the ionic strength on the structure and dynamical behavior of hydrogels from the nonquaternized PAA-*b*-P2VP-*b*-PAA polyampholyte at pD 3.0 was studied using small-angle neutron scattering and rotational dynamic light scattering. In this system, the degrees of ionization of both blocks are relatively low, and the uncharged polymer chains are hydrophobic. This makes the hydrophobic interactions in the system prevailing, minimizing the influence from the electrostatics on the polymer behavior in solution. As the reference system, the quaternized polyampholyte PAA-*b*-QP2VP-*b*-PAA at pD 5.0 was chosen. In this system, the degrees of ionization of both blocks are higher, which enhances the influence from the electrostatic interactions. We investigated the structural changes in the networks of these two systems upon variation in ionic strength.

Small-angle neutron scattering studies in both salt-free systems revealed strong networks from homogeneous spherical particles from complexed oppositely charged P2VP and PAA chains. These complexes are bridged together by those segments of the P2VP blocks, not associated with PAA.

In both systems, the complex radius grows with NaCl concentration. This was attributed to the transition of the system from a polyampholyte regime to a non-charged state. In the nonquaternized system, the maximum growth occurs at 0.15 M of NaCl, related to the reduced charge density in the system. In the quaternized polyampholyte, the hydrophobically triggered aggregation and growth of complexes occurs already at 0.05 M of NaCl.

The network organization in two systems evolves differently. In the nonquaternized system, the network is more stable and retains its initial conformation upon higher variations in ionic strength. Thus, the distance between the complexes remains the same in the entire range of studied NaCl concentrations. This was related to the fact, that the gel network does not exhibit only interpolyelectrolyte complexes but additionally is stabilized by the presence of hydrophobic units along the P2VP blocks. Thus, hydrophobic effect noticeably enhances the mechanical stiffness of the network. In contrast in the quaternized system, where electrostatic interactions are predominant, the distance between the complexes follows the growth of aggregates and increases with NaCl concentration. In both systems, the hydrophobic P2VP segments form additional small spheres on the bridging chains, which may restrict fluctuations of the length of bridging P2VP chains.

Rotational dynamic light scattering allowed us to resolve different dynamical processes in the hydrogel networks from the nonquaternized polyampholyte. The fast dynamics was attributed to the relaxation of internal stresses in highly cross-linked network, whereas the slow dynamics was ascribed to the slow diffusion of large aggregates, formed upon the hydrophobic agglomeration in the system on the large length scales. The network is found to be stable at all salt concentrations.

Concluding, the high charge density in PAA-*b*-QP2VP-*b*-PAA makes the system more sensitive to charge screening, resulting in well-defined gradual weakening of the network. In contrast, the high hydrophobicity in PAA-*b*-P2VP-*b*-PAA enhances the rigidity of the network, and the system preserves the connectivity up to higher salt concentrations.

6. Self-assembling physical hydrogels from telechelic polyampholytes

In previous chapters 4 and 5, we have shown that morphological and dynamical properties of polyampholytes are defined by the charge asymmetry and charge density on polymer. In polyampholytes, both blocks are ionizable, and the resulting behavior in solution is determined by the extent of electrostatic interactions between these blocks. Change in charge asymmetry would dictate which of the two electrostatic forces: attractive or repulsive – would prevail. In contrast, change in charge density or total fraction of ionized units would affect the extent of both: electrostatic and hydrophobic interactions present in the system, and the resulting gelation ability.

In the present chapter we move further and investigate the influence of the charge density on the structure of hydrogels from the triblock terpolymer PMMA-*b*-P(DEA-*co*-MAA)-*b*-PMMA (PMMA, PDEA and PMAA are poly(methyl methacrylate), poly(2-(diethylamino)ethyl methacrylate) and poly(methacrylic acid)), after variation of pH. In comparison to the previously studied polyampholytes (Chapters 4,5), the terpolymer in present study along with the middle polyampholytic hydrophilic P(DEA-*co*-MAA) block, comprises the hydrophobic PMMA outer blocks. In aqueous solutions, the latter ones associate forming the micellar cores, which are bridged by middle blocks. In present study, the polyampholytic middle block is a random copolymer, which implies that the degree of polymerization of elastic bridging blocks remains the same at all pH. However, the degrees of ionization of both PDEA and PMAA inside the middle block are pH-dependent, and thus the pH variation is expected to influence the conformation and solubility of the middle block, which defines its ability to act as elastic chains, contributing to the network formation. The behavior of the entire polymer in solution and its gelation properties are determined by the interplay between the hydrophobic associations of the outer blocks and the electrostatic interactions inside the polyampholytic block. In order to examine the effect of the polymer concentration and the charge density on the structure of hydrogels, SANS measurements were carried out in dilute and semi-dilute regime.

6.1. System

The present section is based on refs. [140,197-198].

We investigate the influence of the pH value of the solution on the structure of hydrogels from the triblock terpolymer poly(methyl methacrylate)-*b*-poly(2-(diethylamino)ethyl methacrylate-*co*-methacrylic acid)-*b*-poly(methyl methacrylate) $PMMA_{86}$-*b*-$P(DEA_{190}$-*co*-$MAA_{96})$-*b*-$PMMA_{86}$ (M_w = 60100 $gmol^{-1}$, M_w/M_n = 1.30).[198] The polymers were synthesized by Dr. George Gotzamanis (Department of Chemical Engineering, University of Patras, Patras, Greece). The details of the synthesis can be found elsewhere.[197] The middle block has a weak ampholytic nature, and its conformation is defined by the charge density on both PDEA and PMMA (figure 6.1).

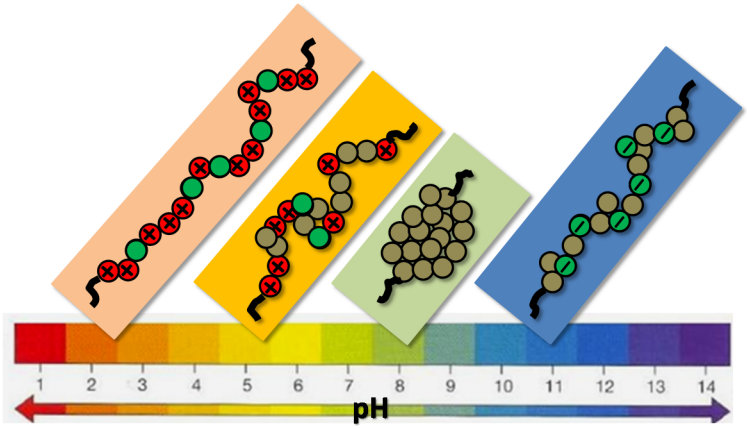

Fig. 6.1: The pH induced variation of the degree of ionization of PDEA and PMAA in the middle polyampholytic block of the PMMA-*b*-P(DEA-*co*-MAA)-*b*-PMMA triblock terpolymer (DEA and MAA repeating units are in red and green spheres, respectively). The grey spheres denote neutralized and/or hydrophobic PDEA or PMAA moieties. Taken from Ref. 198.

PDEA exhibits pH-dependent protonation at low pH values, resulting in a positive net charge of the block (fig. 6.1, 6.2a). Increasing pH, the fraction of protonated $DEAH^+$ units decreases, and so the *z*-potential (fig. 6.2a). Because the polyampholytic block along with the PDEA segments carries short negative PMAA segments, whose degree of ionization increases with pH, the net charge of the polymer alters with pH (fig. 6.1, 6.2a). From figure 6.2a it can be seen that, increasing pH from low (acidic) to high (basic) values, the *z*-potential changes sign, from positive at low pH, where ionized PDEA predominate, to negative at high pH, where deprotonated PMAA segments prevail since PDEA has been transformed to neutral and

hydrophobic. In the range of pH values between 7.6 and 8.8 (isoelectric point at pH 8.2, zero net charge), the polymer precipitates due to neutralization of the opposite charges (fig. 6.2a dashed region, 6.2b).

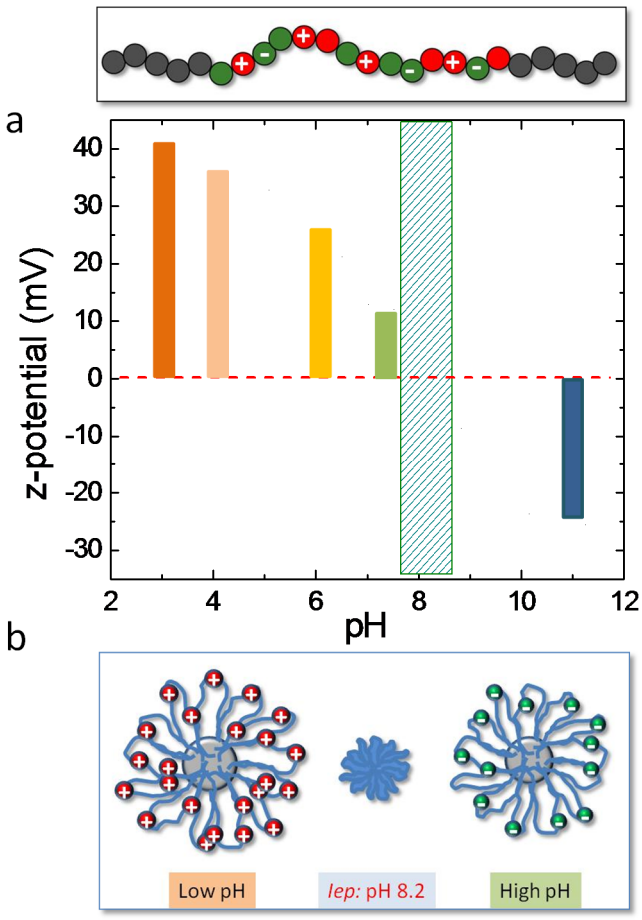

Fig. 6.2: (a) Zeta-potential (mV) of 0.5 wt% $PMMA_{86}$-*b*-P(DEA_{190}-*co*-MAA_{96})-*b*-$PMMA_{86}$ aqueous solutions at various pH values. The dashed region denotes the precipitation region. (b) Schematic representation of self-assembled structures. Taken from Ref. 198.

6.2. Materials and instrumental set-up

Sample preparation. The samples for rheological studies were prepared by Dr. George Gotzamanis (Department of Chemical Engineering, University of Patras, Patras, Greece). The details of the sample preparation can be found in Refs. 197,198.

The samples for structural and dynamical studies were prepared by dissolution of $PMMA_{86}$-*b*-P(DEA_{190}-*co*-MAA_{96})-*b*-$PMMA_{86}$ in D_2O at 3 wt% and 0.05 wt% at room

temperature. pD values of 3.0 and 4.0 were fixed by adding 0.1 M hydrochloric acid (HCl) in D_2O. The appropriate amount of 0.1 M sodium hydroxide NaOH in D_2O was added to install pD values of 6.0, 7.4 and 11.0.

Rheometry. Measurements were performed on a stress controlled Rheometric Scientific SR 200 rheometer, equipped with a cone and plate geometry (diameter = 25 mm, cone angle = 5.7°, truncation = 56 μm). After each sample loading, a delay of 5 min was applied before each measurement, in order to erase the mechanical history. The temperature was fixed at 25 ± 0.1 °C. The linear viscoelastic regime was established by oscillatory strain sweeps at constant frequency of 0.5 Hz.

Small-angle neutron scattering (SANS). Measurements were carried out at the instrument KWS-1 at the JCNS outstation at MLZ in Garching, Germany. The neutron wavelength was chosen at λ = 0.47 nm with a spread $\Delta\lambda/\lambda$ = 20 %. Using sample-detector distances (SDDs) of 1.17, 7.67 and 19.67 m, a range of momentum transfers q = 0.026 to 4.9 nm^{-1} was covered. The exposure times were 10, 25 and 45 min at SDD = 1.17 m, 7.67 m and 19.67 m, respectively. The samples having pD 3.0, 4.0 and 6.0 at 3 wt% were mounted in 0.5 mm quartz glass cuvettes (Hellma). The samples at pD 7.4 and 11.0 at 3 wt% and all samples at 0.05 wt% were mounted in 1 mm quartz glass cuvettes (Hellma). All samples were measured at room temperature. The raw data treatment was performed following the procedures, described in Chapter 4 (section 4.2).

Rotational dynamic light scattering (DLS). Measurements were performed following the procedure described in Chapter 5 (section 5.2).

6.3. Rheological studies

The present chapter is based on refs. [140,197-198].

6.3.1. Rheological behavior in dilute solutions

Measurements in dilute and concentrated solutions were carried out by Dr. George Gotzamanis (Department of Chemical Engineering, University of Patras, Patras, Greece).

The present system was initially designed as pH-responsive gelator. The pH-dependent degree of ionization of both PDEA and PMAA defines the extent of electrostatic interactions between charged units and of hydrophobic associations of non-ionized groups, which, in turn, dictates the final architecture of micelles. In the previous studies, it was demonstrated that the telechelic polyampholyte in aqueous solutions forms a 3D network from the flower-like micelles with a core, composed from the hydrophobic PMMA end-blocks, and a corona from the hydrophilic polyampholyte P(DEA-*co*-MAA) blocks.[197] The size of aggregates, detected in further DLS studies, confirmed the existence of micelles (fig. 6.3a). From figure 6.3a it can be seen that, by moving away from the *iep* region, the hydrodynamic radius of aggregates, $R_{H,app}$, increases. It was explained by the increasing degree of ionization of the predominant charged moieties: the number of ionized $DEAH^+$ units increases with decreasing pH, while of ionized MAA^- units - with increasing pH. Thus, at pH values far below or above the *iep*, strong electrostatic repulsion along the middle polyampholytic block results in its extension in the shell of flower-like micelles (fig. 6.2b). The size of the aggregates in the acidic region was found to be larger compared to those in the basic region (fig. 6.3a). The authors assign the large aggregates at low pH to the clusters of micelles, bridged by strongly stretched protonated middle polyampholytic blocks. Further TEM studies revealed large irregular aggregates at low pH, whereas rather uniform small aggregates at high pH (fig. 6.3b), which is consistent with findings from DLS.

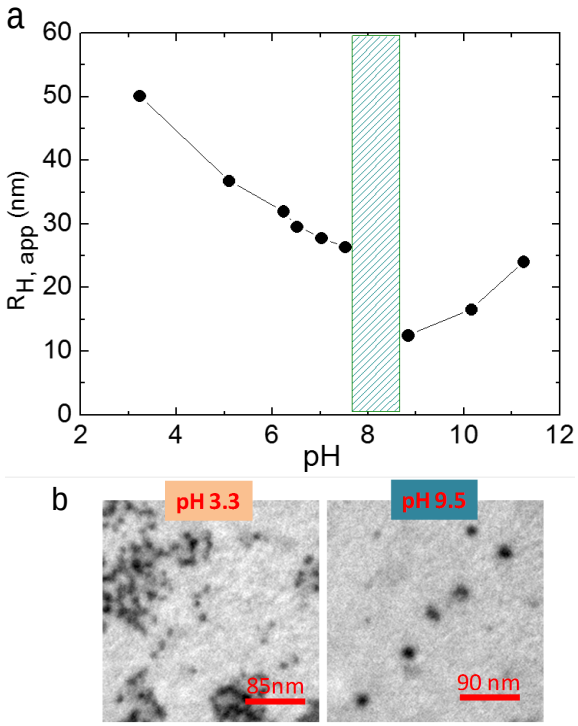

Fig. 6.3: (a) pH dependence of the apparent hydrodynamic radius, $R_{H,app}$. Data from conventional DLS. The shaded green area denotes the *iep* region. (b) TEM micrographs of $PMMA_{86}$-*b*-$P(DEA_{190}$-*co*-$MAA_{96})$-*b*-$PMMA_{86}$ at pH 3.3 and 9.5. Taken from Ref. 198.

6.3.2. Rheological behavior in concentrated solutions

In solutions of 3 wt% of PMMA-*b*-P(DEA-*co*-MAA)-*b*-PMMA, the gel is formed in the acidic region, whereas the viscous solutions are observed in the high pH region, *i.e.* above the *iep*. According to authors, in this pH region, a relatively low number of ionized MAA^- moieties (the ratio [DEA]/[MAA] ~ 2), interrupted by high number of deprotonated hydrophobic DEA moieties, does not allow the middle polyampholytic block to stretch long enough to bridge the micelles. The rheological properties in concentrated solutions were studied at pH values below *iep*.

Steady state shear viscosity measurements on obtained gels were carried out at different pH, and the viscosity versus shear stress profiles are presented in figure 6.4. It can be seen that at pH < 6 increasing the shear stress, a low-shear Newtonian region is followed by a sharp viscosity decrease and a subsequent shear-thinning. At pH 4, the maximum solution viscosity (several 10^4 Pa.s) and highest yield stress (about 35 Pa) were encountered, manifesting the

formation of a strong free-supporting hydrogel. Above pH 6, the viscosity was found to be a non-Newtonian, characterized by a continuous shear-thinning.

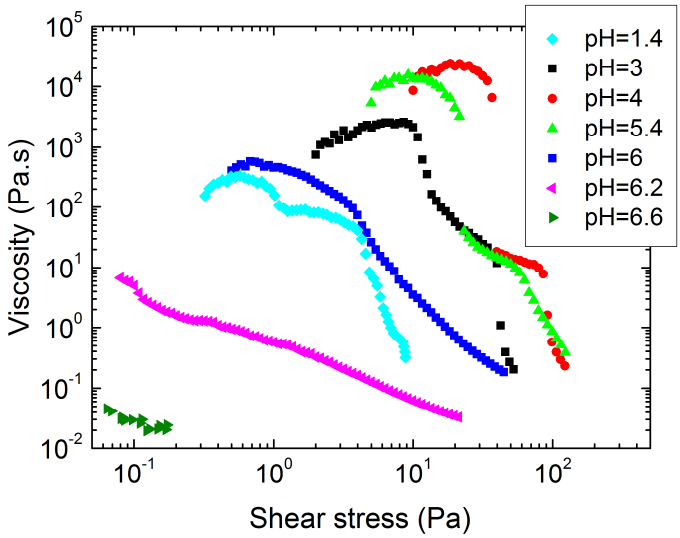

Fig. 6.4: Apparent shear viscosity as a function of the applied shear stress of 3 wt% $PMMA_{86}$-*b*-$P(DEA_{190}$-*co*-$MAA_{96})$-*b*-$PMMA_{86}$ aqueous solutions at different pH values. Taken from Ref. 198.

In figure 6.5, the authors compare the pH-dependent behavior of the low shear viscosity of the telechelic polyampholyte with the one of the telechelic polyelectrolyte $PMMA_{32}$-$PDEA_{224}$-$PMMA_{32}$ (contains only PDEA ionizable block). It was shown, that for both systems the viscosity continuously increases with pH and reaches its maximum at pH 4, while its behavior is different in two cases at higher pH. Thus, for the telechelic polyelectrolyte at 1 wt% at pH 7 (close to physiological pH), the viscosity remains high (of the order of 10^4 Pa.s). In contrary, for the telechelic polyampholyte even at higher concentration of 3 wt%, in the region $5.4 < pH < 6.6$, the viscosity drops by four orders of magnitude, revealing a gel-to-sol transition. The authors attribute it to the pronounced effect of the attractive interactions among $DEAH^+$ and MAA^- on the middle polyampholytic block (light green area in fig. 6.5), and propose that these interactions are predominantly intramolecular, resulting in a shrinkage of the bridging chains, preventing the formation of a 3D network. In comparison, in the telechelic polyelectrolyte, elastic bridging chains are composed from the middle polyelectrolyte blocks, which remain stretched and maintain the connectivity in the network. The main differences in flow behavior in these two systems were related by authors to the different ampholytic nature of the potentially elastic bridging blocks.

Moreover, the determined rheological behavior of the telechelic polyampholyte allows to use its aqueous solutions as an injectable hydrogel, *i.e.* for biomedical applications. Thus, being injected at the physiological pH 7.4, it forms a sol, whereas it transforms into a free-standing gel, reaching the tumor environment with pH 6.

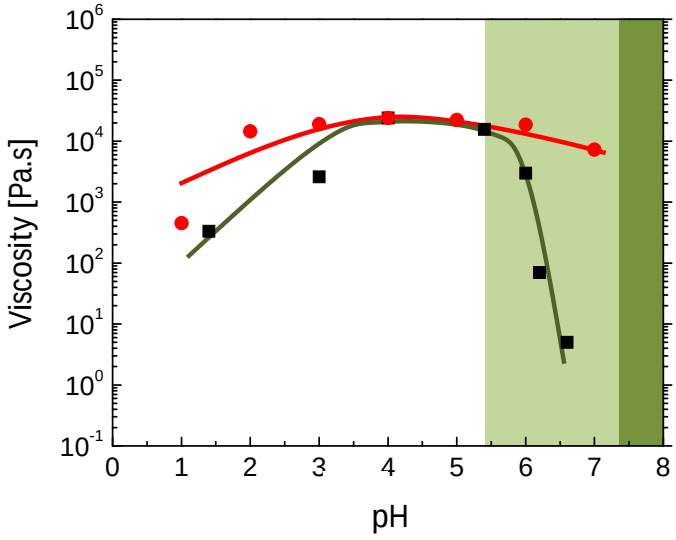

Fig. 6.5: Low shear viscosity as a function of pH for telechelic polyampholyte $PMMA_{86}$-*b*-$P(DEA_{190}$-*co*-$MAA_{96})$-*b*-$PMMA_{86}$ at c = 3 wt% (black squares) and for telechelic polyelectrolyte $PMMA_{32}$-*b*-$PDEA_{224}$-*b*-$PMMA_{32}$ at c = 1 wt% (red circles, from Ref. 136.) The light and dark green regions denote the region of the electrostatic attractions of the opposite charges on the polyampholyte and its precipitation region. Taken from Ref. 198.

Further studies on the viscoelastic behavior revealed different viscoelastic responses, depending on pH (fig. 6.6). In figure 6.6, the elastic, G', and loss modulus, G'', obtained in the linear viscoelastic regime, are plotted as a function of frequency at various pH. Both, G' and G'' were found to be frequency independent, with G' being 1 order of magnitude higher than G'' in the whole frequency range. The authors correlate long relaxation times − higher than 10^3 s (the G', G'' crossover is not visible) with the appearance of free-supporting hydrogels in this pH region (4 < pH < 6, at pH 5.4 the viscoelastic behavior is found to be similar to the one at pH 4). At pH 6, *i.e.* close to *iep*, both moduli were found to be significantly lower than those at pH 4. The G', G'' crossover was detected at $f = 2\times10^{-3}$ Hz, implying that the terminal relaxation time decreased to 500 s. The authors correlate the transition from the elastic gel to a viscoelastic fluid at this pH with the gel-to-sol transition, detected earlier (fig. 6.4, 6.5). Similar behavior was observed at pH far below the *iep*, *i.e.* 1.4 and 3.

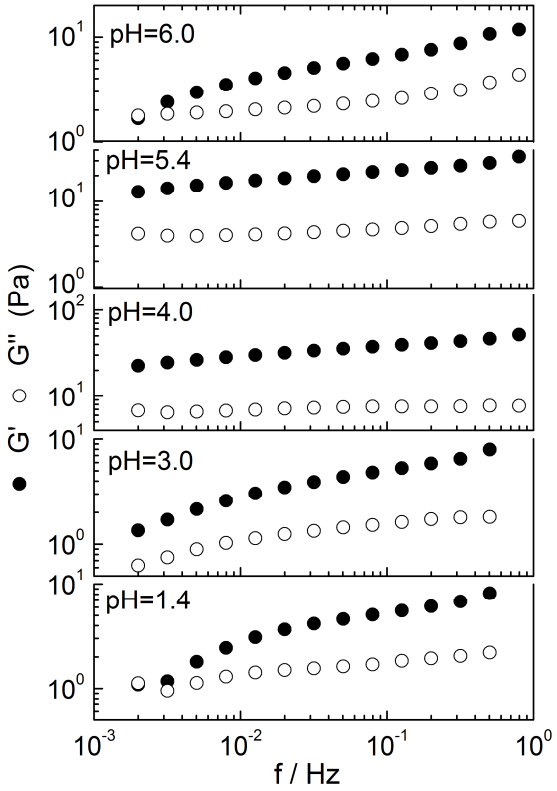

Fig. 6.6: Frequency dependence of dynamic moduli, *G′* (filled symbols) and *G″* (open symbols) of 3 wt% $PMMA_{86}$-*b*-$P(DEA_{190}$-*co*-$MAA_{96})$-*b*-$PMMA_{86}$ aqueous solutions at different pH values. Taken from Ref. 198.

6.4. Structural investigation

The present chapter is based on ref. [198].

6.4.1. Structural investigation in concentrated solutions

With the aim to identify the corresponding changes in the mesoscopic structures, responsible for a peculiar rheological behavior, the small-angle neutron scattering on 3 wt% $PMMA_{86}$-*b*-P(DEA_{190}-*co*-MAA_{96})-*b*-$PMMA_{86}$ solutions in D_2O at different pD values was performed (fig. 6.7). At low pD values, namely 3.0, 4.0 and 6.0, the scattering curves show a pronounced peak maximum at $q \sim 0.2$ nm^{-1}, associated with the electrostatic repulsion between the micelles, together with a rather stretched shoulder at higher q values, ascribed to the internal structure of the micelles. At q values below 0.07 nm^{-1}, the strong forward scattering is encountered (fig. 6.7a). The model fitting indicates that hydrogels at these pD values consist of charged fuzzy spheres ($P_{Fuz}(q)$, Eq. 3.52), interacting with each other via the screened Coulomb potential ($S_{RMSA}(q)$, Eq. 3.69):

$$I(q) = P_{Fuz}(q)S_{RMSA}(q) + P_P(q) + I_{bkg} \tag{6.1}$$

where $P_P(q)$ is the modified Porod law, which accounts for the scattering from large-scale inhomogeneities at low q values (Eq. 3.41). From fitting Eq. 6.1, the resulting particle core radius is found to increase from R_c = 2.2 ± 0.1 nm at pD 3.0 to 2.8 ± 0.2 nm at pD 6.0 (fig. 6.7b), whereas the interface thickness is nearly constant and has an average value of δ_{surf} = 2.0 ± 0.2 nm. The value of the core radius R_c is very similar to the one, obtained previously from TEM studies (~2.3 nm, fig. 6.3b). We suppose that the cores of the fuzzy spheres are formed by the hydrophobic PMMA blocks, whereas some non-ionized segments of the P(DEA-*co*-MAA) middle blocks form the interface. At low pD, the PDEA segments are strongly protonated (fig. 6.1). Being stretched, they spread out from the sphere surface, carrying the non-ionized PMAA segments and preventing their collapse with the PMMA cores. The growth of the core radius with increasing pD was attributed to the decreasing degree of ionization of the PDEA blocks. Increasing pD from 3.0 to 6.0, the fraction of non-ionized, and hence hydrophobic DEA units increases, while a big fraction of the MAA units still remain neutral. This enhances the hydrophobicity of the middle block, which causes it to fold back to the core. In addition, at pD 6.0, some of the MAA units are deprotonated (the pK_α of PMAA is 4.8)[136] and electrostatically interact with the remaining protonated DEA

units, which leads to their mutual neutralization, promoting the partial merging of the middle block with the PMMA cores.

The big difference between the hydrodynamic radius, derived previously from DLS (fig. 6.3a), and the radius of gyration, derived from SANS (fig. 6.7b) we explain by the fact, that the hydrodynamic radius in DLS corresponds to the one of the large aggregates from clustered micelles, which are at the origin of strong forward scattering in SANS (fig. 6.7a).

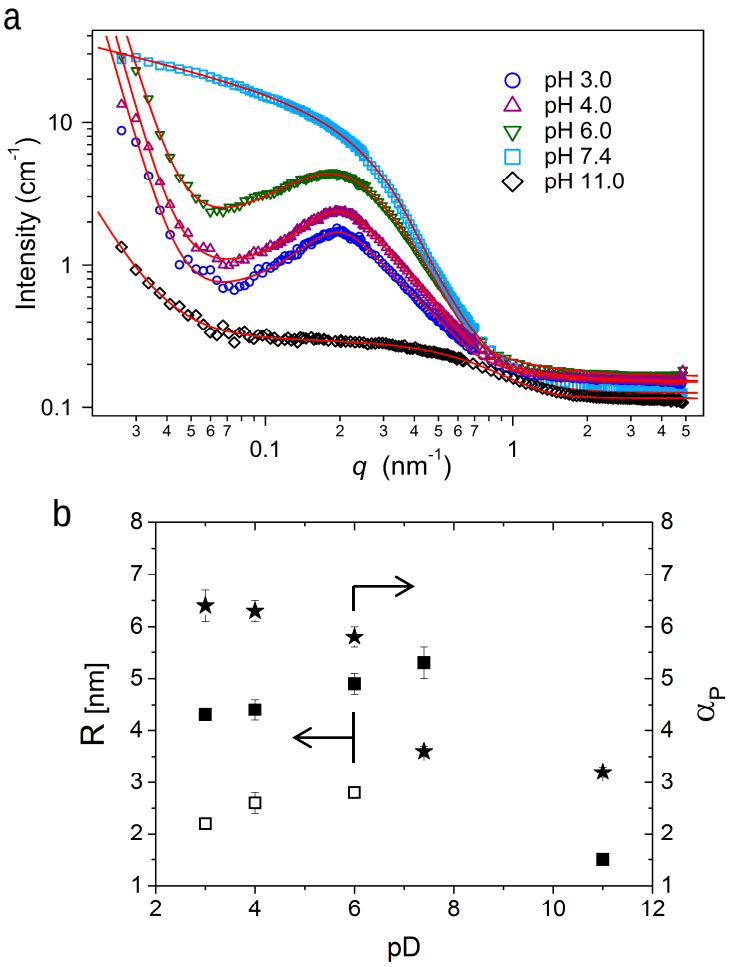

Fig. 6.7: (a) SANS curves of 3 wt% PMMA$_{86}$-*b*-P(DEA$_{190}$-*co*-MAA$_{96}$)-*b*-PMMA$_{86}$ aqueous solutions at 26 °C at different pD values. For better visibility, the curves at pD 3.0, 4.0 and 11.0 were divided by the factor of 1.5, 2.1 and 2.0, respectively. The solid lines represent the model fits. (b) Parameters from fitting of the SANS curves in (a): particle radius, $R_{FS} = R_c + \delta_{surf}$ for pD 3.0, 4.0 and 6.0, R_G for pD 7.4 and R_{sph} for pD 11.0 (solid squares, left axis); core radius R_c for pD 3.0, 4.0 and 6.0 (open squares, left axis); Porod exponent, α_P (stars, right axis). Taken from Ref. 198.

From fitting of the RMSA Coulomb structure factor in Eq. 6.1, the charge of the micelles, *Z*, is found to decrease from 20.1 ± 0.7 at pD 3 to 13.6 ± 0.6 at pD 6.0, which is attributed to the decreasing fraction of ionized DEA units with increasing pD. The continuous charge decrease explains the behavior of the *z*-potential below *iep* (fig. 6.2a). It is worth to note here the big difference between the total large number of ionized units on each polymer chain and the resulting net charge of the micelles, derived from SANS. We assume that the derived values correspond to an effective surface charge on the micelle.

The correlation length, ξ, is found to increase from 13.1 ± 1.4 nm at pD 3.0 to 17.7 ± 1.2 nm at pD 6.0. It corresponds to the average distance between the bridging chains in the network around the charged micelles. With increasing pD, the degree of protonation of PDEA decreases, and so the degree of repulsion along and between the polyampholytic blocks. As a result, the polyampholyte chains at the interface are less stretched away from the micelle, but mainly located in the vicinity of the core. This lowers the extent of cross-linking in the network, which results in a larger average distance between the chains. The strong forward scattering at low *q* values is attributed to the scattering from clusters of micelles. At low pD values (3.0, 4.0 and 6.0), the Porod exponent is determined at an average value $\alpha_P = 6.2 \pm 0.4$. We suppose that the physical network from glassy PMMA domains with the interface from the polyampholytic blocks is additionally stabilized by the repulsion between the charged micelles.

The deduced structure in the low pD region, *i.e.* below the iep, explains the appearance of strong free-standing gels with a maximum zero-shear viscosity and yield stress in this pH range.

Increasing pD to 7.4, which is close to *iep* of the polymer, there is no more evidence of a structure factor peak (fig. 6.7a), instead a shoulder at $q \sim 0.3$ nm^{-1}, associated with the architecture of the micelles. The absence of a structure factor manifests that there is no correlation between the particles, which explains the gel-to-sol transition, accompanied by a significant viscosity drop, observed earlier in rheological studies (figs. 6.4 - 6.6). The scattering curve was fitted using the Guinier-Porod model (Eq. 3.42). The radius of gyration is deduced at $R_G = 5.3 \pm 0.4$ nm with a dimensionality parameter $s = 0.4 \pm 0.1$, which denotes slightly distorted spherical shape of the aggregates. Thus, at pD 7.4, the micelles are non-charged and bigger compared to those at lower pD values. Close to *iep*, the number of oppositely charged DEA and MAA units is nearly equal. The electrostatic attraction between them results in their neutralization, which, in turn, enhances the hydrophobicity of the middle block. As a result, it

merges with the PMMA cores. This fast hydrophobically driven process leads to a non-spherical shape of formed aggregates. The Porod exponent is derived at α_P = 3.7 ± 0.2, which implies rather smooth surface of the aggregates, which is consistent with the concept of collapsed chains.

At pD 11.0, the scattering curve has a very low intensity and features a decay at q > 0.3 nm^{-1} together with a forward scattering at q < 0.1 nm^{-1}. The curve was successfully fitted using Eq. 6.2, which includes the form factor of homogeneous spheres, and a modified Porod law, describing the forward scattering from the large-scale inhomogeneities:

$$I(q) = P_{sph}(q) + P_P(q) + I_{bkg} . \quad (6.2)$$

From fitting Eq. 6.2, the radius of the micelles is found at R_{sph} = 1.5 ± 0.2 nm, which is smaller compared to those at lower pD values. Although the degree of ionization of PMAA is high at this pD, the total number of ionized PMAA segments is not sufficient to stretch the middle block to the extent needed to bridge the micelles, preventing the formation of a 3D network. The Porod exponent is found at α_P = 3.2 ± 0.2 (fig. 6.7b), denoting that the micelles aggregate into bigger clusters.

6.4.2. Structural investigation in dilute solutions

In order to examine the influence of polymer concentration and charge density on the internal structure and the gelation ability of the system, SANS measurements were carried out on PMMA$_{86}$-*b*-P(DEA$_{190}$-*co*-MAA$_{96}$)-*b*-PMMA$_{86}$ aqueous solutions at lower concentration, namely 0.05 wt%. SANS curves at different pD values are presented in figure 6.8a.

The scattering curve at pD 3.0 features a shoulder at q ~ 0.3 nm^{-1}, which could be fitted by the form factor of homogeneous spheres (P_{sph} (q), Eq. 3.43), and a broad maximum at q ~ 0.15 nm^{-1}, which was modelled with a hard-sphere structure factor (S_{HS} (q), Eq. 3.61), manifesting the existence of a 3D network of spherical micelles (microgels):

$$I(q) = P_{sph}(q)S_{HS}(q) + P_P(q) + I_{bkg} \quad (6.3)$$

where $P_P(q)$ is the modified Porod law, which accounts for the scattering at low q values (< 0.1nm^{-1}). The micellar radius is found at R_{sph} = 3.2 ± 0.2 nm, which is similar to the core radius at 3 wt% at the same pD. Presumably the hydrogel consists of spherical micelles, bridged by strongly stretched middle blocks. The existence of finite network already

at this low concentration was confirmed earlier in DLS and TEM studies (fig. 6.3). The distance between the correlated micelles is found at 35.6 ± 1.0 nm. The volume fraction of micelles being part of the network is very low η_{HS} = 0.08 ± 0.04, which is consistent with a low viscosity of the sample at this pD. The derived value of the Porod exponent α_P = 2.5 ± 0.2 manifests that the micelles form loose fractal-like aggregates.

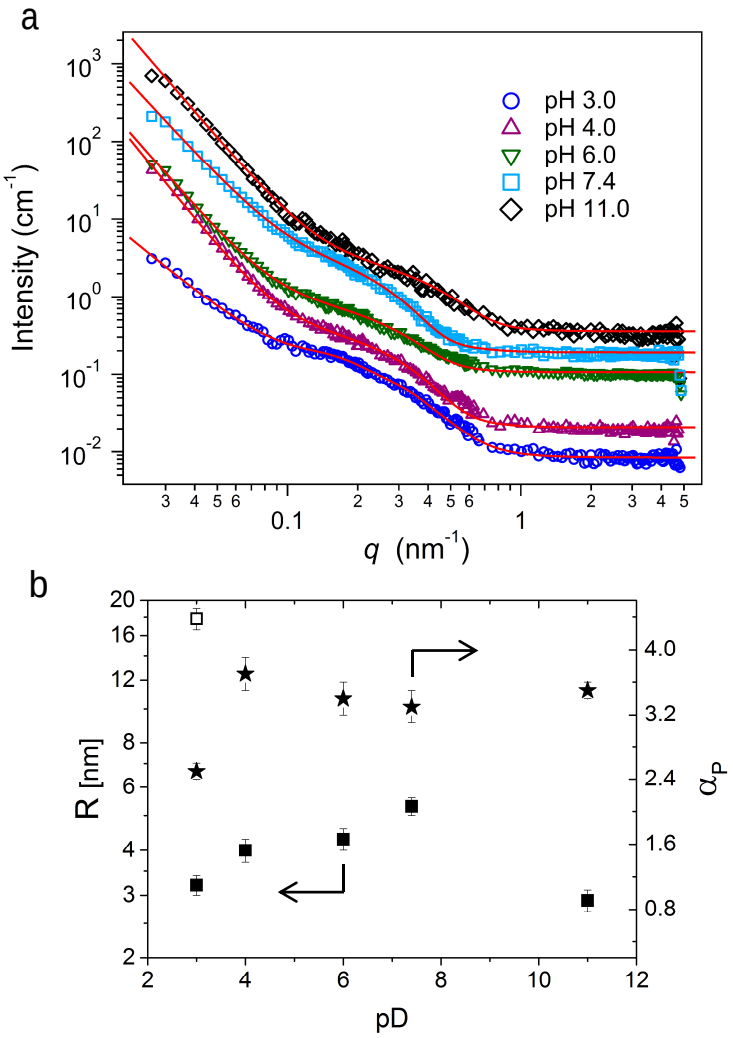

Fig. 6.8: (a) SANS curves of 0.05 wt% PMMA$_{86}$-*b*-P(DEA$_{190}$-*co*-MAA$_{96}$)-*b*-PMMA$_{86}$ aqueous solutions at 26 °C at different pD. For better visibility, the curves are shifted. The solid lines represent the model fits. (b) Parameters from fitting of the SANS curves from (a): sphere radius, R_{sph} (solid squares, left axis); hard-sphere radius, R_{HS} for pD 3.0 (open square, left axis); Porod exponent, α_P (stars, right axis). Taken from Ref. 198.

The scattering curves at all other pD values were fitted using the same model as at pD 3.0 (Eq. 6.3), however, the structure factor was not needed and set to one. Increasing pD in the range below the *iep*, the fraction of ionized DEA units decreases. As a result, the reduced charge density on the middle block leads to its shortening, which restricts its ability to bridge the micelles. The radius of the micelles, R_{sph}, increases from 4.0 ± 0.2 nm at pD 4.0 to 5.3 ± 0.3 nm at pD 7.4, whereas at pD 11.0 it decreases to 2.9 ± 0.4 nm. Upon neutralization of charged segments, the hydrophobicity of micelles increases, provoking their further aggregation, which explains the growth of the aggregate radius. At pD 7.4, close to the *iep*, the hydrophobic effect is even more pronounced due to the mutual neutralization of oppositely charged moieties. Increasing pD to 11.0, the architecture of the micelles repeats the one at pD values below the *iep* with the only difference that now the PMAA moieties are ionized. In contrary to the situation at pD values below the *iep*, the number of ionized MAA units is low (twice lower than the number of ionized DEA units at pD 3.0), which does not allow the middle block to stretch long enough to bridge the micelles. The average value of the Porod exponent (α_P = 3.5 ± 0.3) in the range of pD 4.0 - 11.0 implies the formation of large clusters, presumably from agglomerated micelles.

Therefore, the system demonstrates the same character of structural changes as at higher concentration. Particularly, it was found that with increasing pD, the decrease in ionization degree of the middle polyampholytic block reduces the effective charge on micelles, which is accompanied by a complete loss of the correlation between them. The network disintegrates already at pD 4.0, denoting the system is more sensitive to the variation in charge density.

6.5. Dynamical studies

The present chapter is based on ref. [198].

The hydrogels in the present study represent complex non-ergodic systems. In the previous chapter 5, we have shown that for studies of the dynamical processes in these systems the conventional DLS is not applicable. Thus, it was demonstrated that the long-time scale relaxation processes result in strong oscillations in the intensity autocorrelation curves (fig. 5.8). In order to study dynamics in the present system, it was proposed to use the rotational DLS.

In figure 6.9a, the intensity autocorrelation curves of 3 wt% aqueous solutions of $PMMA_{86}$-*b*-P(DEA_{190}-*co*-MAA_{96})-*b*-$PMMA_{86}$ in D_2O at at different pD values are presented. At pD values 3.0, 4.0 and 6.0, the autocorrelation curves have a similar shape with a relatively fast decay at ca. 1 ms. The second, slower decay (τ > a few ms, the decay was not evaluated quantitatively) is related to the very slow diffusion of large "frozen inhomogeneities", which give rise to the strong forward scattering, observed in SANS (fig. 6.7a). From fitting Eq. 3.79, the relaxation time of the fast decay, τ_{r1}, is deduced to have a non-linear dependence on pD. Thus, it increases from 1.03 at pD 3.0 to 1.37 ms at pD 4.0, reaching its maximum, but it is much lower at pD 7.4, namely 0.89 ms. Therefore, its behavior is consistent with the one of the viscosity (figs. 6.4, 6.5), which has a maximum at pH 4.0, followed by a gradual decrease with increasing pH. At pD 7.4, there is only one strong decay, whereas there is no evidence of the second slower decay. We suppose that the hydrogel consists of large uncorrelated clusters, formed upon hydrophobic aggregation of micelles. In range of pD 3.0 - 7.4, the stretching exponent exhibits pH-independent behavior and has an average value of β_1 = 1.4. In the previous chapter 5, we related this high value to the relaxation of the inner stress. In the present system, it is built due to the presence of the frozen physical constraints inside the network (glassy PMMA cores) and the repulsion between equally charged micelles. This restricts conventional relaxation processes in the system at large length scales, being the origin of a very slow dynamics. At pD 11.0, the curve again shows two decays, but in contrary to the curves at pD below the *iep*, both decays are detected at $\tau \leq 1$ ms. The ultrafast decay is found at τ_{r1} = 2.3×10^{-2} ms with β_1 = 1.05, and is attributed to the diffusion of small unimolecular micelles. The hydrodynamic radius is estimated at R_H = 1.63 nm, which is similar to the micellar radius, detected from SANS fitting at pD 11.0 (R_{sph} = 1.5 ± 0.2 nm, fig. 6.7b).

The second decay is found at τ_{r2} = 1.33 ms (β_2 = 1.01, inset in fig. 6.9a) and is related to the restricted relaxation processes in large clusters from aggregated micelles.

Therefore, we have shown that the relaxation time of the fast decay has a non-linear pD dependence, which is consistent with the rheological behavior and underlying structural changes in the system. Upon increase in pD from 4.0 to 7.4, the network becomes weaker and destabilized due to the reduced charge density in the system.

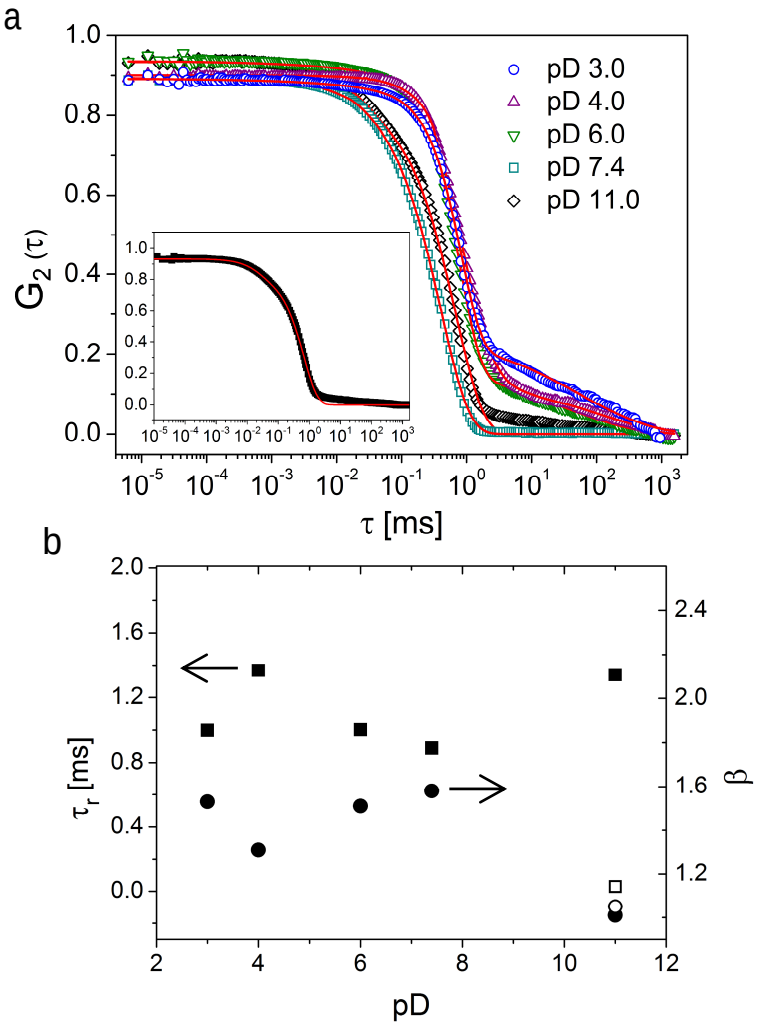

Fig. 6.9: (a) Intensity autocorrelation curves from rotational DLS of 3 wt% $PMMA_{86}$-*b*-$P(DEA_{190}$-*co*-$MAA_{96})$-*b*-$PMMA_{86}$ aqueous solutions at 26 °C at different pD values. The inset shows the curve at pD 11.0. The solid red lines represent the model fits. (b) Parameters from fitting of the DLS curves from (a): relaxation times, τ_r (squares, left axis) and stretching exponents, β (circles, right axis); filled symbols: decay at τ_r ~ 1 ms, open symbols: decay at τ_r ~ 0.02 ms. Taken from Ref. 198.

6.6. Conclusions

In the present chapter we investigated the influence of the charge density on the structure of hydrogels and solutions from a PMMA-*b*-P(DEA-*co*-MAA)-*b*-PMMA triblock terpolymer, using small-angle neutron scattering and rotational dynamic light scattering. In order to examine the influence of concentration, we carried SANS on the same system in dilute solutions. Several regimes were determined.

At 3 wt% in the pD region below the *iep* (i.e. up to pD 6.0), SANS studies revealed the presence of charged fuzzy spheres interacting with each other through a screened Coulomb potential. These fuzzy spheres consist of a core from the hydrophobic PMMA end-blocks with a fuzzy interface from the middle P(DEA-*co*-MAA) blocks. In this pD region, the degree of ionization of PDEA is high, which makes the repulsive electrostatic interactions along the middle polyampholytic block predominant and responsible for the high connectivity in the network. The long relaxation times, derived from rotational DLS, imply that the formed physical hydrogels are frozen. Therefore, the findings from SANS and DLS confirm the existence of free-standing gels with high viscosities in this pH region, detected by rheology. At lower concentration of 0.05 wt%, a loose network of aggregates from micelles is detected.

In the pD region in the vicinity of *iep*, the hydrodynamic radius of aggregates increases, denoting the aggregation of the micelles as a result of their increased hydrophobicity upon neutralization of oppositely charged segments on the middle block. Aggregation is accompanied by a decrease in the effective surface charge of the micelles, followed by a complete loss of the correlation between them at pD 7.4, which explains the gel-to-sol transition and very low viscosity of the sample at this pD.

At pD 11.0, *i.e.* above the *iep*, the uncorrelated homogeneous spherical micelles are present. Low degree of ionization of the middle block and large amount of non-ionized hydrophobic DEA units cause the middle block to shrink, preventing the formation of a 3D network. Rotational DLS indicated the diffusion of small single micelles together with big clusters of micelles.

Therefore, telechelic polymers, comprising a random polyampholytic block, represent strongly pH-responsive systems, which offer the possibility to form hydrogels with tunable properties. The structure of formed self-assembled hydrogels, being the origin of the obtained rheological properties, is sensitive to the charge density on the polyampholytic middle block, controlled by

pH. The final morphology of hydrogels is determined by the interplay between the associative hydrophobic interactions of the PMMA end-groups and the strength of repulsive and/or attractive electrostatic interactions between the charged moieties along the polyampholytic block.

Concluding, the present telechelic polyampholyte represents very promising model system. Its strong pH sensitivity and rich rheological behavior allows to use its aqueous solutions as an injectable hydrogel, *i.e.* for biomedical applications.

7. Summary and conclusion

The present work is devoted to studies of self-assembled hydrogels from stimuli-responsive charged polymers: polyelectrolytes and polyampholytes. Previously, their properties have been shown to have rich pH-dependent rheological behavior, which inevitably raises an interest to these systems as model systems for multiple applications. At the origin of the particular mechanical properties is the conformation of polymer chains in solution, which is defined by the combination of attractive and/or repulsive electrostatic interactions between charged groups and hydrophobic associations of non-ionized groups. In polyampholytes, the extent of electrostatic interactions is defined by charge asymmetry and charge density. The latter ones can be affected by several parameters. In present work we investigated the influence of pH and ionic strength on the associative character of several types of polyampholytes and the resulting nanostructure of the hydrogels.

The first part was devoted to studies of the effect of charge asymmetry on the conformational properties of the quaternized polyampholyte PAA-*b*-QP2VP-*b*-PAA. SANS on quasi-dilute solutions enabled us to detect a progressive transformation of the structure with increasing charge imbalance. Moving from pH 7.0 to 3.0, the system undergoes the transition from uncorrelated dense microgels via the fractal clusters from micelles to a 3D network. The latter is formed at a minimum charge molar ratio, $[AA^-]/[2VPR^+]$, of ca. 6% (highest charge asymmetry), manifesting the electrostatic interactions is the main driving force for gelation. The network formation becomes possible due to the combination of both: attractive electrostatic interactions among the oppositely charged moieties of the different blocks, and repulsive – between the equally charged units on the middle block. Thus, extended attractive interactions lead to the formation of interpolyelectrolyte complexes, which act as physical cross-links in the network. In contrast, the repulsive interactions are responsible for the stretching of the QP2VP blocks, providing the network connectivity. The transition from uncorrelated microgels to a 3D network decreasing pH was correlated with the sol-to-gel transition, observed in previous rheological studies.

Further, with the aim to explain the origin of large differences in mechanical behavior of hydrogels from this kind of systems, we studied the network properties in hydrogels from the

nonquaternized precursor PAA-*b*-P2VP-*b*-PAA and the telechelic polyelectrolyte P*t*BA-*b*-P2VP-*b*-P*t*BA, from which both polyampholytes are derived. Systems were studied at the pH of maximum viscosity, namely 3.0. SANS revealed that the hydrogels in all cases consist of micelles, bridged by stretched QP2VP/P2VP blocks. The strong correlation between the network architecture and the gelation properties of three systems was deduced. Thus, it was shown that the higher the effective length of the bridging chains, the lower is the percolation threshold, and the higher are the viscosity and elasticity of gels, so η_o (telechelic polyelectrolyte) > η_o (nonquaternized polyampholyte) > η_o (quaternized polyampholyte). Free-standing gels from the nonquaternized polyampholyte are due to higher stability of bridging chains, carrying high number of non-ionized hydrophobic 2VP units. Kinetically "frozen" networks with high viscosity and elasticity from the telechelic polyelectrolyte are the result of enhanced stability of both: bridging P2VP chains and "frozen" physical cross-links from the P*t*BA blocks. In contrary, softer gel with lower viscosity from the quaternized polyampholyte is the result of enhanced mobility of strongly ionized QP2VP blocks, which restricts their ability to act as bridging chains.

In the second part, we focused on the influence of ionic strength on the structural properties of hydrogels from similar kind of triblock polyampholytes PAA-*b*-P2VP-*b*-PAA at pH 3. With the aim to study the influence of charge density, the SANS studies were accordingly accomplished on the quaternized counterpart PAA-*b*-PQ2VP-*b*-PAA at pH 5, which has higher degrees of ionization of both blocks. SANS on the salt-free solutions detected a 3D network, similar to the one from the polyampholyte systems, studied in the first part of the work: micelles from interpolyelectrolyte complexes of oppositely charged QP2VP/P2VP and PAA chains, connected by stretched PQ2VP/P2VP middle blocks. After addition of NaCl we observe a different response of the two systems and attribute it to the different nature of the predominant interactions in each case, namely electrostatic or hydrophobic. Thus, it was found that in PAA-*b*-PQ2VP-*b*-PAA, which has a high charge density, a variation in ionic strength leads to strong changes in the network architecture, explaining softening of gels, detected previously. Thus, salt addition leads to increase in the radius of complexes and the distance between them, which is due to the increased hydrophobicity in the system upon screening of charges. In contrast, in PAA-*b*-P2VP-*b*-PAA at pH 3, which features lower degrees of ionization of both blocks and the presence of hydrophobic units along the P2VP chains, the architecture of the

network is less sensitive to changes in ionic strength, which is at the origin of mechanical stiffness of gel up to higher salt concentrations. Rotational dynamic light scattering DLS studies in this system supported the hypothesis, arisen from SANS and rheology, that the formed hydrogels are stable over the entire studied NaCl concentration range.

Thirdly, we investigated the influence of charge density on the structure of pH-responsive hydrogels from the telechelic polyampholyte PMMA-*b*-P(DEA-*co*-MAA)-*b*-PMMA with a random polyampholytic middle block, at different pH values in dilute and semi-dilute regime. The interest to the present system was raised by its different self-assembly mechanism due to the presence of the hydrophobic end-blocks along with the polyampholytic block.

SANS indicated several structural transitions with increasing pH, explaining the transition from a rigid gel to aqueous solutions, detected earlier in rheological studies. We observed the strong correlation between the degree of ionization of the middle block and the structure of the hydrogel, being at the origin of the particular mechanical properties. In pH range below the *iep* region, a 3D network from charged fuzzy spheres, interacting with each other via a screened Coulomb potential, is formed. The connectivity in the network was correlated with the high degree of ionization of the middle blocks, allowing them to adopt an extended conformation and bridge different micelles. Rotational DLS confirmed that the formed physical hydrogels are frozen. These findings come in agreement with the formation of free-standing hydrogels with maximum viscosity in this pH region. At pH 7.4, close to *iep* region, SANS revealed the existence of uncorrelated micelles, which explains the abrupt gel-to-sol transition at this pH. This happens upon vanishing of the electrostatic effect upon neutralization of both ionized PDEA and PMAA segments. In pH range above the *iep* region, only single micelles are present. Low degree of ionization of the middle block provokes its merging with the hydrophobic core, prohibiting the network formation. Rotational DLS allowed us to separate the diffusion of single micelles from the one of bigger clusters from aggregated micelles. The morphology of the system at lower concentration is found to be more sensitive to pH variation. Therefore, we were able to bind the final mechanical properties of the system to the corresponding changes in the nanostructure of formed hydrogels, which is pH and concentration dependent.

Concluding, we were able to demonstrate the strong influence of the molecular characteristics, charge asymmetry and charge density of the polyampholyte on its associative behavior and properties of formed hydrogels, namely morphological and dynamical.

Bibliography

[1] C. A. Costello, G. F. Matz, N. S. Sherwood, B. P. Boffardi, M. A. Yorke, and Z. Amjad. EU Patent 0156031, 1987.

[2] C. S. Patrickios, L. R. Sharma, S. P. Armes, and N. C. Billingham. *Langmuir*, 15:1613-1620, 1999.

[3] X. Xi, Y. Liu, J. Shi, and S. Cao. *J. Mol. Catal. A*, 192:1-7, 2003.

[4] Z. E. Ibraeva, M. Hahn, W. Jaeger, L. A. Bimendina, S. E. Kudaibergenov. *Macromol. Chem. Phys.*, 205:2464-2472, 2004.

[5] T. K. Georgiou and C. S. Patrickios. *Biomacromolecules*, 9:574-582, 2008.

[6] S. Chen and S. Jiang. *Adv. Mater.*, 20:335-338, 2008.

[7] C. Yoshihara, C.-Y. Shew, T. Ito, Y. Koyama. *Biophys. J.*, 98:1257-1266, 2010.

[8] Z. Iatridi, G. Mattheolabakis, K. Avgoustakis, and C. Tsitsilianis. *Soft Matter*, 7:11160-11168, 2011.

[9] X.-F. Sun, Z. Jing, G. Wang. *J. Appl. Polym. Sci.*, 128:1861-1870, 2013.

[10] J. van der Gucht, E. Spruijt, M. Lemmers, and M. A. Cohen Stuart. *J. Colloid Interface Sci.*, 361:407-422, 2011.

[11] D. V. Pergushov, A. H. Müller, and F. H. Schacher. *Chem. Soc. Rev.*, 41:6888-6901, 2012.

[12] I. Tanaka, S. T. Nishio, S. Sun, and S. Ueno-Nishio. *Science*, 218:467-469, 1982.

[13] Y. Osada and P. Gong. *Polymer Gels and Networks.* New York: Marcel Dekker, 2002.

[14] A. S. Krishnan, S. Seifert, B. Lee, S. A. Khan, and R. J. Spontak. *Soft Matter*, 6:4331-4334, 2010.

[15] F. Lai and H. Li. *Mech. Mater.*, 43:287-298, 2011.

[16] K. J. Henderson and K. R. Shull. *Macromolecules*, 45:1631-1635, 2012.

[17] S. Sircar, J. P. Keener, and A. L. Fogelson. *J. Chem. Phys.*, 138:014901, 2013.

[18] A. D. Drozdov and C. J. deClaville. *J. Chem. Phys.*, 142:114904, 2015.

[19] F. A. Blyakhman, A. P. Safronov, T. F. Shklyar, and M. A. Filipovich. *Sens. Actuat. A*, 229:104-109, 2015.

[20] A. Richter, D. Kuckling, K.-F. Arndt, T. Gehring, and S. J. Howitz. *Microelectromech. Syst.*,12:748-753, 2003.

[21] G. Gerlach, M. Guenther, J. Sorber, G. Suchaneck, K.-F. Arndt, A. Richter. *Sens. Actuat. B*, 111-112:555-561, 2005.

[22] E. Fernandez, D. Lopez, E. Lopez-Cabarcos, and C. Mijangos. *Polymer*, 46:2211-2217, 2005.

[23] M. Guenther, G. Gerlach, C. Corten, D. Kuckling, M. Müller, Z. Shi, J. Sorber, K.-F. Arndt. *Macromol. Symp.*, 254:314-321, 2007.

[24] L. Dong, A. K. Agarwal, D. J. Beebe, and H. Jiang. *Nature*, 442:551-554, 2006.

[25] L. Tokarev, S. Minko. *Advanced Materials*, 22:3446-3462, 2010.

[26] T. Miyata, T. Uragami, K. Nakamae. *Adv. Drug Deliv. Rev.*, 54*:*79-98, 2002.

[27] N. E. Fedorovich, J. Alblas, J. R. de Wijn, W. E. Hennink, A. J. Verbout, and W. J. A. Dhert. *Tissue Eng.*, 13:1905-1925, *2007.*

[28] H. J. Kwon. *Advances in Materials Science and Engineering*, 2014, Article ID 154071.

[29] N. Rahimi, G. Swennen, S. Verbruggen, M. Scibiorek, D. G. Molin, and M. J. Post. *Tissue Eng. C*, 20:703-713, 2014.

[30] C. Tanford. *Physical Chemistry of Macromolecules.* New York: Wiley, 1961.

[31] F. Oosawa. *Polyelectrolytes.* New York: Marcel Dekker, 1971.

[32] M. Madel. *Polyelectrolytes* in Encyclopedia of Polymer Science and Engineering. New York: Wiley-Interscience, 1986.

[33] J. L. Barrat and J. F. Joanny. *Chem. Phys.*, 94:1-66, 1996.

[34] T. Radeva. *Physical Chemistry of Polyelectrolytes*. New York: Marcel Dekker, 2001.

[35] Wikipedia homepage, visited on 19.08.2015. URL https://en.wikipedia.org/wiki/Polyelectrolyte.

[36] E. A. Bekturov, S. E. Kudaibergenov, and S. R. Rafikov. *J. Macromol. Sci., Rev. Macromol. Chem. Phys.*, C30:233-303, 1990.

[37] S. E. Kudaibergenov. *Adv. Polym. Sci.*, 144:115-197, 1999.

[38] P. G. de Gennes. *Scaling concepts in polymer physics.* Ithaca, New York: Cornell University Press, 1979.

[39] M. Doi and S. F. Edwards. *The theory of polymer dynamics.* Oxford: Clarendon Press, 1989.

[40] M. Rubinstein and R. H. Colby. *Polymer physics*. New York: Oxford University Press, 2003.

[41] A. V. Dobrynin and M. Rubinstein. *Prog. Polym. Sci.*, 30:1049-1118, 2005.

[42] R. R. Netz and D. Andelman. *Polyelectrolytes in Solution and at Surfaces* in Encyclopedia of Electrochemistry. New York: Wiley, 2007.

[43] R. M. Fuoss. *J. Polym. Sci.*, 3:603-604, 1948.

[44] D. Andelman. *Electrostatic Properties of Membranes: The Poisson–Boltzmann Theory* in Handbook of Biological Physics, ed. by R. Lipowsky and E. Sackmann. Amsterdam: Elsevier, 1995.

[45] T. Zito. Grand Canonical Monte Carlo Simulation of Polymer Chains with a Fluctuating Charge Distribution (Annealed Polyelectrolytes). Theoretical Physics diploma thesis, Bologna University, 2001.

[46] H. Ohshima. *Theory of Colloid and Interfacial Electric Phenomena* in Interface Science and Technology, ed. by A. Hubbard. Amsterdam: Elsevier, 2006.

[47] P. Debye and E. Hückel. *Phys. Z.*, 24:185-206, 1923.

[48] A. V. Dobrynin, R. H. Colby, and M. Rubinstein. *J. Polym. Sci. B*, 42:3513-3538, 2004.

[49] W. Kuhn, O. Künzle, and A. Katchalsky. *Helv. Chim. Acta*, 31:1994-2037, 1948.

[50] A. V. Dobrynin, R. H. Colby, and M. Rubinstein. *Macromolecules*, 28:1859-1871, 1995.

[51] Q. Liao, A. V. Dobrynin, and M. Rubinstein. *Macromolecules*, 36:3386-3398, 2003.

[52] Y. Kantor and M. Kardar. *Phys. Rev. E*, 51:1299-1312, 1995.

[53] F. J. Solis and M. O. de la Cruz. *Macromolecules*, 31:5502-5506, 1998.

[54] H. Schiessel. *Macromolecules*, 32:5673-5680, 1999.

[55] U. Micka and K. Kremer. *Europhys.Lett.*, 49:189-195, 2000.

[56] G. T. Pickett and A. Balazs. *Langmuir*, 17:5111-5117, 2001.

[57] A. V. Dobrynin and M. Rubinstein. *Macromolecules*, 34:1964-1972, 2001.

[58] H. Limbach, C. Holm, and K. Kremer. *Europhys.Lett.*, 60:566-572, 2002.

[59] Holm, H. J. Limbach, and K. J. Kremer. *Phys.: Condens. Matter*, 15:S205-S211, 2003.

[60] H. J. Limbach and C. Holm. *J. Phys. Chem. B*, 107: 8041-8055, 2003.

[61] A. V. Dobrynin, M. Rubinstein, and S. P. Solis. *Macromolecules*, 29:2974-2979, 1996.

[62] U. Micka, C. Holm, and K. Kremer. *Langmuir*, 15:4033-4044, 1999.

[63] A. Y. Grosberg, A. R. Khokhlov. *Statistical Physics of Macromolecules*. New York: AIP Press, 1994.

[64] L. Rayleigh. *Philos. Mag.*, 14:184-186, 1882.

[65] A. V. Dobrynin, M. Rubinstein, and S. P. Obukhov. *Macromolecules*, 29:2974-2979, 1996.

[66] G. S. Manning. *J. Chem. Phys.*, 51:954, 1969.

[67] N. Th. M. Klooster, F. van der Touw, and M. Mandel. *Macromolecules*, 17:2070-2078, 1984.

[68] S. G. Starodoubtsev, A. R. Khokhlov, E. L. Sokolov, and B. Chu. *Macromolecules*, 28:3930-3936, 1995.

[69] R. G. Winkler, M. Gold, and P. Reineker. *Phys. Rev. Lett.*, 80:3731-3734, 1998.

[70] T. Odijk. *J. Polym. Phys. B*, 15:477-483, 1977.

[71] J. Skolnick and M. Fixman. *Macromolecules*, 10:944-948, 1977.

[72] A. Katchalsky, Z. Alexandrowicz, O. Kedem. *Polyelectrolyte solutions* in Chemical Physics of Ionic Solutions, ed. by B. E. Conway and R. G. Barradas. London: Wiley, 1966.

[73] P. Pfeuty. *J. Phys. Coll. C2,* 39:149-160, 1978.

[74] F. Bordi, R. H. Colby, C. Cametti, L. De Lorenzo, and T. Gili. *J. Phys. Chem. B,* 106:6887-6893, 2002.

[75] M. J. Lee, M. M. Green, F. Mikes, and H. Morawetz. *Macromolecules,* 35:4216-4217, 2002.

[76] S. Minko, A. Kiriy, G. Gorodyska, and M. Stamm. *J. Am. Chem. Soc*., 124:3218-3219, 2002.

[77] M. N. Spiteri, F. Boue, A. Lapp, and J. P. Cotton. *Physica B,* 234:303-305, 1997.

[78] T. A. Waigh, R. Ober, C. E. Williams, and J. C. Galin. *Macromolecules,* 34:1973-1980, 2001.

[79] D. Qu, D. Baig, C. E. Williams, H. Mohwald, A. Fery. *Macromolecules,* 36:6878-6883, 2003.

[80] Dobrynin's group homepage, visited on 03.04.2014. URL http://faculty.ims.uconn.edu/~avd/.

[81] E. N. Danilovtseva, V. V. Annenkov, and A. I. Mikhaleva. *Polym. Sci. Ser. A,* 46:125-129, 2004.

[82] J. T. Huang, J. Zhang, J. Q. Zhang, and S. H. Zheng. *J. Appl. Polym. Sci.*, 95:358-361, 2005.

[83] J. G. Noh, Y. J. Sung, K. E. Geckeler, and S. E. Kudaibergenov. *Polymer*, 46:2183-2190, 2005.

[84] C. Note, J. Koetz, L. Wattebled, A. Laschewsky. *J. Colloid Interface Sci.*, 308:162-169, 2007.

[85] M. E. Schroeder, K. M. Zurick, D. E. McGrath, and M. T. Bernards. *Biomacromolecules*, 14:3112-3122, 2013.

[86] R. K. Mishra, K. Ramasamy, N. N. Ban, and A. B. Majeed. *J. Appl. Polym. Sci.*, 128:3365-3374, 2013.

[87] G. Ehrlich and P. Doty. *J. Am. Chem. Soc.*, 76:3764-3777, 1954.

[88] T. Alfrey and S. H. Pinner. *J. Polym. Sci.*, 23:533-547, 1957.

[89] C. L. McCormick and C. B. Johnson. *Macromolecules*, 21:694-699, 1988.

[90] K. S. Pafiti, Z. Philippou, E. Loizou, L. Porcar, C. S. Patrickios. *Macromolecules*, 44:5352-5362, 2011.

[91] Y. Morishima, T. Hashimoto, Y. Itoh, M. Kamachi, S. I. Nozakura. *J. Polym. Sci., Polym. Chem.*, 20:299-310, 1982.

[92] A. B. Lowe, N. C. Billingham, S. P. Armes. *Macromolecules*, 31:5991-5998, 1998.

[93] G. Gotzamanis and C. Tsitsilianis. *Macromol. Rapid Commun.*, 27:1757-1763, 2006.

[94] K. M. Zurick and M. Bernards. *J. Appl. Polym. Sci.*, 131:40069:1-40069:9, 2014.

[95] D. Kuckling, C. D. Vo, and S. E. Wohlrab. *Langmuir*, 18:4263-4269, 2002.

[96] T. Hoare and R. Pelton. *Macromolecules*, 37:2544-2550, 2004.

[97] W. Agut, A. Brulet, C. Schatz, D. Taton, and S. Lecommandoux. *Langmuir*, 26:10546-10554, 2010.

[98] I. Ohmine and T. Tanaka. *J. Chem. Phys.*, 11:5725-5729, 1982.

[99] R. A. Siegel and B. A. Firestone. *Macromolecules*, 21:3254-3259, 1988.

[100] J. Kotz, M. Hahn, B. Philipp. *Makromol. Chem.*, 194:397-410, 1993.

[101] C. S. Patrickios, W. R. Hertler, T. A. Hatton. *Fluid Phase Equilibria*, 108:243-254, 1995.

[102] J. I. Amalvy, E. J. Wanless, Y. Li., V. Michailidou, S. P. Armes, and Y. Duccini. *Langmuir*, 20:8992-8999, 2004.

[103] R. G. Ezell, I. Gorman, B. Lokitz, N. Ayres, C. L. McCormick. *J. Polym. Sci., Part A: Polym. Chem.*, 44:3125-3139, 2006.

[104] B. H. Tan, P. Ravi, L. N. Tan, and K. C. Tam. *J. Colloid Interface Sci.*, 309:453-463, 2007.

[105] R. Kodiyath, I. Choi, B. Patterson, C. Tsitsilianis, and V. V. Tsukruk. *Polymer*, 54:1150-1159, 2013.

[106] J. Ricka and T. Tanaka. *Macromolecules*, 18:83-85, 1985.

[107] A. G. Didukh, R. B. Koizhaiganova, G. Khamitzhanova, L. A. Bimendina, and S. E. Kudaibergenov. *Polym.Int.*, 52:883-891, 2003.

[108] B. H. Tan, K. C. Tam, Y. C. Lam, C. B. Tan. *Langmuir*, 20:11380-11386, 2004.

[109] K. S. Schmitz. *Macroions in Solution and Colloidal Suspension*. New York: VCH Publishers, 1993.

[110] Y. Kantor and M. Kardar. *Europhys. Lett.*, 27:643-648, 1994.

[111] S. Forster and M. Schmidt. *AdvPolym Sci.*, 120:51-133, 1995.

[112] P. G. Higgs and J. F. Joanny. *J. Chem. Phys.*, 94:1543-1554, 1991.

[113] J. C. Salamone, L. Quach, A. C. Watterson, S. Krauser, M. U. Mahmud. *J. Macromol. Sci.*, 22:653-664, 1985.

[114] C. L. McCormick and C. B. Johnson. *Macromolecules*, 21:686-693, 1988.

[115] C. Qian and A. L. Kholodenko. *J. Chem. Phys.*, 89:5273-5279, 1988.

[116] M. Tanaka, A. Y. Grosberg, V. S. Pande, and T. Tanaka, T. *Phys. Rev.*, 56:5798-5808, 1997.

[117] N. P. Shusharina and M. Rubinstein. *Scaling Theory of Polyelectrolyte and Polyampholyte Micelles* in Nanostructured Soft Matter: Experiment, Theory, Simulation and Prospectives. Series: NanoScience and Technology, ed. by A.V. Zvelindovski. Springer, 2007.

[118] N. P. Shusharina, E. B. Zhulina, A. V. Dobrynin, M. Rubinstein. *Macromolecules*, 38:8870-8881, 2005.

[119] J. Jeon and A. V. Dobrynin. *J. Phys. Chem. B*, 110:24652-24665, 2006.

[120] C. Chassenieux, T. Nicolai, and D. Durand. *Macromolecules*, 30:4952-4958, 1997.

[121] A. B. Lowe and C. L. McCormick. *Chem. Rev.*, 102:4177-4189, 2002.

[122] V. Sfika and C. Tsitsilianis. *Macromolecules*, 36:4983-4988, 2003.

[123] M. Lemmers, J. Sprakel, I. K. Voets, J. van der Gucht, and M. A. Cohen Stuart. *Angew. Chem. Int. Ed.*, 49:708-711, 2010.

[124] J. van der Gucht, E. Spruijt, M. Lemmers, and M. A. Cohen Stuart. *J. Colloid Interface Sci.*, 361:407-422, 2011.

[125] D. G. Peiffer and R. D. Lundberg. *Polymer*, 26:1058-1068, 1985.

[126] A. Ohlemacher, F. Candau, J. P. Munch, and S. J. Candau. *J. Polym. Sci.*, 34:2747-2757, 1996.

[127] A. E. English, S. Mafe, J. A. Manzanares, X. Yu, A. Y. Grosberg, and T. Tanaka. *J. Chem. Phys*., 104:8713-8720, 1996.

[128] M. Tanaka and T. Tanaka. *Phys. Rev. E*, 62:3803-3816, 2000.

[129] G. Nisato, J. P. Munch, and S. J. Candau. *Langmuir*, 15:4236-4244, 1999.

[130] P. Kujawa, F. Segui, S. Shaban, C. Diab, Y. Okada, F. Tanaka, F. M. Winnik. *Macromolecules*, 39:341-348, 2006.

[131] A. Nykänen, M. Nuopponen, A. Laukkanen, S.-P. Hirvonen, M. Rytelä, O. Turunen, H. Tenhu, R. Mezzenga, O. Ikkala and J. Ruokolainen. *Macromolecules*, 40:5827-5834, 2007.

[132] T. Koga, F. Tanaka, R. Motokawa, S. Koizumi, F. M. Winnik. *Macromolecules*, 41:9413-9422, 2008.

[133] W. Richtering and A. Pich. *Soft Matter*, 8:11423-11430, 2012.

[134] A. Laschewsky, P. Müller-Buschbaum, C. M. Papadakis. *Progr. Colloid Polym. Sci.*, 140:15-34, 2013.

[135] A. S. Kimerling, W. E. Rochefort, S. R. Bhatia. *Eng. Chem. Res*., 45:6885-6889, 2006.

[136] F. Bossard, T. Aubry, G. Gotzamanis, C. Tsitsilianis. *Soft Matter*, 2:510-516, 2006.

[137] C. Tsitsilianis, N. Stavrouli, V. Bocharova, S. Angelopoulos, A. Kiriy, I. Katsampas, M. Stamm. *Polymer*, 49:2996-3006, 2008.

[138] C. Tsitsilianis, T. Aubry, I. Iliopoulos, S. Norvez. *Macromolecules*, 43:7779-7784, 2010.

[139] N. Stavrouli, J. Katsampas, S. Angelopoulos, C. Tsitsilianis. *Macromol. Rapid Commun.*, 29:130-135, 2008.

[140] C. Tsitsilianis, G. Gotzamanis, Z. Iatridi. *Eur.Polym. J.*, 47:497-510, 2011.

[141] S. Li, Y. Wu, J. Wang, Q. Zhang, Y. Kou, S. Zhang. *J. Mater. Chem*., 20:4379-4384, 2010.

[142] S. Soll, Q. Zhao, J. Weber, J. Yuan. *Chem. Mater.*, 25:3003-3010, 2013.

[143] Z. Iatridi and C. Tsitsilianis. *Chem. Commun*., 47:5560-5562, 2011.

[144] H. Feil, Y. H. Bae, J. Feijen, S. W. Kim. *Macromolecules*, 25:5528-5530, 1992.

[145] V. Bulmus, Z. Ding, C. J. Long, P. S. Stayton, A. S. Hoffman. *Bioconjugate Chem*., 11:78-83, 2000.

[146] R. B. Bird, R. C. Armstrong, O. Hassager. *Fluid Mechanics in Dynamics of Polymeric Liquids.* New York: Wiley, 1987.

[147] S. A. Khan, J. R. Royer, and S. R. Raghavan. *Rheology: Tools and Methods* in Aviation Fuels with Improved Fire Safety: A *proceeding.* Washington DC: Nat. Acad. Press, 1997.

[148] C. W. Macosko. *Rheology: Principles, Measurements and Applications.* New York: Wiley, 1994.

[149] I. W. Hamley. *Introduction to Soft Matter - Revised Edition: Synthetic and Biological Self-Assembling Materials*. Chichester: Wiley, 2007.

[150] D. T. N. Chen, Q. Wen, P. A. Janmey, J. C. Crocker, and A. G. Yodh. *Annu. Rev. Condens. Matter Phys.*, 1:301-322, 2010.

[151] C. Riedel, A. Alegria, J. Colmenero, and P. Tordjeman. *Polymer Rheology by Dielectric Spectroscopy* in Rheology, ed. by Dr. J. De Vicente. InTech, 2012.

[152] Homepage of Experimental Soft Condensed Matter group, visited on 10.06.2015. D. Vader and H. Wyss. *Introduction to Rheology*. URL http://weitzlab.seas.harvard.edu/.

[153] Homepage for CM4650 Polymer Rheology laboratory, visited on 16.09.2015. URL http://www.chem.mtu.edu/~fmorriso/cm4655/cm4655.html.

[154] H. A. Barnes. *A handbook of Elementary Rheology*. Aberystwyth: Cambrian printers, 2000.

[155] Homepage Malvern, visited on 9.10.2015. URL www.malvern.com.

[156] R.-J. Roe. *Methods of X-Ray and Neutron Scattering in Polymer Science*. New York: Oxford University Press, 2000.

[157] O. Spalla. *General theorems in Small-angle scattering* in Neutrons, X-rays and Light: Scattering Methods Applied to Soft Condensed Matter, ed. by P. Lindner, Th. Zemb. Amsterdam: Elsevier, 2002.

[158] A. J. Jackson. Introduction to Small-Angle Neutron Scattering and Neutron Reflectometry. NIST Center for Neutron Research, May 2008.

[159] D. S. Silvia. Elementary Scattering Theory: For X-ray and Neutron Users. New York: Oxford University Press Inc., 2011.

[160] R. Pynn. *Los Alamos Science*, 19:1-31, 1990.

[161] P. Lindner. *Scattering Experiments: Experimental Aspects, Initial Data Reduction and Absolute Calibration* in Neutrons, X-rays and Light: Scattering Methods Applied to Soft Condensed Matter, ed. by P. Lindner, Th. Zemb. Amsterdam: Elsevier, 2002.

[162] G. L. Squires. Introduction to Thermal Neutron Scattering. Cambridge: Cambridge University Press, 1978.

[163] I. Grillo. *Small-Angle Neutron Scattering and Applications in Soft Condensed Matter* in Soft-Matter Characterization, ed. by R. Borsali and R. Pecora. Springer, 2008.

[164] A. Radulescu, V. Pipich, H. Frielinghaus, and M.-S. Appavou. *J. Phys.: Conf. Series* 351:012026:1-012026:13, 2012.

[165] A. V. Feoktystov, H. Frielinghaus, Z. Di, S. Jaksch, V. Pipich, M.-S. Appavou, E. Babcock, R. Hanslik, R. Engels, G. Kemmerling, H. Kleines, A. Ioffe, D. Richter, and T. Brückel. *J. Appl. Cryst.*, 48:61-70, 2015.

[166] Homepage Heinz Maier-Leibnitz Zentrum, visited on 10.09.2015. URL http://www.mlz-garching.de/kws-1.

[167] B. Hammouda. *J. Appl. Cryst.*, 43:716-719, 2010.

[168] P. Bartlett and R. H. Ottewill. *J. Chem. Phys*., 96:3306-3318, 1992.

[169] J. Adelsberger. Struktur und Kineticthermoresponsiver Hydrogele. PhD thesis, Physics Department, TU München, 2012.

[170] M. Stieger, J. S. Pedersen, P. Lindner, and W. Richtering. *Langmuir*, 20:7283-7292, 2004.

[171] L. S. Ornstein and F. Zernike. *Phys. Z.*, 19:134-137, 1918.

[172] J. K. Percus and G. J. Yevick. *Phys. Rev*., 110:1-13, 1958.

[173] J. P. Hansen and I. R. McDonald. *Theory of Simple Liquids*. London: Academic Press, 1986.

[174] J. B. Hayter and J. Penfold. *Mol. Phys.*, 42:109-118, 1981.

[175] J. P. Hansen and J. B. Hayter. *Mol. Phys.*, 46:651-656, 1982.

[176] E. J. W. Verwey and J. Th. G. Overbeek. *Theory of the Stability of Lyophobic Colloids.* Amsterdam: Elsevier, 1948.

[177] J. Teixeira. *Appl. Cryst.*, 21:781-785, 1988.

[178] M. Shibayama and T. Tanaka. *J. Chem. Phys.*, 97:6829-6841, 1992.

[179] C. S. Johnson, Jr. and D. A. Gabriel. *Laser Light Scattering*. New York: Dover Publications, 1994.

[180] L. Øgendal. *Light Scattering demystified. Theory and Practice*. (visited on 1.08.2015) URL http://igm.fys.ku.dk/~lho/personal/lho/lightscattering_theory_and_practice.pdf.

[181] B. J. Berne and R. Pecora. *Dynamic Light scattering*. New York: Wiley, 1975.

[182] W. Burchard. *Static and Dynamic Scattering Approaches to Structure Determination of Biopolymers* in Laser Light Scattering in Biochemistry, ed. by S. E. Harding, D. B. Sattelle and V. A. Bloomfield. Royal Society of Chemistry, Cambridge, 1992.

[183] J. Jakes. *Czech. J. Phys*., B38:1305-1316, 1988.

[184] P. Štěpánek. *Data Analysis in Dynamic Light Scattering* in Dynamic Light Scattering. The Method and Some Applications, ed.by W. Brown. Clarendon Press: Oxford, 1993.

[185] J.-Z. Xue, D. J. Pine, S. T. Milner, X.-I. Wu, P. M. Chaikin. *Phys. Rev. A*, 46:6550-6563, 1992.

[186] P. N. Pusey. Dynamic Light Scattering.in Neutrons, X-rays and Light: Scattering Methods Applied to Soft Condensed Matter, ed. by P. Lindner, Th. Zemb. Amsterdam: Elsevier, 2002.

[187] O. Colombani, E. Lejeune, C. Charbonneau, C. Chassenieux, T. Nikolai. *J. Phys. Chem. B*, 116:7560-7565, 2012.

[188] N. Stavrouli. PhD thesis. University of Patras, Greece, 2006.

[189] E. A. Boucher, C. C. Mollet. *J. Chem. Soc. Faraday Trans.*, 78:75-88, 1982.

[190] N. Stavrouli, Z. Iatridi, T. Aubry, and C. Tsitsilianis. *Polym. Chem*., 4:2097-2105, 2013.

[191] M. A. Dyakonova, N. Stavrouli, M. T. Popescu, K. Kyriakos, I. Grillo, M. Philipp, S. Jaksch, C. Tsitsilianis, C. M. Papadakis. *Macromolecules*, 47:7561-7572, 2014.

[192] N. Stavrouli, T. Aubry, C. Tsitsilianis. *Polymer*, 49:1249-1256, 2008.

[193] M. A. Dyakonova, A. V. Berezkin, K. Kyriakos, S. Gkermpoura, M. T. Popescu, S. K. Filippov, P. Štěpánek, Z. Di, C. Tsitsilianis, and C. M. Papadakis. *Macromolecules*, 48:8177-8189, 2015.

[194] R. Bandyopadhyay, D. Liang, H. Yardimci, D. A. Sessoms, M. A. Borthwick, S. G. J. Mochrie, J. L. Harden, R. L. Leheny. *Phys. Rev. Lett.*, 93:228302-1-228302-4, 2004.

[195] L. Cipelletti, L. Ramos, S. Manley, E. Pitard, D. A. Weitz, E. E. Pashkovski, M. Johansson. *Faraday Discuss.*, 123:237-251, 2003.

[196] E. S. Matsuo, T. Tanaka. *Nature*, 358:482-485, 1992.

[197] G. Gotzamanis, C. Tsitsilianis, K. Papadimitriou. *Polym. Chem*., 2016, DOI: 10.1039/c5py02066b.

[198] M. A. Dyakonova, G. Gotzamanis, B.-J. Niebuur, N. Vishnevetskaya, K. N. Raftopoulos, Z. Di, S. K. Filippov, C. Tsitsilianis, C. M. Papadakis. *in preparation*.

List of publications

Publications related to the subject of the dissertation

1. M. A. Dyakonova, A. V. Berezkin, K. Kyriakos, S. Gkermpoura, M. T. Popescu, S. Filippov, P. Štěpánek, Z. Di, C. Tsitsilianis, C. M. Papadakis. “Salt-induced changes in triblock polyampholyte hydrogels – computer simulations, rheological, structural and dynamic characterization”, *Macromolecules* 48, 8177-8189, 2015.
2. M. A. Dyakonova, N. Stavrouli, M. T. Popescu, K. Kyriakos, I. Grillo, M. Philipp, S. Jaksch, C. Tsitsilianis, C. M. Papadakis. “Physical hydrogels via charge driven self-organization of a triblock polyampholyte - rheological and structural investigations”, *Macromolecules* 47, 7561-7572, 2014.

Further publications

1. K. Kyriakos, M. Philipp, C.-H. Lin, M. Dyakonova, N. Vishnevetskaya, I. Grillo, A. Zaccone, A. Miasnikova, A. Laschewsky, P. Müller-Buschbaum, C. M. Papadakis. “Quantifying the interactions in the aggregation of thermoresponsive polymers – the effect of cononsolvency”, *Macromol. Rapid Commun.* 37, 420-425, 2016.

Conference talks

1. M. A. Dyakonova, K. Kyriakos, S. Gkermpoura, M. T. Popescu, S. Filippov, P. Štěpánek, Z. Di, C. Tsitsilianis, C. M. Papadakis. “Stimuli-responsive polyampholyte hydrogels - influence of charge asymmetry and ionic strength”, *workshop „Crosslinking Science: Hydrogel Microsystems*”, Meissen, Germany, 14 - 15 October, 2015.
2. M. A. Dyakonova, K. Kyriakos, A. V. Berezkin, M.-T. Popescu, N. Stavrouli, S. Jaksch, Z. Di, C. Tsitsilianis, C. M. Papadakis. “Stimuli-responsive reversible hydrogels from triblock polyampholytes and terpolymers”, *2nd internal biennial science meeting of TUM* (*MLZ, E13, E21*), *HZG and JCNS*, Grainau, Germany, 15 - 18 June, 2015.

3. M. A. Dyakonova, M.-T. Popescu, K. Kyriakos, S. Jaksch, C. Tsitsilianis, C. M. Papadakis. “Stimuli-responsive polyampholyte hydrogels - influence of charge asymmetry and ionic strength”, *DPG Frühjahrstagung*, Berlin, Germany, 15 - 20 May, 2015.
4. M. A. Dyakonova, N. Stavrouli, M.-T. Popescu, K. Kyriakos, I. Grillo, M. Philipp, S. Jaksch, C. Tsitsilianis, C. M. Papadakis. “Stimuli-responsive reversible hydrogels from triblock polyelectrolytes and polyampholytes”, *DPG Frühjahrstagung*, Dresden, Germany, 30 March - 4 April, 2014.

Conference poster presentations

1. M. A. Dyakonova, N. Stavrouli, M.-T. Popescu, K. Kyriakos, I. Grillo, M. Philipp, S. Jaksch, C. Tsitsilianis, C. M. Papadakis. “Stimuli-responsive reversible hydrogels from triblock polyelectrolytes and polyampholytes”, *8th International Symposium* “*Molecular Order and Mobility in Polymer Systems”*, St. Petersburg, Russia, 2 - 6 Jun, 2014.
2. M. A. Dyakonova, N. Stavrouli, M.-T. Popescu, K. Kyriakos, I. Grillo, M. Philipp, S. Jaksch, C. Tsitsilianis, C. M. Papadakis. “Stimuli-responsive reversible hydrogels from triblock polyelectrolytes and polyampholytes”, *German-Greek workshop 2014, “Structural Methods for the Investigation of Soft Responsive Matter”*, Garching, Germany, 12 - 16 May, 2014.

Acknowledgment

I would like to express my gratitude towards many people for their kind help, cooperation and support which helped me in completion of this project.

I am heartily thankful to my supervisor, Prof. Dr. Christine M. Papadakis, for her professional guidance, continuous support and patience from the initial to the final stage of the project. Her tremendous academic support and stimulating discussions helped me to develop an understanding of the subject and were essential to the completion of this dissertation.

I wish to express my gratitude to Prof. Dr. Constantinos Tsitsilianis (Laboratory of Macromolecular Engineering, Department of Chemical Engineering, University of Patras, Patras, Greece), who has offered invaluable assistance and support throughout the entire project. Without his broad knowledge and fruitful discussions this study would not have been successful.

Very special thanks to Prof. Dr. Petr Štěpánek and Dr. Sergey Filippov (Department of Supramolecular Polymer Systems, Institute of Macromolecular Chemistry, Prague, Czech Republic), for the opportunity to carry out rotational dynamic light scattering (DLS) measurements. I thank them for the help during measurements and following discussions.

Special gratitude is extended to Dr. Konstantinos Kyriakos for his invaluable help and continuous assistance in technical aspects during the project.

Also I would like to take this opportunity to thank Dr. Teodora Popescu for numerous and helpful discussions, as well as for the generous help during measurements.

I am grateful to Dr. Nikoletta Stavrouli and Dr. George Gotzamanis (Department of Chemical Engineering, University of Patras, Patras, Greece), who synthesized all polymers for present research.

Profound gratitude goes to all beamline scientists: Dr. Sebastian Jaksch and Dr. Zhenyu Di (KWS-1/KWS-2 instruments at the Heinz Maier-Leibnitz Zentrum (MLZ), Garching, Germany) and Dr. Isabelle Grillo (D22 instrument at Institut Laue–Langevin (ILL), Grenoble,

France). Without their support and guidance during the measurements, the present work would not have been complete.

I am also grateful to my colleagues from the Soft Matter Physics Group, who supported me in any respect during the completion of the project: Dr. Anatoly Berezkin, Dr. Konstantinos Raftopoulos, M. Sc. Bart-Jan Niebuur, Chia-Hsin Ko, M. Sc. Xiaohan Zhang, M. Sc. Natalya Vishnevetskaya.

I would also like to take this opportunity to thank the Chair of Functional Materials (Physics Department, TU München) for creating the positive atmosphere and great time during all these years.

Profound gratitude goes to Susanna Fink and Marion Waletzki, who were always there and ready to help with all possible bureaucratic and administrative aspects.

I wish to express my gratitude to my family for their support and belief in me. You have been a constant source of strength and inspiration for me.

In conclusion, I thank TUM Graduate School for financial support, which enabled me to begin my doctoral studies. I thank DAAD and IKY for financial support of mutual visits in the framework of the program for the promotion of the exchange and scientific cooperation between Germany and Greece, IKYDA 2013, and the DAAD program PPP Tschechien, financed by the Bundesministerium für Bildung und Forschung (BMBF), and the Czech Academy of Sciences.